Caractérisation de pathologies cérébrales par l'analyse de modèles multi-compartiment en IRM de diffusion

Renaud Hedouin

ANNÉE 2017

UNIVERSITÉ DE RENNES 1

UNIVERSITE BRETAGNE LOIRE

THÈSE / UNIVERSITÉ DE RENNES 1
sous le sceau de l'Université Bretagne Loire

pour le grade de

DOCTEUR DE L'UNIVERSITÉ DE RENNES 1

Mention : Traitement du signal

Ecole doctorale MATISSE

présentée par

Renaud HÉDOUIN

préparée à l'unité de recherche IRISA UMR CNRS 6074 / Inria Rennes
(Nom développé de l'unité : VisAGeS - INSERM U1228)
UFR Informatique et Electronique (ISTIC)

Diffusion MRI processing for multi-compartment characterization of brain pathology

Thèse soutenue à Rennes le 12/06/2017

devant le jury composé de :

Rachid DERICHE Rapporteur
Directeur de recherche, Inria Sophia Antipolis

Jean-Philippe THIRAN Rapporteur
Associate professor, EPFL

Isabelle BERRY Examinateur
PU-PH, CHU Toulouse

Patrick PEREZ Examinateur
Directeur de recherche, Technicolor Rennes

Simon WARFIELD Examinateur
Director of research, Boston Children's Hospital

Christian BARILLOT Directeur de thèse, Directeur de recherche, CNRS

Olivier COMMOWICK Co-directeur de thèse, Chargé de recherche, Inria Rennes

Diffusion MRI processing for multi-compartment characterization of brain pathology

Abstract: Diffusion weighted imaging (DWI) is a specific type of MRI acquisition based on the direction of diffusion of the brain water molecules. It allows, through several acquisitions, to model the brain microstructure, as white matter, which is significantly smaller than the voxel-resolution.

To acquire a large number of images in a clinical setting, very-fast acquisition techniques are required as single-shot imaging. However these acquisitions suffer locally large distortions. We propose a block-matching registration method based on the acquisition of images with opposite phase-encoding directions (PED). This technique specially designed for Echo-Planar Images (EPI) robustly correct images and provides a deformation field. This field is applicable to an entire DWI series from only one reversed EPI allowing distortion correction with a minimal acquisition time cost. This registration algorithm has been validated both on phantom and on *in vivo* data and is available in our source medical image processing toolbox Anima.

From these diffusion images, we are able to construct multi-compartments models (MCM) which can represent complex brain microstructure. Doing registration, averaging and atlas creation on these MCM images is required to perform studies and statistic analyses. We propose a general method to interpolate MCM as a simplification problem based on spectral clustering. This technique, which is adaptable for any MCM, has been validated on both synthetic and real data. Then, from a registered dataset, we performed a patient to population analysis at a voxel-level computing statistics on MCM parameters. Specifically designed tractography can also be used to make analysis, following tracks, based on individual anisotropic compartments. All these tools are designed and used on real data and contribute to the search of biomakers for brain diseases such as multiple sclerosis.

Keyworlds: Diffusion MRI, Registration, Block-Matching, Multi Compartment models

Caractérisation de pathologies cérébrales par l'analyse de modèles multi-compartiment en IRM de diffusion

Abstract: L'imagerie pondérée en diffusion est un type d'acquisition IRM spécifique basé sur la direction de diffusion des molécules d'eau dans le cerveau. Cela permet, au moyen de plusieurs acquisitions, de modéliser la microstructure du cerveau, comme la substance blanche qui a une taille très inférieure à la résolution du voxel.

L'obtention d'un grand nombre d'images nécessite, pour un usage clinique, des techniques d'acquisition ultra rapides tel que l'imagerie parallèle. Malheureusement, ces images sont entachées de larges distortions. Nous proposons une méthode de recalage par blocs basée sur l'acquisition d'images avec des directions de phase d'encodage opposées. Cette technique spécialement conçue pour des images écho planaires, mais qui peut être générique, corrige les images de façon robuste tout en fournissant un champ de déformation. Cette transformation est applicable à une série entière d'images de diffusion à partir d'une seule image b_0 renversée, ce qui permet de faire de la correction de distortion avec un temps d'acquisition supplémentaire minimal. Cet algorithme de recalage, qui a été validé à la fois sur des données synthétiques et cliniques, est disponible avec notre logiciel de traitement d'images Anima.

A partir de ces images de diffusion, nous sommes capables de construire des modèles de diffusion multi-compartiment qui représentent la microstructure complexe du cerveau. Pour pouvoir produire des analyses statistiques sur ces modèles, nous devons être capables de faire du recalage, du moyennage, ou encore de créer un atlas d'images. Nous proposons une méthode générale pour interpoler des modèles multi-compartiment comme un problème de simplification basé sur le partitionnement spectral. Cette technique qui est adaptable pour n'importe quel modèle, a été validée à la fois sur des données synthétiques et réelles. Ensuite à partir d'une base de données recalée, nous faisons des analyses statistiques en extrayant des paramètres au niveau du voxel. Une tractographie, spécifiquement conçue pour les modèles multi-compartiment, est aussi utilisée pour faire des analyses en suivant les fibres de substance blanche. Ces outils sont conçus et appliqués à des données réelles pour contribuer à la recherche de biomarqueurs pour les pathologies cérébrales.

Mot clés: IRM de diffusion, Recalage, Block-Matching, Modèles multi-compartiment

Contents

Chapter 1

Résumé en français

1.1 Contexte général

L'imagerie par résonance magnétique (IRM) est un examen médical qui produit des images *in-vivo* des organes internes et des structures du corps. Pendant cet examen, le sujet est installé dans un champ magnétique puissant et homogène qui est généralement généré à l'intérieur d'un long tube (voir Fig 1.1). L'IRM est basée sur la résonnance magnétique nucléaire et utilise les propriétés magnétiques des noyaux des atomes. L'eau est le composant principal du corps humain, la proportion qui dépend de nombreux facteurs dont l'âge est comprise entre 55% et 80% [Brozek 1961, Siri 1961, Ellis 2000]. Par conséquent, même si tous les atomes peuvent théoriquement être étudiés, pour l'IRM clinique, les atomes d'hydrogènes qui composent l'eau sont préférés. Un des avantages de l'IRM est que contrairement à d'autres modalités (comme les rayons X ou la tomodensitométrie), c'est une technique d'imagerie non-invasive.

Figure 1.1: Illustration d'un appareil IRM. *Common license,* https://commons.wikimedia.org/wiki/File:MRI-Philips.JPG

Une grande variété de séquences IRM existent avec des temps d'acquisitions différents. Générallement, différentes séquences peuvent être acquises durant un même examen pour obtenir des informations complémentaires sur le patient. Le temps d'acquisition total d'un examen IRM est important pour plusieurs raisons. Tout d'abord, le confort du patient est crucial, non seulement pour son bien-être, mais aussi parce que si des mouvements surviennent pendant une longue sequence, les images résultantes seront dégradées. En outre, la complexité d'une machine IRM fait que les examens sont couteux. Selon le type de séquence et le choix des paramètres, une IRM produit un type d'imagerie varié ce qui inclut des images anatomiques, de l'imagerie fonctionnelle ou de l'imagerie quantitative.

En raison de sa faible dangerosité et de sa haute résolution spatiale, l'IRM est devenu un examen incontournable avec la tomodensitométrie pour l'étude des organes internes. Son usage clinque s'est répandu dans un grand nombre de domaine incluant: les pathologies thoraciques, les pathologies artérielles, les pathologies digestives, les maladies du système nerveux central [Calvo 2001, Gebker 2007, Sandrasegaran 2005, Polman 2005]...

L'examen IRM est tout d'abord utilisé pour établir un diagnostique: localiser des tumeurs, étudier les problèmes d'articulations, préparer une intervention chirurgicale. Il permet également de surveiller l'évolution d'une maladie au cour d'une étude longitudinale et de pouvoir adapter un meilleur traitement. Il est aussi essentiel pour la recherche médicale, en particulier en neuroscience. En effet, les connaissances scientifiques sur le cerveau, à la fois anatomiques et fonctionnelles, ont largement progréssées grace aux études IRM. Désormais, les IRM sont des examens médicaux classiques et essentiels pour un usage clinique ainsi que pour la recherche scientifique. L'IRM de diffusion est un type particulier d'acquisition IRM, c'est le sujet principal de cette thèse. Cette technique vise à étudier la direction et la quantité de diffusion des molécules d'eau dans le cerveau. Cela permet, moyennant plusieurs acquisitions, de modéliser indirectement la microstructure du cerveau. La substance blanche en particulier a une taille nettement inférieur (le diamètre d'un axone est de l'ordre du micromètre) à l'unité de résolution spatiale, le voxel (qui est de l'ordre du millimètre cube). L'étude de la microstructure du cerveau par l'IRM de diffusion est un grand défi qui nécessite des méthodes précises et des modèles adaptés à la fois pour la qualité de l'acquisition et pour la reconstruction de la microstructure au niveau du voxel. Dans ce manuscript, nous nous focaliserons sur cette modalité IRM particulière.

L'IRM de diffusion peut apporter un excellent aperçu dans la qualification d'une maladie et l'adaptation du traitement. Le premier défi de l'IRM de diffusion est la conception et l'estimation des modèles de diffusion. Cet aspect a été largement étudié et une revue de la littérature sur le sujet est présentée en Section 1.2. Les acquisitions utilisées pour l'IRM de diffusion ont des artefacts, la correction de distortion de ces artefacts est introduite Section 1.3. Enfin, nous présentons des méthodes de traitements et des outils statistiques pour une classe de modèle de diffusion complexe appelé modèle multi-compartiment en Section 2.4 et Section 1.5.

1.2 Etat de l'art

Le manuscrit commence par un état de l'art (Chapitre 3) en proposant une présentation rapide du cerveau humain ainsi qu'une description des principales catégories de pathologies cérébrales et de l'impact potentiel des techniques d'imagerie médicale sur ces pathologies.

Des spins des atomes d'hydrogènes à la récupération du signal dans l'espace de Fourier, l'IRM est une modalité complexe d'imagerie médicale. En outre, les acquisitions d'IRM de diffusion (DWI) que nous étudions sont basées sur la diffusion naturelle des molécules d'eau selon différent tissues. Les principes généraux de l'IRM et la spécificité des acquistions DWI sont introduits dans ce chapitre.

Dans le reste de l'état de l'art, différent modèles de diffusion estimés à partir d'acquisition DWI sont présentés. Nous soulignons les forces et faiblesses de ces modèles classés en trois catégories:

- L'imagerie du tenseur de diffusion (DTI) représente la diffusion d'eau au sein de chaque voxel au moyen d'un tenseur.
- Les modèles basés sur la décomposition du signal dans une base de fonctions orthogonales.
- Les modèles multi-compartiment (MCM) représentant la diffusion avec plusieurs compartiments isotropiques et anisotropiques.

1.3 Correction de distortion des images écho planaires

En diminuant la durée d'acquisition des IRM, les techniques d'imagerie parallèle permettent l'acquisition d'un grand nombre d'images (EPI) dans un court laps de temps, compatible avec des contraintes cliniques requises pour l'imagerie de diffusion ou l'imagerie fonctionnelle. Cependant, ces images sont soumises à de larges distortions perturbant leurs correspondance avec l'anatomie sous jacente. La correction de ces distortions reste un problème ouvert, spécialement dans les zones sévèrement impactées par de grandes déformations.

Nous proposons au Chapitre 4 une nouvelle technique de block-matching basée sur l'acquisition de deux EPI avec des directions de phases d'encodages opposées. Cela s'appuie sur de nouvelles transformations entre les blocs adaptées au modèle de distortion et sur un schéma d'optimisation qui assure une transformation symétrique. Nous présentons des résultats qualitatifs et quantitatifs de correction par block-matching en utilisant différentes métriques à la fois sur des données synthétiques et sur des données réelles. Nous montrons la qualité de la correction block-matching et sa robustesse, y comprit dans des zones fortement affectées par les déformations. Pour finir nous présentons dans les perspectives un algorithme block-matching totalement symétrique qui utilise une image structurelle supplémentaire non distordue comme une image centrale.

1.4 Interpolation des modèles multi-compartiment

Les modèles multi-compartiment (MCMs) sont de plus en plus utilisés pour charactériser la substance blanche du cerveau à partir d'images pondérées en diffusion. Dans le Chapitre 5, nous posons le problème d'interpolation et de moyennage des MCMs comme un problème de simplification basé sur le partitionnement spectral.

Ces méthodes génériques sont testées pour les modèles multi-tenseurs et évaluées pour un MCM spécifique: le diffusion direction imaging (DDI). Les résultats calculés à partir d'une large base de données, montrent la supériorité de la méthode analytique, calculé à partir de la partie tenseur interne du DDI, par rapport à d'autres méthodes plus simples. Nous présentons également un atlas MCM de sujets sains construit en utilisant les méthodes d'interpolations proposées.

1.5 Statistiques sur les modèles multi-compartiment

Pour finir, nous proposons dans le Chapitre 6 de calculer des statistiques en utilisant les méthodes d'interpolations proposées précédemment. Nous présentons une comparaison d'un patient à une population de sujets sains recalée sur un atlas, à la fois au niveau du voxel et au niveau des fibres. La tractographie est spécialement conçue pour être bien adapté aux MCM par rapport aux tractographies ordinaire réalisées sur DTI.

La construction de l'atlas, illustrée dans le Chapitre 5, et les méthodes de recalage sont détaillées. Un grand nombre de figures illustrent les deux approches basées sur les voxels ou sur les fibres. Cela souligne les forces et faiblesses des deux techniques. La comparaison avec le DTI montre une meilleure interprétabilité des résultats.

Chapter 2

Introduction

Contents

2.1 General context

Magnetic resonance imaging (MRI) is a medical exam that produces *in vivo* images of internal organs and structure of the body. During the exam, the subject is installed inside a strong, homogeneous, magnetic field that is commonly generated within an horizontal tube (see Fig 2.1). MRI is based on nuclear magnetic resonance (NMR) using the magnetic properties of atoms nuclei. Water is the main component of the human body, proportion is of around 55% to 80% depending on various factors including age [Brozek 1961, Siri 1961, Ellis 2000]. Hence, even if all atoms can theoretically be studied, the hydrogen atom that composes water molecules is preferred in clinical MRI. A benefit of MRI is that contrary to other imaging modalities (as X-ray or computed tomography (CT)), it does not use ionizing radiation. While the precautionary principle is still required, the food and drug administration (FDA) declared in 2003, a nonsignificant risk status for MRI clinical systems generating static fields up to 8 Tesla [Hartwig 2009].

A wide range of MRI sequences exist with different acquisition times. Usually different sequences can be acquired in the same exam to get complementary information on the subject or patient. The total acquisition time of an MRI exam is important mainly for two reasons. First, the patient comfort is crucial, not even for his own well-being, but also since motion is more likely to occur during a long scan and the resulting images may thus be corrupted. Secondly, the complexity of an MRI scanner makes it an expensive exam. Depending on the sequence type and the parameters choice, MRI scan produces various types of images including anatomical images, functional images or quantitative imaging.

Due to its weak dangerosity and its high spatial resolution, MRI takes a growing place for internal body exams next to CT. It has been increasingly adopted for clinic

Figure 2.1: Illustration of a MRI scan. *Common license, courtesy of Jan Ainali , https://commons.wikimedia.org/wiki/File:MRI-Philips.JPG*

in all kind of domain such as: thoracic pathology, osteoarthritis pathology, digestive pathology, central nervous system (CNS) disorders [Calvo 2001, Gebker 2007, Sandrasegaran 2005, Polman 2005]...

MRI exams are primarily used to perform diagnostic: find unhealthy tissue, locate tumors, bone damage, surgery planning. Moreover, it allows to monitor the evolution of a disease within a longitudinal study and better adapt a treatment. It is also essential for research advancement, in particular in neuroscience. Indeed, the scientific knowledge about the brain, both anatomic and functional, has largely progressed thanks to MRI studies. Henceforth, MRI scans are classic and essential medical exams in clinic and to improve the brain comprehension in research.

Diffusion-weighted magnetic resonance imaging (DWI) also named diffusion MRI (dMRI) is a specific type of magnetic resonance imaging (MRI) acquisition, the main topic of this thesis, aimed at studying the direction and amount of diffusion of brain water molecules. It allows, through several acquisitions, to model indirectly the brain microstructure, especially the brain white matter (WM), which are significantly smaller than the voxel-resolution. The study of the brain microstructure through dMRI is a great challenge which needs accurate methods and well adapted models, both to the quality of the acquisition and to the expected voxel microstructure. We will focus on this specific MRI modality in this manuscript.

The dMRI may bring a great insight in disease quantification and treatment adaptation. The design and estimation of the diffusion model is the first challenge with dMRI. This aspect, well studied by a large literature, is introduced Section

2.2. The acquisitions used to model diffusion suffer from artifacts, the correction of distortion artifacts is presented Section 2.3. Finally, we present processing tools and statistical methods for a class of complex diffusion models named MCM in Section 2.4 and Section 2.5.

2.2 State of the art

We start this manuscript by a state-of-the-art (Chapter 3), first proposing a quick overview of the human brain, followed by a description of the main categories of brain diseases and the potential impact of medical imaging for those diseases.

From the spin of hydrogen nuclei to the signal recovery in the Fourier space, the MRI scanner is a complex medical imaging modality. Moreover, the DWI acquisitions are based on the natural diffusion of water molecules within different tissues. The MRI general principles and the specificity of the DWI acquisition are thus also introduced in this chapter.

In the rest of the state of the art, different models of water diffusion estimated from DWI acquisitions are presented. We highlight the strength and weakness of all these models divided in three categories:

- Diffusion tensor imaging (DTI) representing the water diffusion within each voxel with a tensor
- Based functions in q-space derived from the decomposition of the signal through an orthogonal basis of functions.
- Multi-compartment models (MCMs) representing the diffusion with several isotropic compartments and anisotropic compartments.

2.3 Distortion correction of echo-planar images

By shortening the acquisition time of MRI, echo planar imaging (EPI) enables the acquisition of a large number of images in a short time, compatible with clinical constraints as required for dMRI or functional MRI (fMRI). However such images are subject to large, local distortions disrupting their correspondence with the underlying anatomy. The correction of those distortions is an open problem, especially in regions where large deformations occur.

We propose in Chapter 4 a new block-matching registration method to perform EPI distortion correction based on the acquisition of two EPI with opposite phase encoding direction (PED). It relies on new transformations between blocks adapted to the EPI distortion model, and on an adapted optimization scheme to ensure an opposite symmetric transformation. We present qualitative and quantitative results of the block-matching correction using different metrics on a phantom dataset and on *in vivo* data. We show the ability of the block-matching approach to robustly correct EPI distortion even in strongly affected areas. Finally, we present in perspectives a

fully symmetric block-matching (BM) algorithm which uses an extra non-distorted structural image as the center image.

2.4 Interpolation of multi-compartment models

MCMs are increasingly used to characterize the brain white matter microstructure from dMRI. In chapter 5, we address the problem of interpolation and averaging of MCM images as a simplification problem based on spectral clustering. As a core part of the framework, we propose novel solutions for the averaging of MCM compartments.

This generic framework is tested for multi-tensor model (MTM) and evaluated for a specific MCM: the diffusion direction imaging (DDI). Results, computed on a large database, show the ability of the analytic method accounting for the internal tensor part of the DDI to perform better than simpler ones. We then present an MCM template of normal controls constructed using the proposed interpolation framework.

2.5 From multi-compartment model to statistics

We finally present in Chapter 6 to perform statistics using the interpolation framework proposed in Chapter 5. We propose an atlas-based patient to population comparison based on MCM data, both voxel-based and tract-based. The tract-based part relies on the construction of an atlas, MCM tractography and compartment selection along the tracts to take full advantage of the multiple compartments of the models.

The construction of the atlas, illustrated in Chapter 5, and the registration method are detailed. A deterministic tractography algorithm specifically adapted for MCM is also presented. A large number of figure illustrate the two approaches, voxel-based and tract-based. They highlight different strengths and weaknesses of both techniques and compare then to DTI based results, showing better interpretability of the obtained results.

Chapter 3

State of the art

Contents

3.1 General context

3.1.1 General presentation of the human brain

The central nervous system (CNS) is composed by the brain which centralizes the control of the body, conscious and unconscious thoughts, and the spinal cord. The peripheric nervous system (PNS) is the rest of the nervous system which connects the CNS to the rest of the body. According to the Society of Neuroscience, the human brain is the most complex living structure in the known universe. The human brain consists of the cerebrum, the cerebellum and the brainstem.

The cerebrum, the largest part, is divided by several sulci and gyri in 4 lobes: occipital, parietal, frontal and temporal (see Fig 3.1). Each lobe is related to a different function and is connected to the other by the white matter:

- **The frontal lobe** in the front of the cranial cavity is associated to the voluntary motor function. It is also involved in judgment, decision-making, language through the Broca's area and more.
- **The parietal lobe** is behind the frontal lobe separated by the central sulcus. It plays a role in space perception, reading through the oculomotor system and receives the major part of sensitive information.
- **The temporal lobe** is under the frontal and parietal lobe separated by the lateral sulcus. It is involved in auditory processing and visual processing, language recognition (through the Wernicke's area in tandem with the Broca's area). The temporal lobe contains the limbic system which handles the treatment of emotion. The hippocampus belongs to the lymbic system and plays a crucial role in memory and spatial navigation.
- **The occipital lobe**, located behind the temporal lobe, is the smallest of the 4 lobes. It is mainly the visual processing center of the brain.

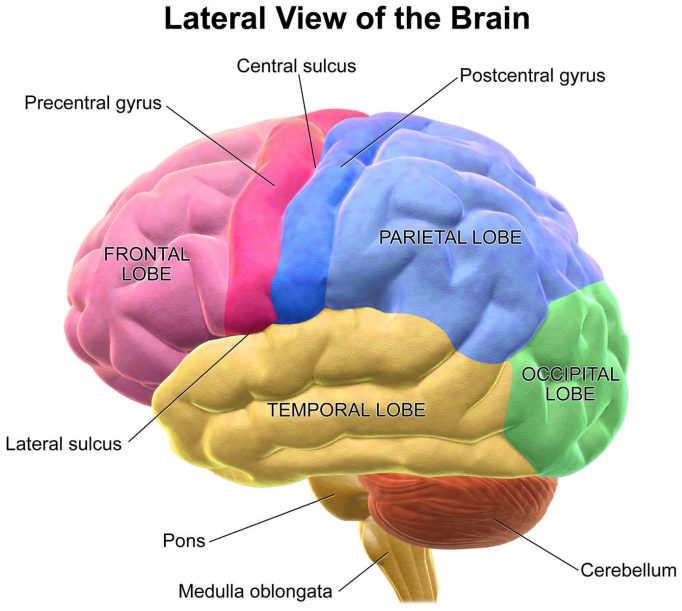

Figure 3.1: Schematic representation of the brain with the 4 lobes, the main sulcus and the cerebellum. *Courtesy of Blausen,* https://en.wikipedia.org/wiki/Lobes_of_the_brain

Under the occipital and the temporal lobe is the cerebellum. Its major function is to coordinate motor control. It also plays a role in cognitive functions such as

attention and language. The brainstem connects the cerebrum and the cerebellum to the rest of the body and regulates the cardiac and respiratory functions. This description composes a schematic review of the brain at a macroscopic level.

At a microscopic scale, the human brain contains neurons and glial cells which include all the non-neuronal cells. There are around 100 billion neurons in a human adult brain and recent studies advance the same quantity of glial cells [Hilgetag 2009, Pakkenberg 1988]. The cell body of the neuron and some glial cells compose the grey matter (GM) named in opposition to the WM which designate the axonal fibers of the neurons. The GM is mainly located at the periphery of the brain around the cranial cavity and is basically the seat of the consciousness. There is also a deeper gray matter made of brainstem and nuclei. The WM, which is bright in dissection because of the myelin, is responsible of the transmission of the information through the axons between different areas of the brain or between the brain and body.

A typical neuron comports mainly a cell body, an axon and dendrites (see a complete illustration of a neuron on Fig 3.2). The axon transfers the electric signal from one neuron to another cell via its terminations called synapses. Each axon includes thousand of synapses that transmit the signal via a chemical process to the dendrites of other neurons. The axon has a diameter of around $1\mu m$ (from $0.5\mu m$ up to $8\mu m$) and can reach up to 1 meter in length (therefore the total length of axons is evaluated to be longer than 100.000 km [Schröder 1978, Marner 2003]). Glial cells comprise the following cells, all helping brain function:

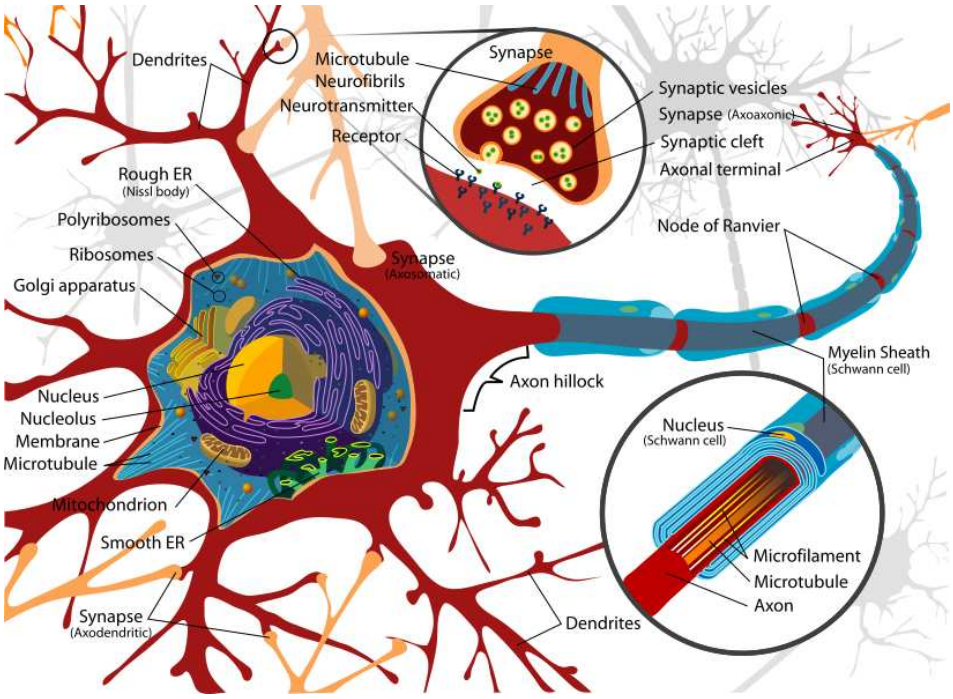

Figure 3.2: Illustration of a neuron. *Common license,* https://en.wikipedia.org/wiki/Neuron

- **Astrocytes** cover a large subclass of glial cells with all kind of supporting tasks in the CNS and PNS. The word astrocyte derived from their star shape, however their morphologies are extremely diverse [Zhang 2012a]. They compose between 20 and 40 % of all the glial cells and execute their supportive tasks while maintaining neuronal health. Several forms of astrocytes exist including protoplasmic, which mainly support the GM, and fibrous for the WM [Sofroniew 2010]. During decades, astrocytes were considered as passive in the brain. Contrariwise, many studies revealed their active role in metabolic support of neurons, synaptic generation, detoxification, guidance of neuronal migration, immune function and more [Markiewicz 2006]. Moreover astrocytes stimulate the neuron-generating process [Svendsen 2002].

- **Oligodendrocytes** is an other specific type of glial cells which create membranes around one or several axons of the CNS (the Schwann cells play a similar role in the PNS). These membranes compose the myelin sheath which form an electrically insulating layer around axons. The myelin is a fat substance composed by 80% of lipids and 20% of proteins [Laatsch 1962, Gerstl 1967]. Overall the length of the axon myelin sheaths are interrupted by nodes of Ranvier (see Fig 3.2). Information is transmitted along the axon through saltatory conduction, thanks to the myelin, making the signal transmission between neurons much faster. Schematically the action potentials jump from one node to the following. The myelin sheath is thus essential to protect axons and provide velocity to the electric signal up to 50 times compared to an unmyelinated fiber [Koch 2004]. The acquisition of myelin in the vertebrate lineage is important in the evolution since the velocity of the information propagation is crucial to survive [Zalc 2006]. The axon and myelin sheath also modify the diffusion of water molecules within the brain and therefore is an object of study for dMRI (see Section 3.5.3).

3.1.2 Brain diseases

The proper functioning of the brain through neurons and glial cells can be disturbed by all kinds of diseases. The brain disorders can be classified into four main categories:

- **Traumatic brain injury (TBI)** is caused by external action impacting the brain as impact, object penetration, deceleration, chemicals damage. They can cause injuries with different degrees of severity: hematomas, contusion, strokes, ischemia... After an accident, cerebral imaging exams can be performed to detect such TBI.

- **Brain cancer** is the anarchical propagation of abnormal cells within the brain. Such diseases still have a high mortality ratio of around 40 % for children to 95 % for elderly people [Legler 1999]. Such tumors are often detected through unusual symptoms due to the expansion of the tumor perturbing brain function: nausea, speech difficulties, behavior change, vision problems, hearing

problems. MRI scanner allows to detect the tumor, analyze its evolution, and to prepare and follow its treatment (chemotherapy, radiotherapy, surgery).

- **Psychiatric disorders** are a brain diseases which disorganize personality, mind or emotion. They include depression, bipolar disorder, anxiety, post-traumatic stress disorder (PTSD). The cause of such disorders is often unclear. However diseases such as depression are frequently related to anatomical brain anomalies and thus can be studied with cerebral imaging modalities [Mervaala 2000, Treadway 2011].

- **Neurodegenerative diseases** cause a progressive deterioration of neurons. Such disorders include Parkinson's disease, Alzheimer's disease, Huntington's disease or amyotrophic lateral sclerosis (ALS) and are often incurable [Gandhi 2005, Pluchino 2003, Lambrechts 2003]. Symptoms can induce memory loss, apathy, anxiety, motor issues [Paulsen 2001, Jack 2010, Chaudhuri 2006]. The evolution of such diseases are well-studied with classic MRI modality but also fMRI or positron emission tomography (PET) scan [Nordberg 2010].

To conclude this quick review of brain diseases, we detail one particular disorder: multiple sclerosis (MS). The deficit of myelin in the CNS can cause massive injury for vision, memory, motricity and more. MS is a serious and common autoimmune disease which induces chronic demyelination of the CNS. There are around 100.000 individuals suffering from MS in France. Affected persons, mostly located in the northern hemisphere, are young adults and the female to male ratio is about 3:1 [Ascherio 2007, Orton 2006]. There exist genetic risk factors and not-well defined environmental factors (as sunshine, tobacco or obesity) [Hedström 2012, Consortium 2011]. MS is rarely directly mortal but induces severe synptoms including motor, mental and sometimes psychatric issues [Compston 1998]. MS has a high variability between individuals and its evolution is hard to predict. Intensive research has been carried out on this disease, especially using MRI [Barkhof 1997, Brex 2002, Lublin 1996, Polman 2005].

Leukodystrophies, a class of rare diseases, also cause demyelination of the CNS. These diseases affect children and their mortality rate is 1/3 [Bonkowsky 2010]. Demyelination can also occur in the PNS due to several diseases [Sumner 1991, Hartung 2000]. The common point of all these diseases is the possible utilization of MRI to make an accurate diagnostic and study the evolution of the disorder. This can lead to the improved understanding of a disease, for a particular patient as well as in general. It will thus allows, among other, to offer better treatments, to predict the evolution of the disease or to perform surgery.

3.1.3 Brain imaging

Knowledge about the brain follows a fast and expanding progression while its organization(functional and structural) is still largely unknown [Kötter 2001, Sporns 2005]. In history, the first anatomical descriptions of the brain where made from dissections.

Vesalius produced one of the first works about human anatomy during the sixteenth century in his book *De humani corporis fabrica* [Vesalius 1543]. Among these descriptions were included some of the first illustrations of the CNS [Van Laere 1992]. At this time, dissections were prohibited by the Christian church and some medical students stole bodies to increase their brain anatomy performing illegal dissections [Boorstin 1985].

From an anatomical point of view, knowledge about the brain microstructure evolved first with the development of light microscope [Wilt 2009]. In the early twentieth century, electroencephalography (EEG) was developed and provided a first approach to probe *in vivo* the brain activity. It was followed from 1950 by a large number of different *in vivo* imaging methods including MRI. The history of MRI starts around 1946 with the discovery of the magnetic resonance effect by Felix Bloch and Edward Purcell [Bloch 1946, Purcell 1946]. Thirty years later, the first image of a tumor in a mouse was obtained, highlighting the interest of such a technic for a medical use [Damadian 1976].

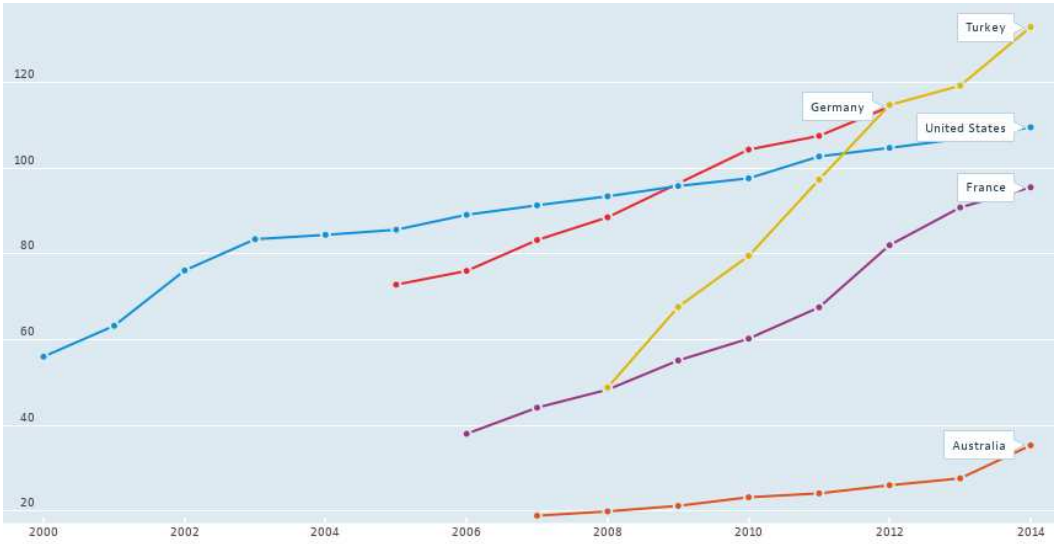

Figure 3.3: Evolution of the number of MRI exams per 1000 habitants along France, Australia, Germany, Turkey and United States. *OECD database,* `https://data.oecd.org/healthcare/magnetic-resonance-imaging-mri-exams.htm`

Today the use of MRI for clinical exams is constantly growing in the OECD countries (see Fig 3.3). Although expensive, recent MRI techniques offer a high image resolution to study the brain anatomy. There are 3 main types of MRI modalities:

- **Conventional MRI** techniques provide an anatomical image through one measure during the spin relaxation. The obtained image, such as T1-weighted or T2-weighted, depends of the scanner parameters (mainly echo time (TE), repetition time (TR)).

- **functional MRI (fMRI)** measures the brain activity through the cerebral blood oxygenation. It is able to produce a high spatial resolution map with a reasonable time resolution of the cerebral activity.

- **Quantitative MRI** directly relates the MRI signals to physical tissue properties. For example, relaxometry sequences measure the signal at several times to reconstruct relaxation curves which are specific to each tissue. dMRI measures the diffusion of the water molecules within the brain to infer microstructure properties. The Apparent Diffusion Coefficient (ADC) and the anisotropic structure of the brain provide informations about the brain structure, in particular the WM. In this thesis, we focus on this specific modality.

3.2 Diffusion MRI

Diffusion MRI (dMRI) or diffusion-weighted magnetic resonance imaging (DWI) is a specific type of MRI sequence that studies the constrained random diffusion of water molecules within different tissues. The phenomena of molecular diffusion within a magnetic field has been known and studied for a long time [Hahn 1950, Carr 1954, Stejskal 1965]. The first DWI images of the human brain were obtained more recently in 1985 [Le Bihan 1986]. The interest of the neuroscientific community for this modality has since largely grown since studies have demonstrated the ability of dMRI to detect strokes better than MRI traditional sequences [Moseley 1990]. The major clinical applications of dMRI concern neurological disorders, in particular diseases where the WM is affected. DWI is indeed the unique non-invasive *in vivo* modality allowing to model the microstructure of the brain [Le Bihan 2012]. The general principle of natural water diffusion is presented in Section 3.2.1. The study of this phenomena though dMRI acquisition is described in Section 3.2.2. We finally detail in Section 3.2.3 the acquisitions strategies of dMRI and their artefacts.

3.2.1 Principles of water diffusion

Diffusion characterizes the migration of molecules from the highest to the lowest concentration within a liquid, solid or gas solution. This phenomenon is natural and internal to a solution without any external action. For liquid solutions, at a macroscopic level, the diffusion is well modeled by Fick's law defined as [Fick 1855]:

$$J = -D\nabla n \tag{3.1}$$

where D is the diffusion coefficient, J is the net diffusion flux and ∇n the concentration gradient. D is determined by the medium through the particle size, the temperature and the viscosity of the fluid.

At a microscopic level, the molecules have movements induced by thermal energy. In a medium with uniform concentration, the diffusion flux is null, however the motion of molecules still persists. During the observation of pollen grains in a water solution with a microscope, Robert Brown discovered that large particles

such as pollen are affected by permanent motions [Brown 1828]. The large particle is in fact hit by small particles, molecules, around 10^{21} times per second in a water solution [Chandrasekhar 1943]. This movement is named Brownian motion and is used to describe diffusion but also thermodynamic or financial flux in economy [De Meyer 2003]. An illustration of Brownian motion for several diffusion coefficients is presented Fig 3.4.

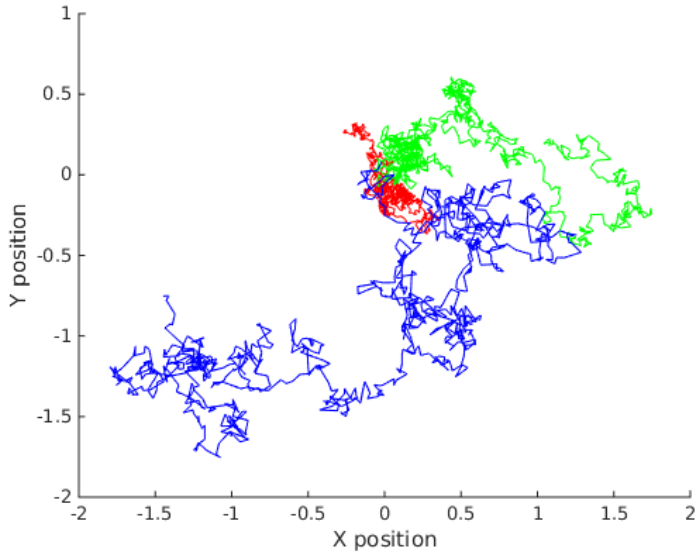

Figure 3.4: Illustration of Brownian motion of three particles with different diffusion coefficients, red: $D = 1.10^{-3}\ mm^2.s^{-1}$, green: $D = 2.10^{-3}\ mm^2.s^{-1}$, blue: $D = 4.10^{-3}\ mm^2.s^{-1}$ for 1000 steps and a time between step $\Delta = 0.1s$

The net flux of the solution, i.e the mean displacement of a particle, is null. Therefore the relation with the diffusion coefficient does not come directly. In 1905, in his famous *annus mirabilis* [Stachel 2005], Albert Einstein found in the Brownian motion the proof of existence of atoms he was seeking. Moreover, he proposed a probabilistic model of the mean-square displacement of a particle as [Einstein 1905]:

$$\langle x^2 \rangle = 2dD\Delta \tag{3.2}$$

where $\langle x^2 \rangle$ is the mean-squared displacement of a particle during a diffusion time Δ, d is the dimensionality of the problem and D is the diffusion coefficient.

Water molecules compose around 75% of the brain depending on the evaluation techniques [Kreis 1993, Lentner 1981]. Hence, knowledge about diffusion of water within the brain provides powerful information about tissues and structures. For example the diffusion coefficient increases within a tumor compared to normal brain tissue [Maier 2010, Padhani 2009]. Moreover, the anisotropy of water diffusion is used as a marker to identify the brain microstructure. Indeed, water diffusion is constrained by the orientation of the axons within the WM. We will see in the

following how the diffusion framework using a magnetic field is used to estimate water diffusion within the brain.

3.2.2 Diffusion within a magnetic field

3.2.2.1 MRI

An MRI scanner generates a strong static magnetic field B_0, typically from 1 to 7 Tesla for human, which is up to 100.000 times more than the earth $60\mu T$ magnetic field [Gómez Paccard 2006]. Hydrogen nuclei have a magnetic dipole named spins. They align themselves with the magnetic field B_0 in a proportion related to the strength field. This is called the longitudinal magnetization. When the spins are aligned, a radiofrequency (RF) pulse is applied to excite the system at a frequency named Larmor frequency:

$$\omega = -\gamma B \tag{3.3}$$

where ω is the Larmor frequency, B the magnetic field strength and γ the gyromagnetic ratio which depends on the mass of the nuclei. The gyromagnetic ratio makes the Larmor frequency unique for each nucleus [Cohen 2010]. Once excited, spins enter a resonance regime, for a sufficient RF pulse, the spins end up oriented in the normal plane to the static magnetic field axis. It creates a transverse magnetization. After this brief RF pulse, spins return to their previous orientations aligned with the B_0 axis. An illustration of the process from the excitation until the end of relaxation is presented Fig 3.5.

During this step named relaxation, in conventional MRI, the signal is recorded by the coils at one particular moment named TE. Then the process is repeated after a TR that allows or not a complete return of the nuclei spins to their state before the RF pulse. On a $3T$ scanner, the order of magnitude of these times is around $50ms$ for the TE and $1s$ for the TR.

Each tissue has its own transversal relaxation time $T2$ and longitudinal relaxation time $T1$. From these intrinsic properties, it is possible to reconstruct an image for the signal highlighting different tissues with different contrasts by choosing appropriately TE and TR. Interestingly, the $T2$ relaxation time is longer for the grey matter than the white matter and it is the opposite for the $T1$ relaxation time [Mlynárik 2001]. T1-weighted images and T2-weighed images are two classical types of conventional sequences for MRI scanner. A short TE and a short TR give a T1-weighted image i.e an image where intensities vary mainly depending on the tissues T1 relaxation time. Contrariwise, a long TE and a long TR give a T2-weighted image. Thereby, these two measures have different properties that confer them different advantages and disadvantages.

As we have seen in Eq 3.3, the Larmor frequency depends on the magnetic field strength. With the constant magnetic field B_0 of the scanner, all hydrogen nuclei are simultaneously excited. It is impossible to reconstruct from the signal received by the coils a map with correct spatial precision of the origin of the signal. Therefore an

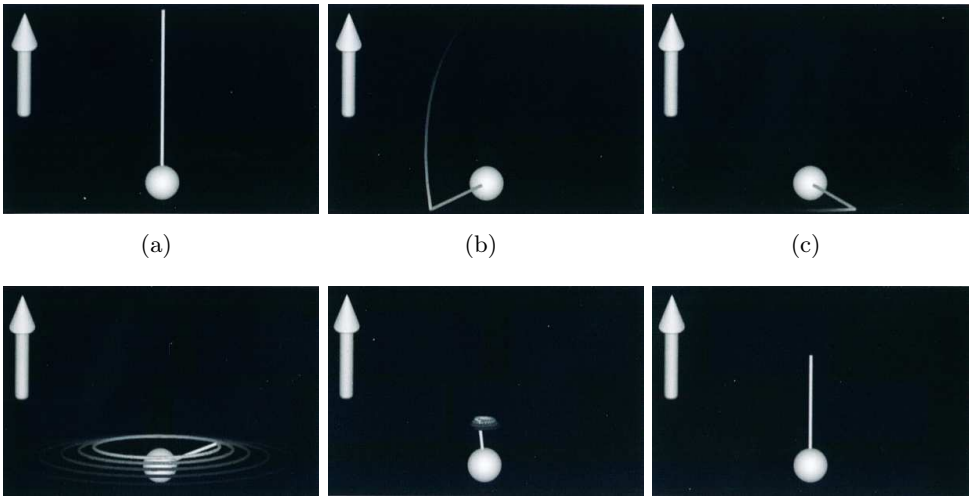

(a) (b) (c)

(d) (e) (f)

Figure 3.5: Illustration of spin behavior. (a) spin in phase with the magnetic field, (b) application of the RF pulse, (c-d) transversal relaxation, (e) longitudinal relaxation, (f) end of relaxation: spins are back aligned with the magnetic field. *Courtesy from pipe [Johansen-Berg 2009]*

other linear magnetic field, called gradient, is applied to select a specific area which is the only one excited by a given RF. The global magnetic field of the scanner is then expressed as:

$$B(t) = G_0 + xG_x(t) + yG_y(t) + zG_z(t) \tag{3.4}$$

where $G_x(t), G_y(t), G_z(t)$ are the linear gradients, x, y, z the spatial coordinate and $B(t)$ the global magnetic field which evolves along the acquisition. Applying a $G_z(t)$ magnetic field selects an entire slice excited for one RF, its Larmor frequency, which is different from that of the other slices. Then the two other gradients $G_x(t)$ and $G_y(t)$ are applied to the excited slice not simultaneously which leads to a phase difference $\theta_{x,y}$ and gives to the receiver coil the following signal:

$$s(t) = \int f(x,y)e^{2i\pi\theta_{x,y}} \tag{3.5}$$

where $s(t)$ is the signal received in the Fourier space, also named k-space. From this signal it is possible to recover images with contrasts between tissues depending on acquisition parameters (mainly TE and TR). In the following, we will see how the magnetic gradient field can be used to report the diffusion within the tissues.

3.2.2.2 Pulse gradient spin echo

The magnetic field gradient used to perform slice selection and phase encoding is too small to measure the aforementioned diffusion effect. A much stronger gradient

is applied in DWI sequences, named pulse gradient spin echo (PGSE), to highlight water diffusion. After the RF pulse, the slice excited is subject to a strong linear gradient during a very short time δ. The spins have thus a positive or negative extra-phase according to their position. Then, after a diffusion time $\Delta - \delta \gg \delta$, the opposite gradient is applied to bring back spins to their original phase.

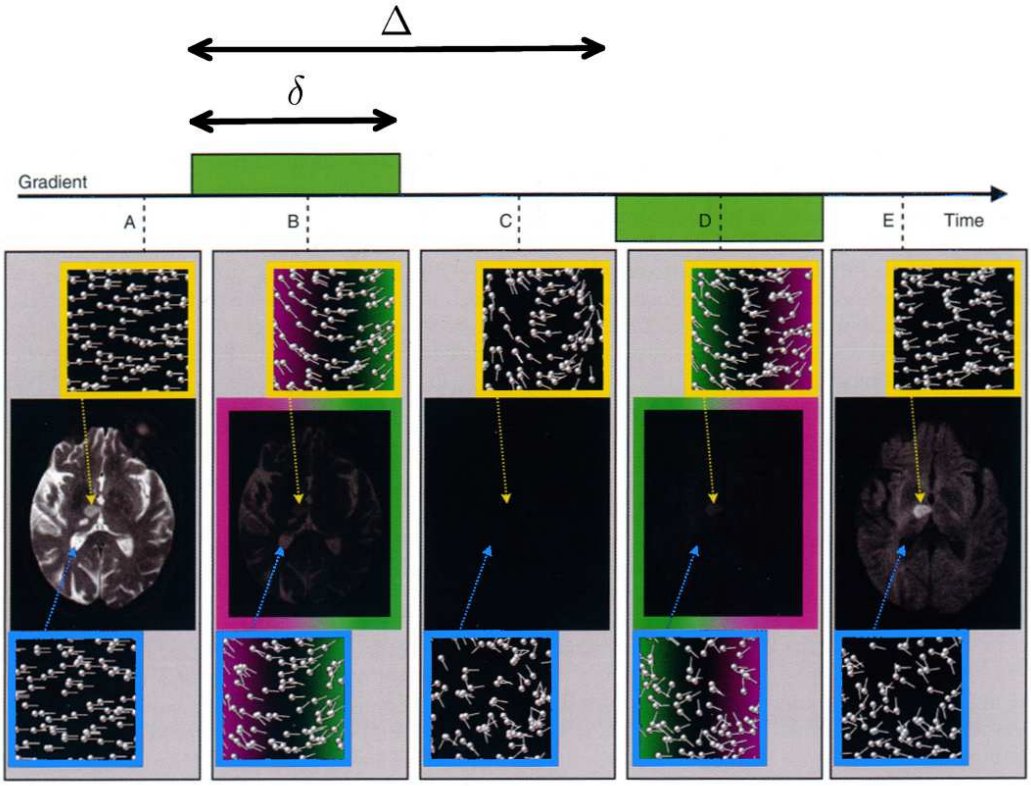

Figure 3.6: After RF application spins are in phase (A). Then a strong gradient adds a positive or negative phase to the spins according to their position (B). During the diffusion time (C), spins do not move (yellow) or lose coherence (blue) depending on the diffusion coefficient of the tissue. After the application of the opposite gradient (D), spins get back in phase and conserve an important net flux (E yellow), or stay incoherent with a low net flux (E blue). *Courtesy from pipe [Johansen-Berg 2009]*

In the illustration of this phenomenon in Fig 3.6, the yellow area is in a low diffusion area. The assumption $\Delta - \delta \gg \delta$ makes the diffusion during the gradient application negligible. During the diffusion time, spins do not move too much and get back in phase after the opposite gradient application. Thus the lesion has a strong brightness in the recovered image. On the contrary, the ventricles in the blue area, are composed of free water with a high diffusion coefficient. During the diffusion time, spins lose phase coherence and stay incoherent after the opposite gradient application. Then the net flux is low and the recovered signal is very low.

From a signal without any gradient S_0, which produces an image called b_0 and

one signal $S_{g,b}$ acquired with a unit gradient $g \in S^2$ and a corresponding b-value b, we define the signal attenuation as:

$$A_{g,b} = \frac{S_{g,b}}{S_0} \tag{3.6}$$

$$A_{g,b} = e^{-bD} \tag{3.7}$$

where D is a ADC in direction g and b is a quantity called b-value defined as:

$$b = \gamma^2 G^2 \delta^2 (\Delta - \frac{\delta}{3}) \tag{3.8}$$

where G is the gradient amplitude, δ is the gradient application time and Δ is the sum of gradient and the diffusion time as illustrated in Fig 3.6. The ADC can be recovered directly using Eq 3.7:

$$D = \frac{-\log(A_{g,b})}{b} \tag{3.9}$$

This relation gives the diffusion in the gradient direction. However, this is not sufficient to estimate the ADC in a 3D space. From 3 gradient directions, it is possible to estimate a global ADC independent of the gradient direction, also called mean diffusivity (MD). Since the brain is an organ with highly orientated structures, several images acquired with different gradient directions are required to correctly model the 3D diffusion. The description of the complete water diffusion probability density function (PDF) in the entire space, name ensemble average propagator (EAP), is theoretically possible through a Fourier transform [Ning 2015]:

$$p(x) = \int_{q \in \mathcal{R}^3} A_{g,b} e^{-2i\pi <q.x>} \, dq \tag{3.10}$$

where q belong to the space defined by the gradient direction, called q-space.

The most famous model named DTI estimates, in each voxel, a tensor diffusion which is a 3D Gaussian distribution with 6 parameters. The DTI is described in details in Section 3.3. For now, let us note that at least 6 acquisitions with different gradient directions and one b_0 image are required to estimate this model. If seven acquisitions is the theoretical minimum, it is generally 30, 90 or more images with several b-values which are acquired to reduce noise influence or to estimate complex models such as diffusion spectrum imaging (DSI) described in Section 3.4.2.1 or MCM described in Section 3.5.

3.2.3 Acquisition strategies

A classic MRI sequence to produce a T2-weighted image is made line by line. The corresponding acquisition time is proportional to the TR and ranges typically around 5 minutes [Serrai 2005]. With this type of sequences, 30 acquisitions would take 150 minutes which is impossible in a clinical use. MRI sequences used for diffusion therefore need an accelerated sequence. The most used one, named EPI, allows to

acquire 30 gradient directions in 3 or 4 minutes. With this short acquisition time come artifacts on the recovered image. The acquisition strategy and the diffusion modeling are then two separate problems, then latter will be discussed in Sections 3.3, 3.4, 3.5.

3.2.3.1 Single-shot acquisition sequences

During an MRI sequence, the signal is acquired in the Fourier domain named k-space. At the end of the acquisition, the signal is reconstructed applying a 2D or 3D inverse Fourier transform depending on the acquisition. In a conventional pulse gradient sequence, the signal in the k-space is acquired line by line. To improve the acquisition time, single-shot methods which acquire the entire image slice by slice have been developed (see Fig 3.7 for illustration). With the growing interest of the medical community for diffusion MRI, several single-shot methods has been proposed [Ahn 1986, Hennig 1986, Meyer 1992, Liu 1996]. The most commonly used in clinical practice, the echo planar imaging (EPI), allows to acquire an entire image in seconds rather than minutes [Stehling 1991].

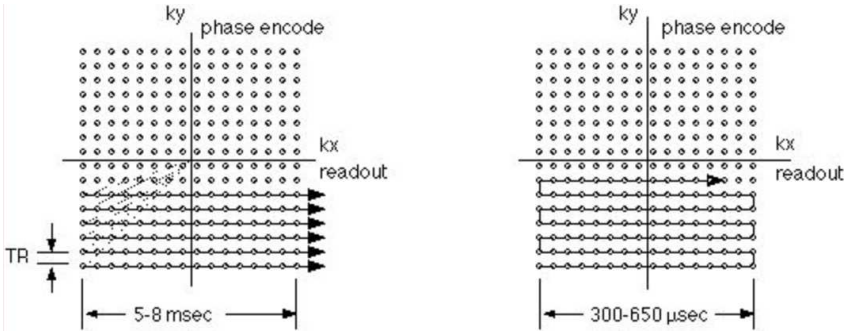

Figure 3.7: Illustration of the signal recovery in the k-space on pulse gradient sequences. On the left: conventional sequence acquired line by line. On the right: EPI which acquires an entire slice in a single-shot. *Courtesy from Tuch [Tuch 2003]*

Unfortunately, single-shot acquisition sequences also deteriorate the quality of the acquisition. Indeed, despite the regular improvements of scanners and acquisition techniques, several artifacts specific to single-shot sequences still affect images.

3.2.3.2 Artifacts

The rapid switch of strong gradients induces Eddy currents (also named Foucault currents) in the electrically conductive structure of the scanner [Jezzard 1998, Reese 2003]. In conventional MRI the gradients are applied with a weak intensity for a short time, resulting in a self compensation of the induced Eddy currents [Johansen-Berg 2013]. On the contrary, in dMRI, the applied gradient can be different than the prescribed one owing to high Eddy current. Furthermore, Eddy currents are time varying and thus do not affect the entire image in the same way. The resulting diffusion mod-

els estimated from the DWI sequence therefore have misregistration artifacts with respect to conventional MRI sequences.

A map of the off-resonance frequency at each voxel, named a field map [Funai 2008], can be used to describe Eddy currents effects and correct them [Jezzard 1998]. Another method models the spatial and temporal evolution of Eddy currents [Rohde 2004]. A different approach proposes the acquisition of an image with an opposite PED and uses the characteristic of the gradient with reversed polarity to correct the Eddy current distortions [Bodammer 2004].

A different distortion artifact induced by the magnetic field inhomogeneity affects EPI images. This artifact leads to locally deformed images, their intensities being modified depending on this deformation. We describe this artifact and how to correct for it in Chapter 4.

An other artifact specific to dMRI named Johnson noise or noise floor occurs depending on the b-value [Jones 2004]. High b-value means a low signal that is thus strongly affected by the background noise. The signal is corrupted by a Rician noise distribution that affects principally the low diffusion region. This causes underestimation of the tensor and anisotropy. A method exists to correct the MD and the anisotropy based on dyadic tensor (specific tensor product) [Basser 2000]. Alternative approaches propose to apply an anisotropic smoothing kernel [McGraw 2004, Tabelow 2008].

3.3 Diffusion Tensor Imaging

3.3.1 Model description

As we saw in Section 3.2, from 2 acquisitions, one with the application of a gradient and one without, it is possible to estimate the ADC in the direction of the gradient. This measure is useful in areas where isotropic diffusion occurs. However, in anisotropic diffusion areas, the ADC in a unique direction does not represent the complexity of the tissue. To do so, the diffusion tensor imaging (DTI) model represents, in each voxel, the diffusion PDF as a 3D Gaussian distribution parameterized by a symmetric matrix:

$$D = \begin{pmatrix} d_{xx} & d_{xy} & d_{xz} \\ d_{xy} & d_{yy} & d_{yz} \\ d_{xz} & d_{yz} & d_{zz} \end{pmatrix} \tag{3.11}$$

This 3D model, one of the the simplest to represent anisotropic diffusion, is also the most used in clinic. The advantage of such a description is that it makes easy to visualize it using its isosurface of probability (as ellipsoid) (see Fig 3.8). It also provides straightforward parameters of the tissue microstructure (see below). The DTI, as there are 6 unknown parameters in the Gaussian covariance matrix, is estimated from at least 6 DWI. More generally, we consider n DWI. For each DWI, the b-values and gradients are now represented by a 3D vector B:

(a) (b) (c)

Figure 3.8: Illustration of an isotropic tensor (a) and two anisotropic tensors (b-c)

$$B = \sqrt{b_0} g \tag{3.12}$$

The signal is represented by a 3D Gaussian distribution and Eq 3.7 becomes:

$$A_{g,b} = e^{-B^\top DB} \tag{3.13}$$

The diffusion tensor D can thus be recovered as the solution of an inverse problem. From at least seven DWI, various solutions exist to recover D [Basser 1994, Landman 2007, Wang 2004, Chang 2005]. The estimation of the diffusion model is beyond our subject, a simple method to perform the DTI estimation is to see the problem as a linear least square on the logarithm of $A_{g,b}$ [Koay 2006]. This estimation of the diffusion tensor offers an analytic expression and hence allows a fast and simple computation.

3.3.2 DTI scalar microstructure properties

A diffusion tensor is characterized by its eigenvalues and eigenvectors and can be expressed as:

$$D = R^\top PR \tag{3.14}$$

where $R \in SO(3)$ is a rotation matrix of the special orthogonal group grouping the eigenvectors and P is a diagonal matrix of the eigenvalues. The largest eigenvalue of P, λ_1, also called the axial diffusivity (AD) and denoted $d_\parallel$, characterizes the ADC in the principal direction of diffusion. The radial diffusivity (RD) is computed as the mean of the two lowest eigenvalues λ_2 and λ_3. From these 3 eigenvalues, several scalar measures are derived to characterize the diffusion.

The mean diffusivity (MD) (or mean ADC) $\hat{\lambda}$ is the average of the diffusion in all directions:

$$\hat{\lambda} = \frac{\lambda_1 + \lambda_2 + \lambda_3}{3} \tag{3.15}$$

The MD is useful to quantify in a global scalar index of diffusion in the brain without direction consideration. It is generally the first biomarker observed and is similar for gray and white matter in adult brain [Johansen-Berg 2009]. MD is used in clinic to detect edema, ischemic strokes [Lythgoe 1997] or discern necrosed glioblastomas and cystic metastatic tumors for example [Toh 2011]. However, the MD does not

quantify the anisotropy of diffusion, which is crucial to highlight the structure of the brain, particularly inside the WM. The fractional anisotropy (FA) is thus defined to characterize the anisotropy as:

$$FA = \sqrt{\frac{3((\lambda_1 - \hat{\lambda})^2 + (\lambda_2 - \hat{\lambda})^2 + (\lambda_3 - \hat{\lambda})^2)}{2(\lambda_1^2 + \lambda_2^2 + \lambda_3^2)}} \tag{3.16}$$

This measure ranges between 0 and 1 where 0 represents an isotropic tensor and 1 a complete anisotropic tensor which is degenerated. WM injury through demyelination in the brain can be evaluated by measuring as FA, AD, RD. This loss of WM integrity plays a role in disorder as major depressive disorder (MDD), obsessive-compulsive disorder (OCD), autism, MS, epilepticus [Lucchinetti 2000, Kutzelnigg 2005, White 2008, Song 2002, Budde 2009, Soares 2013, Wieshmann 1997].

3.3.3 DTI limitations

As we see, the DTI is easy to estimate and it is still very used in clinic for many diseases. However the simplicity of the DTI also holds limitations. A voxel size is typically around 8 mm^3, this cube in a normal brain can include white matter (WM), grey matter (GM), glial cells, cerebrospinal fluid (CSF) ... The diameter of an axon is between 1 and 10 μm, the scale difference between the signal observed and the structure we want to describe is huge. Thus the diffusion in complex areas, as in WM crossing fibers, cannot be represented by a tensor. This phenomenon is illustrated in Fig 3.9. Tensors correctly represent the structure when all fibers have the same orientation but in the crossing areas the tensor is represented as isotropic in the plane of the crossing fibers. Thus, it is not possible to distinguish a crossing fiber or a free diffusion area with the DTI.

Moreover, the parameters as FA, MD are entangled. A change in the microstructure is characterized but not well described. This can be explained as an increment of the water proportion or a diminution of myelin that can provide similar effects on these biomarkers. Hence they do not correctly describe what is really happening within the brain microstructure.

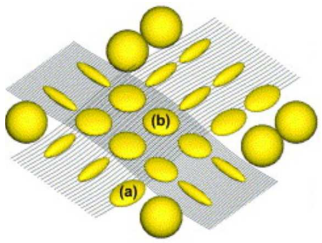

Figure 3.9: Crossing fibers and the corresponding tensors. In (a) the principal orientation of the tensor is correct, in (b) the tensor is isotropic in the crossing plan, thus it is not possible in the crossing area to know if the DTI represents a free water diffusion or a crossing fiber. *Courtesy of Park [Park 2005]*

More complex models have been developed to address these issues that will be presented in Section 3.4, 3.5. First we present a state of the art on tensor interpolation.

3.3.4 Tensor interpolation

To perform statistics on DTI, either to compare two populations or a patient to a group in a voxel-wise manner, a registration step is required. Indeed for all the acquisitions, even within the same study, patients are not at the same exact position and geometric acquisition parameters are different. Moreover the variability of the brain between individuals implies that there is no way to compare to images without a registration step apart from time consuming regional ROI selection and evaluation. Independently of the algorithm used to perform registration, the original images need to be interpolated. In the case of DTI images, we want to average Gaussian PDFs and to do so several methods have been proposed.

A Gaussian PDF is defined by its covariance matrix that belongs to $S_3^+\{\mathbb{R}\}$, the space of positive-define matrices which is an open subset convex cone of $S_3\{\mathbb{R}\}$ the set of symmetric matrices.

3.3.4.1 Euclidean average

The simplest way to average tensors is to use the Euclidean distance between the covariance matrices as:

$$d_{\text{Eucl}}(T_1, T_2) = ||T_1 - T_2||_F \tag{3.17}$$

where $||.||_F$ is the Frobenius norm, and T_1, T_2 are the two Gaussian covariance matrices. Thus the weighted sum of n tensors $\{T_i\}_{i=1,..,n}$ is the one which minimizes the weighted distance using the Frechet mean:

$$\hat{T} = \arg\min_T \sum_{i=1}^{n} w_i \; d_{\text{Eucl}}(T_i, T) \tag{3.18}$$

where w_i are their corresponding weights. In this case, the weighted sum is directly expressed as:

$$\hat{T} = \sum_{i=1}^{n} w_i T_i \tag{3.19}$$

Unfortunately, that method is not well adapted to the space of positive-define matrices because the average of tensors can present a swelling effect [Batchelor 2005, Pasternak 2010]. To avoid these issues, several methods have been proposed based on Riemannian frameworks. We first review some mathematical notions to introduce these tensor interpolation methods.

3.3.4.2 Riemannian manifold

A Riemannian manifold M is a smooth space equipped with a Riemannian metric which generalizes the notion of curve and distances defined in the classic Euclidean geometry. The Riemannian manifolds have been largely studied since the 19th century, many books being dedicated to describe their properties [Wolf 1967, Boothby 1986, Lee 2006, Chavel 2006]. For each point x of M, an inner product equips the corresponding tangent space T_xM. The neighborhood around the origin of the tangent space is called an exponential map. The smoothness of the variation of the tangent spaces allows to associate to each smooth curve $\gamma(t) : [0,1] \to M$ a length derived from the tangent vector of the curve as:

$$L_\gamma(a,b) = \int_a^b (< \gamma'(t), \gamma'(t) >_{T_{\gamma(t)}M})^{\frac{1}{2}} dt \tag{3.20}$$

where L is the length between two points a and b, γ' is the derivative of the curve in the tangent space (see an illustration Fig 3.10) and $< ., . >_{T_xM}$ the inner product of the tangent space. A geodesic in a space thus defines the shortest way between two points as:

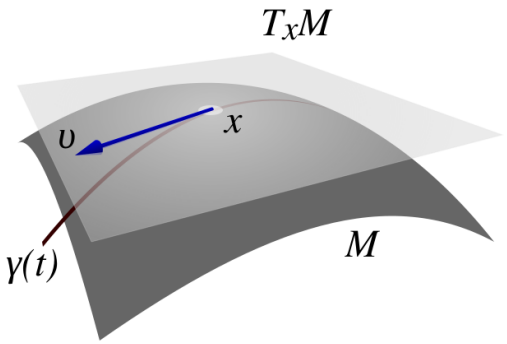

Figure 3.10: Illustration of a curved Riemannian space with a tangent space T_xM defined for a point x (*common license* https://en.wikipedia.org/wiki/Tangent_space).

$$d(a,b) = \inf_{\gamma \in \mathcal{F}([0,1]:\to\mathbb{R})} \int_a^b (< \gamma'(t), \gamma'(t) >_{T_{\gamma(t)}M})^{\frac{1}{2}} dt \tag{3.21}$$

where inf is the infimum of all the curves γ on the manifold. Any Riemannian manifold can be associated with different metrics. Between two points at least one geodesic exists even if, contrarily to the classic Euclidean metric, no uniqueness is guaranteed.

3.3.4.3 Matrix operations

To use a Riemannian framework for DTI, we first need to express some operations on matrix spaces $M_n(\mathbb{R})$. The exponential of a matrix is defined as the infinite sum:

$$e^X = \sum_{k=0}^{\infty} \frac{X^k}{k!} \tag{3.22}$$

This series converges for any $X \in M_n(\mathbb{R})$, thus e^X is well-defined for all $X \in M_n(\mathbb{R})$ [Hall 2015]. The logarithm of a matrix, which is the inverse of the exponential: $\log(\exp(M)) = M$, is not always defined in the general case. However a tensor is characterized by its covariance matrix that belongs to $S_3^+\{\mathbb{R}\}$ (the space of positive-definite matrices). In that space, the matrix logarithm always exists and is uniquely defined [Culver 1966]. In particular, let $X \in S_3^+\{\mathbb{R}\}$, there is an eigen decomposition in a orthonormal basis as:

$$X = R^\top D R \tag{3.23}$$

where R is an orthogonal matrix containing the eigenvectors of X and D is a diagonal matrix containing the eigenvalues of X. Then, for any $k \in [0, \infty[$

$$X^k = (R^\top D R) \underbrace{...(R^\top D R)...}_{k \text{ times}} (R^\top D R) \tag{3.24}$$

given that $R^\top R = I_3$ the identity matrix, we obtain:

$$X^k = R^\top D^k R \tag{3.25}$$

The exponential of X is thus expressed as:

$$e^X = \sum_{k=0}^{\infty} \frac{R^\top D^k R}{k!} = R^\top \left(\sum_{k=0}^{\infty} \frac{D^k}{k!} \right) R \tag{3.26}$$

$$e^X = R^\top e^D R \tag{3.27}$$

where e^D is the exponential of D which corresponds to the exponential of the diagonal elements of D. With this expression, the logarithm is uniquely defined as:

$$\log(X) = R^\top \log(D) R \tag{3.28}$$

with $\log(D)$ containing the logarithm of the diagonal elements of D which is well defined since all eigenvalues are positive.

3.3.4.4 Affine-Invariant Riemannian metric

A Riemannian metric for tensors has been proposed based on a geodesic in the matrix log-space [Pennec 2006]. Interestingly, the method of information geometry [Amari 2007] derived on Gaussian probability density function (PDF) resulted in the same mathematical framework [Lenglet 2006]. This metric is defined to be invariant to any affine action on the tensor space, i.e:

$$< X, Y >_P = < A * X, B * Y >_{A*P} = \mathrm{Tr}(P^{\frac{-1}{2}} X P^{-1} Y P^{\frac{-1}{2}}) \tag{3.29}$$

where Tr is the trace operator, X and Y are two tangent vectors to the manifold P and A is a left operator defined as:

$$A * X = AXA^T \tag{3.30}$$

This represents a solid theoretical mathematical framework which is affine invariant and conserves the determinant of the tensor. With this invariant metric, the exponential map associated at each point of the manifold is defined using the matrix exponential:

$$\exp_P(X) = P^{\frac{1}{2}} \exp\left(P^{\frac{-1}{2}} W P^{\frac{-1}{2}}\right) P^{\frac{1}{2}} \tag{3.31}$$

This expression also determines the inverse mapping with a one to one correspondence, so it is easy to come back to the matrix space. The mean T of a set of tensors $X_1, ..., X_n$ is unique because the manifold has a-non positive curvature [Kendall 1990] and is the one that minimizes the sum of the squared distances (Frechet mean). It can be recovered following a gradient scheme:

$$T_{m+1} = T_m^{\frac{1}{2}} \exp\left(\frac{1}{n} \sum_{i=1}^{n} \log(T_m^{\frac{-1}{2}} X_i T_m^{\frac{-1}{2}})\right) T_m^{\frac{1}{2}} \tag{3.32}$$

At each iteration, the mean is computed as the exponential map corresponding to the point of the previous step and is reprojected to the main manifold. As there is no analytic expression, finding a minimum takes time, even if this algorithm converges quickly [Fletcher 2004]. In this mathematical framework, the determinant, i.e the eigenvalues product, is conserved. Thus the average tensor does not suffer from a swelling effect as the Euclidean mean.

3.3.4.5 Geodesic-loxodromes

Another algorithm based on *geodesic-loxodromes* has been proposed later [Kindlmann 2007]. A loxodrome, very useful in navigation, is a road that crosses all meridians with a constant angle (see Fig 3.11), the famous *Mercator projection* is the first representation that draws every loxodrome as a straight line [Floater 2005]. In mathematical terms, the constraints on the curve are expressed as:

$$\forall t \in [0, 1], \quad |\gamma(t)'| = 1, \quad \gamma'(t).n(\gamma(t)) = \alpha \tag{3.33}$$

with α constant and $n(\gamma(t))$ a normalized vector pointing a constant direction. This method offers interesting properties: it conserves MD and FA instead the tensor determinant. Despite these trumps, as for the affine-invariant Riemannian method, a gradient descent is necessary to estimate the weighted average of tensors. For a classic image with more than 1 million voxels, the computation time can be really expensive.

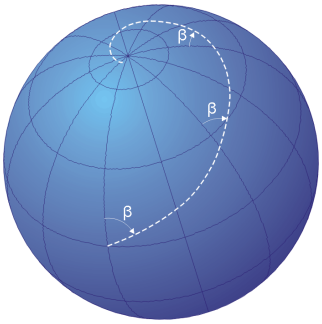

Figure 3.11: Illustration of a loxodrome around a sphere. *Common license, https://en.wikipedia.org/wiki/Rhumb_line*

3.3.4.6 Log-Euclidean

Therefore we next focus on a fast method proposed by Arsigny et al. based on log-Euclidean metrics [Arsigny 2006]. $S_3^+\{\mathbb{R}\}$ is a Lie group whose tangent space is a vector space structure equipped with a logarithm multiplication $\odot$ and a scalar logarithm multiplication $\circledast$:

$$T_1 \odot T_2 = \exp(\log(T_1) + \log(T_2)) \tag{3.34}$$
$$\lambda \circledast T = \exp(\lambda \log(T)) \tag{3.35}$$

where λ is a scalar, T, T_1 and T_2 belong to $S_3^+\{\mathbb{R}\}$. We can notice that I_3 is the neutral element of the logarithm multiplication. $S_3^+\{\mathbb{R}\}$ has a Lie group structure with the logarithm multiplication. From these properties, the distance between two tensors is given by:

$$d_{(Log-Eucl)}(T_1, T_2) = ||\log(T_1) - \log(T_2)||_F \tag{3.36}$$

From this distance, the mean T of a set of tensors $T_1, ..., T_n$ with their corresponding weights $w_1, ..., w_n$ is directly given by:

$$T = \exp\left(\sum_{i=1}^{n} w_i \log(T_i)\right) \tag{3.37}$$

Compared to the affine-invariant framework and the *geodesic-loxodrome*, this expression is very simple and thus the corresponding computation time is much shorter. This framework does not have the affine-invariance property but the determinant of the tensor is conserved. Moreover, several successive computations can be all done in the log-Euclidean space without coming back to the matrix space between each.

The Euclidean, the affine-invariant, and the log-Euclidean interpolation results are compared on the weighted interpolation of two tensors in Fig 3.12. The Euclidean tensor average suffers from an important swelling effect at the middle of the average. The affine-invariant and log-Euclidean averages conserve the determinant, the log-Euclidean average shows a more anisotropic structure than the affine-invariant. For

both methods, the product of eigenvalues is conserved, however the ratio between the first and the second eigenvalues is different. This results in a fattening effect that deforms the shape of the average tensor.

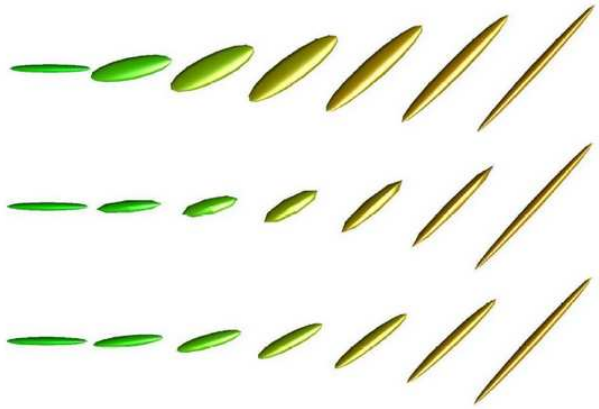

Figure 3.12: Illustration of the interpolation of two tensors. Average tensors in the middle are the results of a weighted average of the two original tensor on the left and on the right. Top line: Euclidean, Middle line: Affine-Invariant, Bottom line: Log-Euclidean. *Image courtesy from Arsigny [Arsigny 2006]*

3.3.4.7 Shape invariant methods

To avoid the fattening effect, some recent studies propose shape-invariant methods [Wang 2014]. The eigen decomposition of a covariance matrix $X = R^\top DR$ is a product of matrices that belong to $SO_3(\mathbb{R})$, the orthogonal group and $D_3(\mathbb{R}) \cong (\mathbb{R}_*^+)^3$, the group of diagonal matrices with positive eigenvalues. A geodesic can be created as the product of two geodesics in each space $SO_3(\mathbb{R})$ and $D_3(\mathbb{R})$. The shape of a tensor is entirely described by the eigenvalues of D. Therefore, the shape of an average tensor is determined by the geodesic on the shape of the original tensors, which is independent of their orientation. Unfortunately, this method is not related to a Frechet mean and thus is less well defined for multiple tensors interpolation [Feragen 2016].

3.4 Models based on orthogonal basis

Now, we present an other type of models based on the decomposition of the signal in an orthogonal basis. These type of methods are classic to perform image processing. Indeed, representation of a signal in a set of orthogonal functions allows to capture, with few coefficients, the main part of the signal. For large bases, in addition to a low storage cost, the application of a simple operation of thresholding could denoise the signal. The popularity of representations produced a lot of bases as the Fourier space [Bracewell 1986], wavelets [Mallat 1989], the curvelet [Starck 2002] and more

others. In the following we present how a set of orthogonal functions can be used to build a diffusion model.

3.4.1 Modified spherical harmonics functions

Orientation distribution functions (ODFs) are used to describe the principal diffusion directions, which can be done using a modified spherical harmonics (SH) orthonormal basis [Descoteaux 2007]. These functions represent main orientations of the signal in the q-space. The gradient applied to each DWI on the 2-sphere S^2 can be expressed with 2 orientation parameters $g = (\theta, \varphi)$. The modified SH basis is described by a set of functions:

$$Y_j(\theta,\varphi) = \begin{cases} \frac{\sqrt{2}}{2}((-1)^m Y_l^{-m}(\theta,\varphi) + Y_l^m(\theta,\phi)), & \text{if } m < 0 \\ Y_l^0, & \text{if } m = 0 \\ i\frac{\sqrt{2}}{2}((-1)^m Y_l^{-m}(\theta,\varphi) - Y_l^m(\theta,\phi)), & \text{if } m > 0 \end{cases} \tag{3.38}$$

where l is the order of the SH basis, $m = -l, ..., l$ is an index, i.e, $j := j(l,m) = l^2 + l + 1 + m$. Y_j is the j-th element of the modified SH basis and Y_i^m is the complex SH value. This basis is designed to be antipodally symmetric, real and orthonormal. Thus the signal from each DWI can be decomposed as:

$$S_i = \sum_{j=i}^{r} c_j Y_l^j(\theta,\varphi) \tag{3.39}$$

where c_j are the decomposition coefficients in the basis and r is the order of the basis. The maximum degree of the basis, l, controls the dimension and therefore the number of modified SH functions $r = \frac{(l+1)(l+2)}{2}$. The degree of the basis defined the number of orientation of the modified SH functions. An illustration of these functions is presented Fig 3.13. For the mathematical background on SH please refer to [Hobson 1931, Müller 2006, Atkinson 2012].

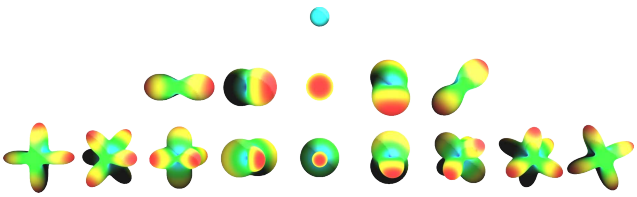

Figure 3.13: The first modified SH functions corresponding to degree $l = 0, 2, 4$ (from top to bottom).

The spherical harmonic functions basis, with a variable number of degrees, can represent any number of diffusion directions (generally 1, 2 or 3) and thus, contrary to DTI, allows to model crossing fibers. On the other hand, this basis only represents the diffusion directions. Therefore we lose microstructure information such as diffusivity. A tractography, which only considers directions, is thus a perfect application for such a representation [Descoteaux 2009].

Moreover, an orthogonal basis offers good mathematical properties. As for tensors, a Riemannian framework performing gradient descent has been developed to interpolate orientation distribution functions (ODF) [Goh 2011b]. An other analytic methods for ODF reorientation reduces the computational complexity of the interpolation[Geng 2009b]. These bases can also be used to perform group comparison for a clinical study. Principal component analysis (PCA) analysis techniques offers a voxelwise comparison [Commowick 2015]. Finally, this method proposed a diffeomorphic registration algorithm used for fiber tractography [Raffelt 2011].

3.4.2 3D bases for ensemble average propagator reconstruction

ODFs only consider the direction of the water diffusion. To estimate the probability of the water displacement in the entire $\mathbb{R}^3$ space, we need to consider other models. In the following, we quickly present several models that allow the reconstruction of the EAP and thus are able to better describe the brain microstructure.

3.4.2.1 Diffusion spectrum imaging

The simplest way to consider an orthogonal basis from DWI acquisitions is to consider the entire q-space. A classic DWI is composed of several pulse sequences measured on the q-space. The acquisition is acquired from a homogeneous repartition of gradients applied to one or several shells for a total between 30 and 100 images. On the other hand, a diffusion spectrum imaging (DSI) acquisition covers the entire q-space with a 3D grid[Tuch 2002]. This results in a huge number of gradients applied (around 500) with different b-values for almost all of them. Here, the function basis is the q-space and the PDF can directly be estimated from it with a 3D discrete Fourier transform [Wedeen 2005].

$$p(x) = (S_0)^{-1}\mathcal{F}^{-1}(S_g) \tag{3.40}$$

where $\mathcal{F}^{-1}$ is the inverse Fourier transform and p is the PDF of water diffusion.

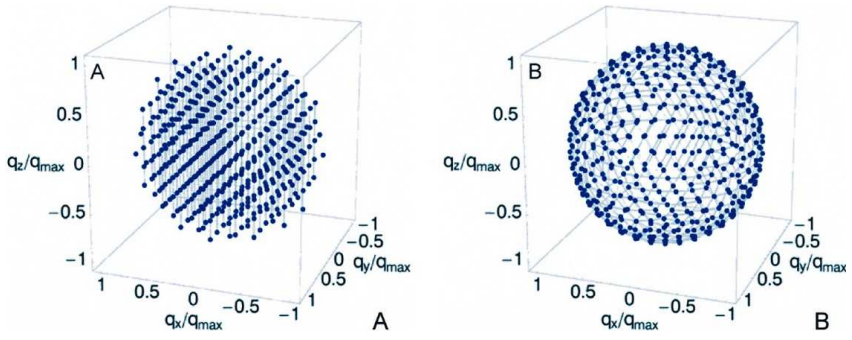

Figure 3.14: Illustration in the q-space of: (A) a DSI grid acquisition, (B) a HARDI acquisition. *Courtesy of Tuch [Tuch 2003]*

Such DSI sequences offer a high angular reconstruction with an acquisition time still too expensive for a clinical use. However, several acquisition schemes based

on compressed sensing reduce the acquisition time offering new possibilities for this type of sequences [Menzel 2011, Bilgic 2012].

3.4.2.2 Q-space based functions

Other methods are based on the reconstruction on the signal from the entire q-space [Assemlal 2009]. The multiple q-shell diffusion propagator imaging (mq-DPI) proposes, as the ODFs, the use of modified SH functions [Descoteaux 2011]. An extension of this work using spherical polar Fourier (SPF) basis, a subset of the modified SH basis, provides better continuity and regularization properties [Caruyer 2012]. It is able to reconstruct information about radial diffusion and need less acquisitions than the DSI . From a multiple shell acquisition, the EAP can be analytically reconstruct using the Laplace equation [Spiegel 1991]. From the EAP expression, it is possible to obtain the ODFs as previously. Moreover, the return-to-origin (RTO) probability has an analytic expression:

$$RTO = b_{\max}^2 \left(c_0 + \frac{2 d_0 b_{\max}}{3} \right) \sqrt{\pi} \tag{3.41}$$

where $b_{\max}$ is the gradient strength, c_0 and d_0 are functions of coefficients of the signal in the modified SH basis. This measure is a propagator feature that includes both radial and axial diffusion informations into a scalar map.

3.5 Multi-Compartment models

3.5.1 General description

We have seen several models based on a decomposition on a orthogonal basis. Now we consider multi-compartment model (MCM), an other class of models that decomposes the water diffusion PDF as a weighted sum of compartments. These models do not have orthogonal properties and are designed to finely describe the microstructure of the brain. In return, they have complex PDF expressions, and thus, the corresponding mathematical framework from estimation to interpolation becomes harder. A MCM PDF is decomposed as:

$$p(x) = \sum_{i=1}^{n} w^i \; p^i(x) + \sum_{j=1}^{m} w_{\text{iso}}^j p_{\text{iso}}^j(x) \tag{3.42}$$

where p^i are the PDFs of anisotropic compartments, p_{iso}^j the PDFs of isotropic compartments and w^i, w_{iso}^j are the compartment weights with the constraint:

$$\sum_{i=1}^{n} w^i + \sum_{j=1}^{m} w_{\text{iso}}^j = 1 \tag{3.43}$$

Before considering the isotropic and anisotropic compartments, we can note that the expression of MCMs has an intrinsic compatibility advantage with the signal

from the Fourier space. Indeed, the characteristic function ϕ for $p(x)$ is written as the weighted sum of individual characteristic functions:

$$\phi(t) = \sum_{i=1}^{n} w^i \phi^i(t) + \sum_{j=1}^{m} w^j_{\text{iso}} \phi^j_{\text{iso}}(t) \tag{3.44}$$

where $\phi^i(t)$ and ϕ^j_{iso} are the characteristic functions of their corresponding PDFs. According to q-space equations, signal is formed from the PDFs as [Stamm 2013]:

$$A_{g,b} = |\phi(\sqrt{2b}g)| \tag{3.45}$$

The main purpose of MCMs is to model, through several compartments, the microstructure of the brain. Each compartment represents specific diffusion within liquid as CSF but also small structures as axons, glial cells...

An isotropic compartment represents isotropic water diffusion inside the brain. We present the different types of isotropic compartments, what they represent, and their corresponding models in Section 3.5.2.

An anisotropic compartment models a fascicle, i.e a bundle of axons with a similar general direction. A good review of anisotropic compartment has been proposed recently [Panagiotaki 2012]. We introduce several anisotropic compartments models as the multi-tensor model (MTM), diffusion direction imaging (DDI), neurite orientation dispersion and density imaging (NODDI) in Section 3.5.3.

3.5.2 Isotropic compartments

The isotropic compartments represent isotropic water diffusion within a voxel. Thus the diffusion follows a 3D Gaussian distribution:

$$p(x) = \frac{1}{\sqrt{2\pi d}} \exp\left(-\frac{x^\top x}{2d}\right) \tag{3.46}$$

where d is the diffusivity. Isotropic compartments have several possible d values corresponding to different cell types or structures:

Free water. It represents the unconstrained water such as CSF in the ventricles and around the brain parenchyma. The diffusivity of free water, which depends on the temperature, is equal to $d_{\text{free}} = 3.10^{-3}\ mm^2 s^{-1}$ at 37° C [Pasternak 2009, Clark 2000, Harris 1980].

Isotropic restricted water. This type of isotropic compartment models the water inside impermeable spherical glial cells. Water molecules indeed rebound infinitely inside the spherical boundary of the glial cell. This trapped water has a corresponding diffusivity equal to $d_{\text{restricted}} = 1.10^{-3}\ mm^2.s^{-1}$ [Stanisz 1997, Panagiotaki 2012].

Fixed water. Some authors also described water particles stationary inside the walls of the glial cells or stuck into cellular membranes in fixed tissues [Stanisz 1997, Alexander 2010]. In brain anatomy, these molecules probably exist, however our experience of MCMs estimations made on the Human Connectome Project (HCP)

give us a high percentage of stationary water which does not seem realistic. This may reflect a modeling problem or noise type and this behavior is subject to caution.

3.5.3 Anisotropic compartments

Anisotropic compartments represent the water diffusion within and around axons. We call fascicle a group of axons along the same global direction, the axial direction. The set of all axons in a fascicle is named intra-axonal space, the rest of the space is named extra-axonal (see Fig 3.15 for illustration). The extra-axonal space is a complex environment composed by astrocytes, glial cells and extra-cellular molecules [Assaf 2004]. Some MCMs divide the signal attenuation between intra-axonal space $A_{g,\mathrm{I}}$ and extra-axonal spaces $A_{g,\mathrm{E}}$. Three solutions exist to model a fascicle:

- One PDF models the entire anisotropic compartment.
- The independant sum of two random variables: one for intra-axonal and one for extra-axonal spaces. The final PDF is thus expressed as a convolution.
- A weighted sum of two PDFs: one for intra-axonal and one for extra-axonal spaces, therefore the PDF becomes :

$$p^i(x) = w_I^i p_I^i(x) + w_E^i p_E^i(x) \tag{3.47}$$

where p_I^i is the PDF of the intra-axonal space, p_E^i is the PDF of the extra-axonal space and w_I^i, w_E^i their respective weights: $w_I^i + w_E^i = 1$.

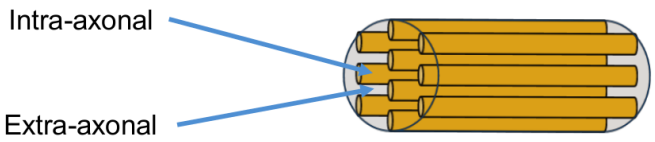

Figure 3.15: Schematic illustration of a fascicle containing a set of axons in the same global direction. The fascicle is divided between the intra-axonal space and the extra-axonal space.

In the intra-axonal space, the water within the axon rebounds against the membrane, thus the global diffusion is more important along the axon than in the perpendicular plane. The ratio between the axial and radial diffusion depends on several parameters:

- **The axon diameter** [Ford 1998]. The water molecules hit statically more quickly the membranes within a very thin axon. Thus the axial diffusion is inversely correlated with the diameter of the axon.

- **The diffusion time**. Along the same idea, when the diffusion time is high, water molecules hit more frequently the membranes. Hence, the FA is higher with a high diffusion time. It is interesting to notice that the b-value is related to the diffusion time and thus impacts the anisotropy of the diffusion model.

These general assumptions do not reflect the complexity of the water molecules behavior. The permeability of the membrane, the presence and the width of a myelin sheath also plays a role, but difficult to quantify in diffusion [Beaulieu 2002].

The water behavior within the extra-axonal space is even more complicated to model and understand. Water within the myelin has a short T2 relaxation time, hence the corresponding ADC is very low and the diffusion is negligible [Brunberg 1995]. However, the rest of the water molecules surrounded by axons will more likely hit the myelin sheath and thus diffuse along the axial direction. The rest of the extra-axonal space is composed of glial cells and astrocytes and the collision of water molecules with such cells is, at least, not obvious to describe.

Therefore, contrarily to the free water diffusion which is well defined and overall accepted in the community, a lot of different models have been proposed to model anisotropic compartments. In the following, we present some of these models, obviously we do not pretend to be exhaustive. Another MCM named diffusion direction imaging (DDI), has been proposed and will be discussed into more details in Section 5.4.2 [Stamm 2013].

3.5.3.1 Tensor model

As we saw in Section 3.3 the anisotropic compartment can be described as a 3D Gaussian distribution. The characterize of which is used to define the acquired signal:

$$A_{g,b} = e^{-B^\top DB} \tag{3.48}$$

This solution allows to represent several fascicles within one voxel and is a straight forward extension of the DTI model, the most used diffusion model. Two simplified versions of the tensor compartment exist:

- **A stick compartment** represents an anisotropic compartment as a degenerated tensor with one principal orientation with corresponding diffusivity. The two lowest eigenvalues are set to 0 [Behrens 2003].
- **A zeppelin compartment** represents a tensor with equal second and third eigenvalues.

The estimation of MCMs is a hard non linear optimization problem. Indeed, in general PDFs do not have an analytic expression. Thus, these particular tensors are frequently used as a proto-compartment to estimate a more complex MCM. One common way to estimate MCM is to fix some parameters in a first time and release them one by one [Stamm 2016]:

- Optimize stick models from randomly picked initial sticks.
- Use it to estimate a zeppelin releasing one eigenvalue.
- Finally, use the ball and zeppelin to compute the MCMs.

The MTM is a combination of isotropic compartments and several tensor compartments. It is estimated step by step with an expensive computation time. Furthermore, the MTM needs at least 2 different b-values to be estimated (as majority of MCM), a single shell leading to an infinite space of solutions [Scherrer 2010]. Hence, its common use in clinic is not realistic yet.

3.5.3.2 NODDI

An other famous MCM developed recently is named NODDI [Zhang 2012a]. This model is made for HARDI acquisitions with at least 2 shells. In NODDI, the anisotropic compartment is separated between the intra-axonal space and the extra-axonal space as in Eq 3.47.

The intra-axonal space is modeled as a set of sticks considering the low radial diffusion inside an axon [Behrens 2003, Sotiropoulos 2012]. Depending on the brain area, the sticks have a low angular dispersion as in the corpus callosum or a large one as in centrum semiovale [Zhang 2012a]. The characteristic function of such a distribution on the sphere is expressed as follows:

$$\phi_I^i(\sqrt{2b}g) = \int_{S^2} f(n) e^{-bd_{\|} <g,n>^2} dn \tag{3.49}$$

where x belongs to the unit sphere S^2, $d_{\|}$ is the axial diffusivity, g the gradient direction and f the distribution around the sphere, modeled as a Watson distribution [Mardia 2009]:

$$f(x) = M\left(\frac{1}{2}, \frac{3}{2}, \kappa\right)^{-1} e^{\kappa <\mu,x>^2} \tag{3.50}$$

where M denotes the confluent hypergeometric function of Kummer [Lewin 1991], μ is the mean direction and κ a concentration parameter around μ. The Watson distribution offers a good representation for both high and low dispersion.

The extra-cellular space is also represented by a model of orientation-dispersed cylinders as:

$$\log\left(\phi_E^i\left(\sqrt{2b}g\right)\right) = -bg^\top \left(\int_{S^2} f(n) D(n) dn\right) g \tag{3.51}$$

where $D(n)$ is a cylindric symmetric tensor with n as principal orientation and f a Watson distribution.

NODDI is a simplification of a previous model which required a more complex protocol and estimation time [Zhang 2011]. As proposed in the original paper [Zhang 2012a], the global MCM NODDI comports one isotropic compartment and

only one such anisotropic compartment with separate intra-axonal and extra-axonal spaces. It demonstrates a good ability to represent the dispersion orientation among a fascicle. However, with one anisotropic compartment, it is not optimal to model crossing fibers, although it is possible to add other anisotropic compartments to do so.

3.5.3.3 CHARMED

A last popular anisotropic compartment model named Composite Hindered And Restricted Model of Diffusion (CHARMED) has been proposed [Assaf 2004, Assaf 2005]. As NODDI, it separates the anisotropic compartment between intra-axonal and extra-axonal spaces.

In the intra-axonal space, the diffusion in the axial direction is considered as free and is thus represented by a classic 1D Gaussian distribution, a stick. Contrary to other models, CHARMED does not assume that the gradient application time δ is small enough to not affect the diffusion and hence attempts to model it. This results in a more complex cylindrically restricted distribution for the radial diffusion in intra-axonal space [Neuman 1974, Assaf 2004].

For the extra-axonal compartment, the model assumes a 3D Gaussian distribution, i.e a tensor. CHARMED is adaptable as it allows several anisotropic compartments with intra and extra-axonal spaces. In addition to that, it previously corrects the Johnson noise using [Pierpaoli 1996]. Few years later, the same authors extended this work with AxCaliber, another anisotropic compartment model, that considers the axon diameters as a free parameter to estimate [Assaf 2008].

Chapter 4

Distortion correction of echo planar images

Contents

4.1 Introduction

In recent years, single-shot echo planar imaging (EPI) has been increasingly used as it is substantially faster than most other acquisition sequences. The high speed of this acquisition comes from the fact that images are acquired within a single-shot instead of multiple shots (single or multiple echoes) in other classical sequences (Gradient Echo, Spin Echo...). With respect to the required relaxation time between each shot, the single-shot method saves a considerable acquisition time. By shortening the acquisition time of every single time frame, EPI enables the acquisition of a larger number of images than other methods while respecting the same clinical constraint. This is particularly useful for diffusion-weighted magnetic resonance imaging (DWI) wherein the acquisition of several scalar images

is required to represent the underlying microstructure of the brain (white matter mainly) [Ferizi 2014b, Zhang 2012b, Stamm 2012a, Taquet 2014]. For this reason, EPI is the most common sequence used for DWI [Johansen-Berg 2009]. For similar speed reasons, EPI is also used for functional imaging [Huettel 2004], which requires the fast acquisition of many brain images while a task is executed by the subject.

The high velocity of EPI acquisitions comes at the cost of a high sensitivity to magnetic field inhomogeneities. Affected areas, often located at the tissue interfaces with different magnetic susceptibilities such as bone or air, are either contracted or dilated along the PED [Jezzard 1995] (moreover, measured tissue intensities in these regions change due to the local transformation). Therefore the brain anatomy in EPI does not match with structural images that are much less sensitive to distortions. Such a correspondence is however critical as a joint analysis is often performed for these modalities: 1- for diffusion imaging, structural images are used to define regions of interest for fiber tracking or to extract lesions that are to be linked to brain microstructure properties ; 2- for fMRI, activations are computed on low resolution EPI to speed up acquisition time and need to be aligned with a high resolution T1w image at least for interpretation and visualization of activated regions in the brain. In both cases, it is therefore necessary to perform EPI distortion correction as non linear anatomy mismatch between the modalities will lead to biased results. Computing such a distortion correction is still an open problem, especially in regions where large deformations occur.

As the distortion in EPI acquisitions comes from the B_0 field inhomogeneities, the first technique for distortion correction relies on the acquisition of a B_0 field map [Jezzard 1995, Reber 1998]. This map is in turn used to infer the local contractions and dilations, and correct EPI intensities. This field map however needs to be smoothed to avoid noise corruption and may therefore be unable to provide sufficient correction in severely distorted areas [Holland 2010, Wu 2008].

Other techniques have considered new sequences using point spread functions (PSF) to obtain acquisitions with no distortion. This category includes works by Robson et al. [Robson 1997], Chung et al. [Chung 2011] and Zaitsev et al. [Zaitsev 2004]. Unfortunately such sequences are not currently available on all scanners.

A third class of methods considers the acquisition of two EPI sequences with opposite phase encoding directions – one anterior-posterior and one posterior-anterior for example – to correct for distortion. This class of techniques, initially proposed by Chang and Fitzpatrick [Chang 1992] and Bowtell et al. [Bowtell 1994], relies on the computation of a distortion field from the two images to correct the EPI. Several methods use this technique: Andersson et al. [Andersson 2003] used a pair of reversed EPI in conjunction with a discrete model of image formation for spin-echo EPI. An implementation called TOPUP is available in the FSL package[1]. Voss et al. [Voss 2006] introduced an algorithm to estimate, from the two images, the correction displacement field based on cumulative intensity distributions along each line in the PED. This simple method strongly reduces the distortion, however it is

[1] http://fsl.fmrib.ox.ac.uk/fsl/fslwiki

sensitive to noise and the computed transformation needs to be smoothed, leading to a trade-off between regularity and precision. Other methods in this category include Morgan et al. approach [Morgan 2004], using continuously alternating phase encoding, Weiskopf et al. method [Weiskopf 2005] using a modified multi-echo EPI acquisition with reversed phases, or Holland et al. algorithm [Holland 2010] which performs an intensity-based registration (each line being considered independently). As for Voss et al. algorithm, the obtained displacement field is sensitive to noise, especially when large displacements are present. More recently a new method has been proposed to combine EPI with opposite PED with PSF [In 2015] however costing additional acquisition time. Finally a registration-based method has been proposed by Irfanoglu et al. [Irfanoglu 2015] requiring a non distorted image such as a T2 image (in addition to the reversed PED image) which is used as the central point where the two images with reversed PEDs are transformed. It minimizes a cost function to compute a transformation which has no *a priori* restriction with respect to EPI image formation. The transformation is instead projected after each step of the minimization to follow a distortion model (with distortions appearing uniquely along the PED).

This last category of techniques has the advantage of requiring only a short additional acquisition time to correct for distortion: if we assume no patient movement occurred during the acquisition and that the magnetic field inhomogeneity stays constant during the acquisition [Vovk 2007], only one supplemental EPI image with reversed PED is necessary to correct the entire EPI series (e.g. fMRI or DWI acquisition). This chapter therefore presents a new algorithm for distortion correction falling in the same category. Block-matching (BM) based registration has been successfully proposed for registration in medical imaging both for rigid [Ourselin 2000] and non-linear registration [Commowick 2012a]. As a registration framework, BM has the advantage of being very generic and easily adaptable to different transformation priors, both to match blocks in the floating image [Commowick 2012b] and for the global transformation (linear or non-linear). Moreover, it is also robust to outliers in the local matches. Our approach towards distortion correction of EPI is thus based on BM. It is designed to register two images acquired with opposite PED without requiring an additional structural image. To do so, we introduce a symmetric BM registration algorithm, optimizing local affine transformations constrained *a priori* in the PED to match the expected distortions in EPI. In addition, the transformation is computed as opposite symmetric to match the distortion model in EPI [Jezzard 1995]. The implementation of our algorithm is available in our open source medical image processing toolbox Anima[2].

We evaluate this algorithm qualitatively and quantitatively on two datasets in Section 4.4. First, we present results on EPI acquisitions of a phantom, where the geometry of the image is known. We also perform evaluation on *in vivo* diffusion-weighted EPI of five subjects for which images with four different PED (anterior-posterior (AP), posterior-anterior (PA), left-right (LR), right-left (RL)) were ac-

[2] https://github.com/Inria-Visages/Anima-Public

quired. We present our results in contrast to two state-of-the-art methods using the same inputs: TOPUP from Andersson et al. [Andersson 2003] and Voss et al. method [Voss 2006].

4.2 Methods

4.2.1 Distortion Model

We assume that two images have been acquired: I_F is the EPI forward image acquired with a classical PED (AP for example), and I_B is the EPI backward image acquired with a reversed PED (PA in this case). The goal of EPI distortion correction is to estimate a distortion transformation field from these two images. Then, from this field, it is possible to recover a corrected image C from these two images, but also an entire serie of EPI acquired with AP or PA PED. Jezzard et al. [Jezzard 1995] have demonstrated that deformations due to B_0 field inhomogeneities appear mainly along the PED and are negligible in other directions. More precisely, we follow the distortion model as expressed previously in [Voss 2006, Morgan 2004] which assumes that I_F and I_B are generated from the theoretical corrected image C using a displacement field parallel to the PED:

$$\begin{cases} C(x) = & J_{T_+}(x) I_F\left(T_+(x)\right) \\ C(x) = & J_{T_-}(x) I_B\left(T_-(x)\right) \end{cases} \tag{4.1}$$

where $T_+(x) = x + U(x)$ and $T_-(x) = x - U(x)$. J_{T_+} and J_{T_-} denote the Jacobian determinants of the local deformations which account for intensity changes in the distorted areas. It will lead to an increased intensity in the contracted areas and a decreased intensity in the dilated areas. U corresponds to the distortion displacement field which is parallel to the PED, e.g. if the PED is along the y-axis then $U(x) = [0\ U_y(x)\ 0]^T$. It is assumed in this model that T_+ and T_- are opposite symmetric, i.e. that they share the same U up to a minus sign along the PED.

4.2.2 Block-matching for distortion correction

Different approaches may be considered to match the two images. In the distortion model, the corrected image C is generally unknown. It could be replaced (as suggested in [Irfanoglu 2015]) by a non distorted similar acquisition (such as a T2 weighted acquisition). However, this is not always available in clinical acquisitions. We therefore consider the case where C can be at best estimated and choose a registration approach that does not rely on it. A registration method has been introduced by Avants et al. [Avants 2008] allowing to estimate the corrected image C without having it directly appear in the algorithm. The idea, instead of looking for the transformation T between two images, is to seek the half-transformation $T^{1/2}$ so that the two images registered from I_F and I_B match as much as possible:

$$I_F \circ T^{1/2} \approx I_B \circ T^{-1/2} \approx C \tag{4.2}$$

We adapt this approach to a BM algorithm [Ourselin 2000, Commowick 2012a] by constraining the transformation to be aligned with the PED as assumed in the distortion model. The BM algorithm enables a simple and effective incorporation of this constraint on the deformation field. First we present the global scheme of the BM algorithm, then we detail each part separately. We consider an initial transformation U_0 which can be null or coming from another coarse correction algorithm. We use a classic multi-resolution pyramidal scheme [Burt 1983] to process images from coarse to fine resolution. At each level of the pyramid, from the transformation at the previous pyramid level, we proceed as described in Algorithm 1 and illustrated as a diagram in Fig. 4.1.

Algorithm 1 Block-matching algorithm for EPI distortion correction

1: **for** $p = 1...P$, iteration on pyramid levels, **do**
2: **for** $l = 1...L$, iterations, **do**
3: Resample images to get $I_{F,l-1}$ and $I_{B,l-1}$
4: Estimate local transformations for each block on $I_{B,l-1}$: $A_+ \leftarrow$ block-matching$(I_{B,l-1}, I_{F,l-1})$
5: Estimate local transformations for each block on $I_{F,l-1}$: $A_- \leftarrow$ block-matching$(I_{F,l-1}, I_{B,l-1})$
6: Extrapolate asymmetric dense SVF updates from A_+ and A_-:
$\delta S_+ \leftarrow$ extrapolate(A_+),
$\delta S_- \leftarrow$ extrapolate(A_-)
7: Compute a symmetric SVF update: δS, and compose it with current transformations
8: Ensure $T_{+,l}$ and $T_{-,l}$ are opposite symmetric
9: Regularize (elastic-like) $T_{+,l}$ and $T_{-,l}$

At each step, we first resample the original images with the current transformation. Then we estimate pairings between the images in the forward and backward directions ($A_+ = \{\hat{A}_{+,1}, .., \hat{A}_{+,N}\}$ and $A_- = \{\hat{A}_{-,1}, .., \hat{A}_{-,N}\}$) using a BM algorithm. We utilize A_+ and A_- to extrapolate two asymmetric stationary velocity field (SVF) δS_+ and δS_- which are combined into a symmetric SVF update δS (Section 4.2.3). We then compose this update with $T_{+,l-1}$ and $T_{-,l-1}$, and ensure that T_+ and T_- still share the same displacement field U. Finally, the current displacement field is regularized using a convolution with a Gaussian kernel (standard deviation σ_E). The following sections detail the BM, extrapolation and composition steps of this algorithm and their specificities for distortion correction of EPI.

4.2.2.1 Block-matching of distorted EPI

At each iteration, we define blocks $B_{+,i}$, which are patches centered at x_i with size $(2N+1)^3$, regularly placed on image $I_{B,l-1}$ (every V voxels in each direction). We also define blocks $B_{-,i}$ with the same characteristics on $I_{F,l-1}$. For each of those blocks, we look for an adapted transformation best matching them respectively to

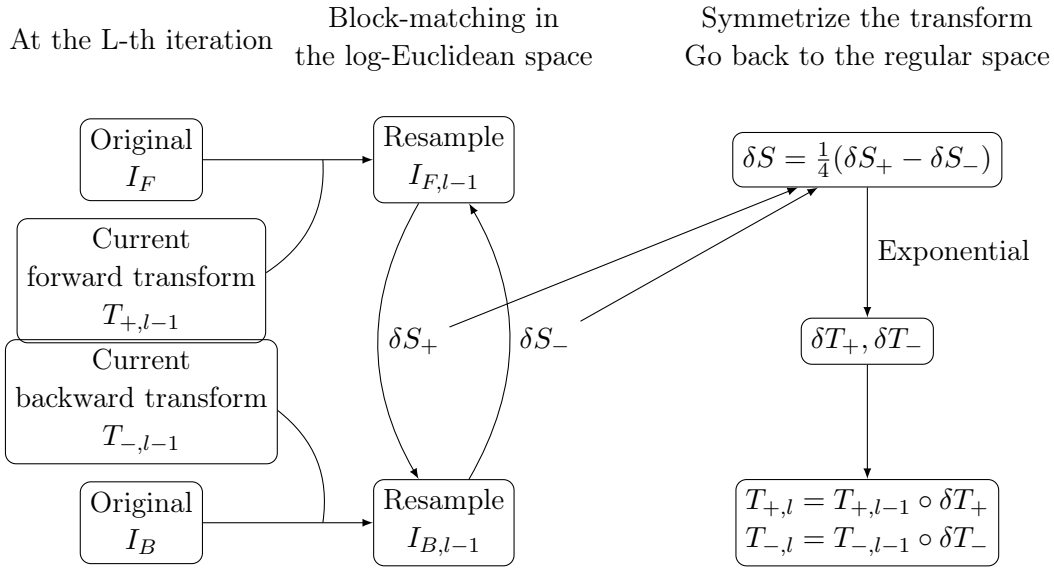

Figure 4.1: Graphical illustration of one iteration of the block-matching algorithm.

$I_{F,l-1}$ and $I_{B,l-1}$. Let $\mathcal{L}$ be the set of allowed transformations for matching blocks. Frequently, in other applications, the transformation sought between blocks is a simple 3-dimensional translation. In the case of EPI distortion, the set $\mathcal{L}$ can be further adapted to match *a priori* the expected features of the distortion at the block level and thus obtain a more robust transformation estimation. First the model assumes that distortions appear uniquely along the PED: a one-dimensional translation along the PED (modeled by one parameter $t_{.,i}$) is therefore sufficient. At the scale of the block, a single translation is however not enough to account for local contractions and dilations due to the distortion at different points of the block. We account for this by adding three parameters to the transformation. The first one accounts for the change of scale due to the global contraction or dilation inside the block ($s_{.,i}$). This scale parameter solves the problem of global scaling inside the block, however different lines along the PED will have different distortions generating skewness at the block level. To consider this, we define two skew components ($k_{.,i}$ and $m_{.,i}$) for the two directions complementary to the PED. Assuming the PED is the y-axis, $A_{.,i}$ is expressed as a 4×4 matrix:

$$A_{.,i} = \begin{pmatrix} 1 & 0 & 0 & 0 \\ k_{.,i} & s_{.,i} & m_{.,i} & t_{.,i} \\ 0 & 0 & 1 & 0 \\ 0 & 0 & 0 & 1 \end{pmatrix} \tag{4.3}$$

Note that having the PED on an other axis will result in the line of parameters being displaced on the first or third line of the matrix. A few interesting properties are associated to this transformation. The Jacobian determinant of the transformation is simply computed as the scaling parameter $s_{.,i}$, and this parameter is therefore

utilized directly for modeling the intensity changes due to distortion at the block level. To speed up the global SVF extrapolation process (see Section 4.2.3), the transformation is estimated directly in the log-space. As the log-Euclidean framework presented in Section 3.3.4 for the positive-definite matrix space, the equivalent for the affine transformation has been developed [Alexa 2002, Arsigny 2009]. Let's assume that the logarithm of the transformation A, is encoded, with simplified notation, as follow:

$$\tilde{A} = \begin{pmatrix} 0 & 0 & 0 & 0 \\ \tilde{k} & \tilde{s} & \tilde{m} & \tilde{t} \\ 0 & 0 & 0 & 0 \\ 0 & 0 & 0 & 0 \end{pmatrix} \tag{4.4}$$

where $\tilde{A}$ is the corresponding log-transformation and $\tilde{k}, \tilde{s}, \tilde{m}, \tilde{t}$ their corresponding parameters, this expression is equivalent as long as the scaling factor $s > 0$. The exponential of this matrix is defined as:

$$e^{\tilde{A}} = \sum_{k=0}^{\infty} \frac{\tilde{A}^k}{k!} = \left(\sum_{k=1}^{\infty} \frac{\tilde{s}^k}{k!} \right) \begin{pmatrix} 0 & 0 & 0 & 0 \\ \frac{\tilde{k}}{\tilde{s}} & 1 & \frac{\tilde{m}}{\tilde{s}} & \frac{\tilde{t}}{\tilde{s}} \\ 0 & 0 & 0 & 0 \\ 0 & 0 & 0 & 0 \end{pmatrix}$$

for any $s \neq 0$, which lead to the analytic expression:

$$e^{\tilde{A}} = I_4 + \begin{pmatrix} 1 & 0 & 0 & 0 \\ \frac{\tilde{k}}{\tilde{s}}(e^{\tilde{s}} - 1) & e^{\tilde{s}} & \frac{\tilde{m}}{\tilde{s}}(e^{\tilde{s}} - 1) & \frac{\tilde{t}}{\tilde{s}}(e^{\tilde{s}} - 1) \\ 0 & 0 & 1 & 0 \\ 0 & 0 & 0 & 1 \end{pmatrix} \tag{4.5}$$

where I_4 is the identity matrix. In the case $s = 0$, the exponential is smiplified to:

$$e^{\tilde{A}} = \begin{pmatrix} 1 & 0 & 0 & 0 \\ \tilde{k} & 1 & \tilde{m} & \tilde{t} \\ 0 & 0 & 1 & 0 \\ 0 & 0 & 0 & 1 \end{pmatrix} \tag{4.6}$$

From these expressions, the logarithm of A the original transformation which is the opposite of the exponential is recovered as:

$$\log(A) = \begin{pmatrix} 0 & 0 & 0 & 0 \\ \frac{k}{s-1}\log(s) & \log(s) & \frac{m}{s-1}\log(s) & \frac{t}{s-1}\log(s) \\ 0 & 0 & 0 & 0 \\ 0 & 0 & 0 & 0 \end{pmatrix} \tag{4.7}$$

which is correct as long as $s > 0$ and $s \neq 0$. If $s = 0$, the logarithm is simplified to:

$$\log(A) = \begin{pmatrix} 0 & 0 & 0 & 0 \\ k & 0 & m & t \\ 0 & 0 & 0 & 0 \\ 0 & 0 & 0 & 0 \end{pmatrix} \tag{4.8}$$

We have a corresponding one to one mapping between the affine transformation and the log-space. Therefore to speed up the algorithm, the BM search, as the entire pipeline, except the similarity measure, is done in the log-space. The BM step then amounts to estimate the four log-parameters of each block transformation in $\mathcal{L}$ to compute the set of optimal transformations $\hat{A}_{+,i}$ and $\hat{A}_{-,i}$ (respectively for blocks $B_{+,i}$ and $B_{-,i}$) optimizing a similarity measure S between $I_{F,l-1}$ and $I_{B,l-1}$:

$$\hat{A}_{+,i} = \arg\max_{\tilde{A}_{+,i}} S\left(J_{\exp(\tilde{A}_{+,i})} I_{F,l-1} \circ \exp(\tilde{A}_{+,i}), I_{B,l-1}\right) \tag{4.9}$$

$$\hat{A}_{-,i} = \arg\max_{\tilde{A}_{-,i}} S\left(I_{F,l-1}, J_{\exp(\tilde{A}_{-,i})} I_{B,l-1} \circ \exp(\tilde{A}_{-,i})\right) \tag{4.10}$$

This optimization is performed using the BOBYQA algorithm for gradient free optimization with parameters within predefined bounds [Powell 2009]. It proceeds by successively computing quadratic approximations to the cost function to find its local maximum.

4.2.2.2 Confidence weights

We have computed for each block $B_{.,i}$ the local transformation $\hat{A}_{.,i}$ that optimizes the similarity measure S. We then assign to this transformation a weight $w_{.,i}$ to estimate the confidence in the block match. To do so, we use a combination of two different terms. The first one is the similarity itself $\hat{S}_{.,i}$ assuming it belongs to the range $[0, 1]$, 1 being the best result (if not, a function of $\hat{S}_{.,i}$ can be used). The second one, $w_d(B_{.,i})$ gives an index of the local structure of the reference block along the PED. If the block structure is parallel to the PED, all tested transformations $A_{.,i}$ for that block may get the same similarity score, thereby introducing uncertainty in the matches. Actually, the algorithm will always find a solution due to small variations of intensities or computing precision. However the quality of such solutions will be random. We therefore want to avoid as much as possible such random solutions which can propagate important errors. Only considering the optimal similarity is therefore not enough and we introduce the index w_d to give a low weight to these uncertain blocks and their corresponding local transformations. w_d is defined as a function of the structure tensor inside the reference block $B_{.,i}$:

$$w_d(B_{.,i}) = c_l\left(D_{B_{.,i}}\right) < \hat{v}_{D_{B_{.,i}}}, g > \tag{4.11}$$

- $D_{B_{.,i}}$ is the average structure tensor of block $B_{.,i}$

- $c_l(D_{B_{.,i}})$ is a linear coefficient which quantifies the anisotropy of the tensor [Westin 2002]
  - $c_l(D_{B_{.,i}}) = \dfrac{\lambda_1 - \lambda_2}{\lambda_1}$, with $\lambda_1 \geqslant \lambda_2 \geqslant \lambda_3$ the eigenvalues of $D_{B(.,i)}$
  - $c_l(D_{B_{.,i}})$ is close to 0 if $D_{B_{.,i}}$ has a planar or circular structure and close to 1 if it has a very anisotropic one
- $\hat{v}_{D_{B_{.,i}}}$ is the principal eigenvector of $D_{B_{.,i}}$
- g is the unit vector along the PED

w_d will be 0 if the structure tensor is perpendicular to the PED (image structure parallel to g) or planar/spherical ($c_l = 0$) giving a structure based confidence to the matches. Finally, the weight for the match of block $B_{.,i}$ is defined as the geometric mean of the similarity index and the structural index:

$$w_{.,i} = \sqrt{w_d\left(B_{.,i}\right)\hat{S}_{.,i}} \tag{4.12}$$

4.2.3 Transformation extrapolation and composition

From the BM algorithm, two sets of block pairings have been constituted: one for I_F, $\hat{A}_+ = (\hat{A}_{+,1}, \ldots, \hat{A}_{+,m})$, and one for I_B, $\hat{A}_- = (\hat{A}_{-,1}, \ldots, \hat{A}_{-,n})$. Each pairing is defined by the center of its corresponding block $B_{.,i}$, a transformation $\hat{A}_{.,i}$, and a weight $w_{.,i}$. We then extrapolate two update SVFs from the sparse weighted transformation logarithms: $\delta S_+ = \text{extrapolate}(\hat{A}_+)$ and $\delta S_- = \text{extrapolate}(\hat{A}_-)$. This extrapolation aims at computing a dense field of transformation logarithms $\hat{R}_{.,i}$ ($i = 1, ..., M$ representing each voxel) from the sparse $\hat{A}_{.,j}$. This is performed utilizing an M-smoothing algorithm in the log-Euclidean space on affine transformations [Arsigny 2009] as proposed in [Commowick 2012a]:

$$(\hat{R}_{.,1}, \ldots, \hat{R}_{.,M}) = \underset{R_{.,1},\ldots,R_{.,M}}{\arg\min} \sum_{i=1}^{M} \sum_{j \in \mathcal{N}_i} w_{B_{.,j}} \rho\left(||R_{.,i} - \log \hat{A}_{.,j}||^2\right) d\left(|x_i - x_j|^2\right) \tag{4.13}$$

where log denotes the matrix logarithm which is naturally obtained in our framework, x_j is the spatial position of pairing, $\mathcal{N}_i$ is the neighbourhood of x_i, ρ is a robust error norm to account for outliers in the set of sparse transformations $\hat{A}_.$ (here the Welsh function), d is a function of the Euclidean distance - here $d(b^2) = \exp(-b^2/2\theta^2)$ - giving more importance to spatially close reference pairings. This cost function is optimized through an iterative scheme, more detailed in [Commowick 2012a]. The obtained transformation logarithms $\hat{R}_{.,i}$ are then applied to their respective positions x_i to compute the SVFs δS_+ and δS_-: $\delta S_.(x_i) = \hat{R}_{.,i}x_i$. Extrapolating update SVFs using this M-smoothing algorithm, we incorporate an outlier rejection framework, mainly coming from the ρ function in Eq. (4.13), that removes from the resulting SVF erroneous block transformation logarithms due for

example to artifacts or other effects in $I_{F,l-1}$ and $I_{B,l-1}$. In addition, the extrapolated fields are SVFs and therefore encode diffeomorphic and invertible transformations.

A symmetric δS is then computed, following [Vercauteren 2008], as a quarter of the subtraction of asymmetric incremental updates δS_+ and δS_-:

$$\delta S = \frac{1}{4}(\delta S_+ - \delta S_-) \tag{4.14}$$

While the half difference of the two asymmetric incremental updates is sufficient to compute a symmetrized field, δS is computed as a quarter of the difference as we are seeking the transformation bringing the two input images towards an unknown middle image C. As such only the half symmetric SVF is needed.

The final step of each iteration then amounts to composing the updates with the current transformations and ensure that the resulting $T_{+,l}$ and $T_{-,l}$ transformations still share the same displacement field U at the l-th iteration U_l. To do so, δT_+ and δT_- are first obtained by exponentiating δS: $\delta T_+ = \exp(\delta S)$ and $\delta T_- = \exp(-\delta S)$ [Arsigny 2009], and composed with the current transformations: $T_{+,l} = T_{+,l-1} \circ \delta T_+$ and $T_{-,l} = T_{-,l-1} \circ \delta T_-$. As the composition and inverse operations do not ensure the opposite symmetry condition, we finally compute the shared displacement field U_l as $U_l(x) = \frac{1}{2}\left(T_{+,l}(x) - T_{-,l}(x)\right)$ such that $T_{+,l}(x) = x + U_l(x)$ and $T_{-,l}(x) = x - U_l(x)$.

4.3 Experimental design

4.3.1 Image acquisitions

Imaging was performed on a Siemens Verio 3T scanner. The approach was evaluated on *in-vitro* and *in vivo* data:

- ***In vitro***: A grid phantom with known geometry developed by the UNIRS group from the commissariat a l'energie atomique (CEA) Neurospin for the CATI Consortium for image acquisition and processing[3] was imaged : b_0 images (AP, PA, LR and RL) were acquired with a 12 channels coil, a 128×128×60 matrix size and a 2×2×2mm^3 voxel size.

- ***In vivo***: 5 healthy volunteers were imaged after approval from the local institutional review board. For each volunteer, two pairs of b_0 EPI images with opposite PEDs (AP/PA and LR/RL), 128×128×60 matrix size and 2×2×2mm^3 voxel size were acquired with a 32 channels head coil. The EPI images were acquired using the parallel imaging method GRAPPA with an acceleration factor of 2 (TE = $82ms$ and an echo space $0.69ms$). Regular clinical DWI were also acquired (30 gradient directions, $b = 1000s.mm^{-2}$) with identical geometry and AP PED.

[3] http://cati-neuroimaging.com

4.3.2 Experimental methods

4.3.2.1 Evaluation strategy

In order to estimate the quality of the distortion correction we follow the process illustrated in Fig. 4.2. We first estimate a corrected image $C_{AP/PA}$ from one pair of reversed b_0 EPI (AP/PA). Then, independently, we estimate a corrected image $C_{LR/RL}$ from the other pair of reversed b_0 EPI (LR/RL). Each pair of reversed EPI has a PED following the same orientation but with an opposite direction. However the two pairs have a PED following a different orientation. This means that distortions will affect different areas of the brain in a different way depending on the orientation of the PED. We thus consider the quality of the match between $C_{AP/PA}$ and $C_{LR/RL}$ as an index to estimate the general quality of the distortion correction (see Fig. 4.2). If the two pairs of images are perfectly corrected, they will match after correction. In the following, we compare three different distortion correction methods with different metrics.

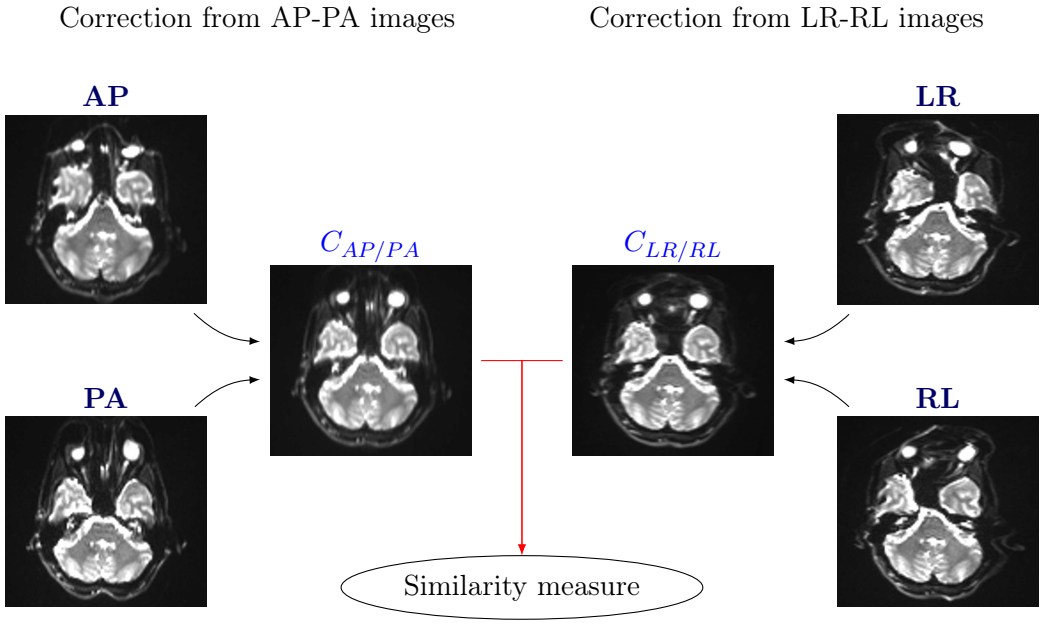

Figure 4.2: Illustration of the evaluation process for two pairs of EPI images with different reversed PEDs. On the left side, the AP (Top) and the PA (Bottom) images corrected by BM (Middle). On the right side, the LR (Top) and the RL (Bottom) images corrected by BM (Middle). A similarity measure between the 2 corrected images is performed to estimate the quality of the corrections.

4.3.2.2 Method 1: Voss

The first evaluated method was proposed by Voss et al [Voss 2006]. Their approach amounts, for each line in the PED, for both images, to do:

- Compute normalized cumulated intensities

$$N_i(y) = \frac{1}{\alpha_i} \int_0^y L_i(x)\mathrm{d}x \qquad \text{for } i = 1, 2 \tag{4.15}$$

- L_1 and L_2 are line intensities of images I_F and I_B, α_1 and α_2 are normalization constants:

$$\alpha_i = \int_0^\infty L_i(x)\mathrm{d}x \qquad \text{for } i = 1, 2 \tag{4.16}$$

- For a large number n of values x_n between 0 and 1, find by cubic interpolation [Schoenberg 1973] $y_{1,n}$ and $y_{2,n}$ such that $N_1(y_{1,n}) = N_2(y_{2,n}) = x_n$

- At each position $y_n = (y_{1,n} + y_{2,n})/2$, the transformation map is computed as

$$U(y_n) = y_{1,n} - y_n = y_n - y_{2,n} \tag{4.17}$$

This algorithm has the advantage of being very fast and simple. However, it is highly sensitive to noise and line registrations are purely independent which may lead to unrealistic transitions between consecutive lines. Therefore, a 3D Gaussian smoothing with a standard deviation σ is performed on the obtained transformation T, which leads to a trade-off between transformation precision (small Gaussian σ) and transformation regularity (large Gaussian σ). In our experimentations, we have set σ to one pixel.

4.3.2.3 Method 2: TOPUP

In addition to Voss et al. method, we also evaluated the distortion correction obtained from the TOPUP algorithm, available within the FSL package[4]. This correction method is based on the work from Andersson et al. [Andersson 2003]. It uses a model of EPI image formation and, together with the two images with opposite PEDs, reconstructs a deformation field to obtain a corrected EPI. More details are provided in Andersson et al. publication or on the FSL documentation page. We utilized the default parameters of this method for all of our experiments.

4.3.2.4 Method 3: Proposed block-matching technique

Distortion correction involves finding very large and local displacements between the images, displacements that may be extremely difficult to recover for registration approaches. We tackle this problem using a coarse-to-fine approach to recover EPI distortion and using Voss et al. method with a large σ smoothing value as an initial transformation, which is then further improved with our BM strategy.

Aside from transformation initialization, the BM implementation has different parameters, that are set as follows. First, we use three levels on the multi-resolution pyramid and 10 iterations at each level. The size of each block is 3×3×3 (i.e. $N = 1$).

[4] http://fsl.fmrib.ox.ac.uk/fsl/fslwiki/TOPUP

These blocks are placed regularly every two voxels in each direction ($V = 2$). The initial search radius for BOBYQA is set to 2 voxels, the initial skew radius is set to 0.1, and the initial scale radius to 0.1. We use a squared correlation coefficient as the similarity measure between blocks. At the end of each iteration, the elastic regularization is made with a σ_E value of 2 voxels. These parameters were set to the same values for each distortion correction experiment.

4.3.3 Evaluation Metrics

4.3.3.1 Phantom Evaluation: point-based metric

Contrary to brain images, the phantom acquisition has a known grid structure on which landmarks are easily identifiable. For each uncorrected image (AP, PA, LR and RL), 20 landmarks were carefully and manually selected at voxels representing crossing points. To evaluate quantitatively distortion correction, we have then applied the following steps for each evaluated method. First, images AP and PA, respectively LR and RL, were used to correct their distortion and estimate two deformation fields (one for AP/PA and one for LR/RL). For this specific evaluation, they were applied independently to the spatial landmark positions in AP, PA, LR and RL giving 4 corrected images. If the distortion correction is perfect, the transformed points should then match after transformation. We evaluate this match by computing an average of the one to one Euclidean distances between the landmarks:

$$d_i = \frac{1}{6} \sum_{j=1}^{4} \sum_{k>j}^{4} ||p_{i,j} - p_{i,k}|| \tag{4.18}$$

where $p_{i,j}$ denotes the transformed i-th landmark on image j (one of the four images with different PEDs, AP, PA, LR and RL). d_i is a distance in millimeters characterizing at which point the four images are distorted after correction around the specific locations of the $p_{i,j}$: the closer d_i is to 0, the closer the four input images are around the i-th landmark.

4.3.3.2 Brain images evaluation: intensity-based metrics

To compare images from the brain database after correction, we define a similarity measure computed between the two corrected images ($C_{AP/PA}$ and $C_{LR/RL}$).

This evaluation similarity measure (Sim) is defined as a sum of local correlation coefficients normalized between two images. To compute this metric only on relevant areas, masks are computed on four images, the two corrected by TOPUP and the two corrected by BM using the brain extraction tool of the FSL package[5]. Then the union of these four masks is used to obtain the global mask M and therefore compute the similarity measure:

[5] http://fsl.fmrib.ox.ac.uk/fsl/fslwiki/FSL

$$Sim(I, J, \mathcal{M}) = \frac{1}{\text{Card}(\mathcal{M})} \sum_{p \in \mathcal{M}} C(I_{\mathcal{N}_p}, J_{\mathcal{N}_p}) \tag{4.19}$$

where $I_{\mathcal{N}_p}$ and $J_{\mathcal{N}_p}$ are neighborhoods of p in I and J, defined as a cube centered on p of size $(2q+1)^3$, in the result part $q = 3$. C is the local correlation between $I_{\mathcal{N}_p}$ and $J_{\mathcal{N}_p}$. Card($\mathcal{M}$) denotes the cardinal of the set to ensure that Sim belongs to the range [0,1].

Sim characterizes well if the images match after correction and is defined between 0 and 1 which is useful to keep the same stable index between several subjects.

4.4 Results

4.4.1 Results on the Phantom

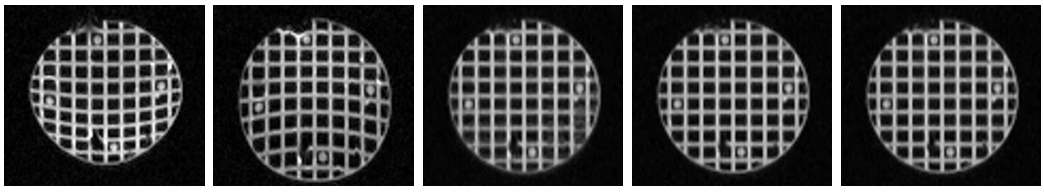

(a) AP (b) PA (c) Voss (d) TOPUP (e) BM

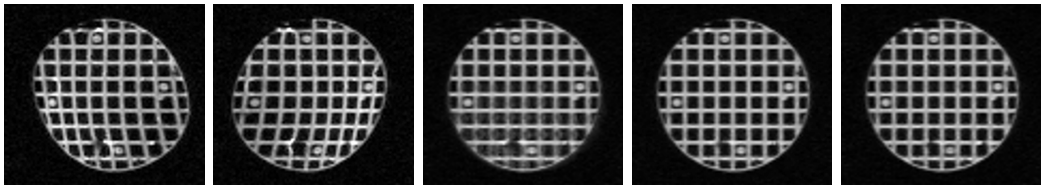

(f) LR (g) RL (h) Voss (i) TOPUP (j) BM

Figure 4.3: **Distortion correction results on a phantom**. Illustration of EPI distortion corrections with the evaluated methods on images acquired with opposite PEDs along the anterior-posterior axis (first line) and the left-right axis (second line). (a-b, f-g): uncorrected b_0 images, (c,h): correction with Voss et al. method, (d,i): correction with TOPUP, (e,j): correction with BM algorithm (proposed technique).

We first compare the different distortion correction algorithms on the phantom acquisition. We present in Fig. 4.3 a visual example of the phantom images before and after correction. The BM corrected images are really close and appear visually as being well corrected for distortion. TOPUP images are also properly corrected. Phantom images however do not represent a realistic anatomy and the distortion correction quality may vary depending on the methods. For example, Voss method is not adapted for this kind of bicolor images and gives visually poorer results.

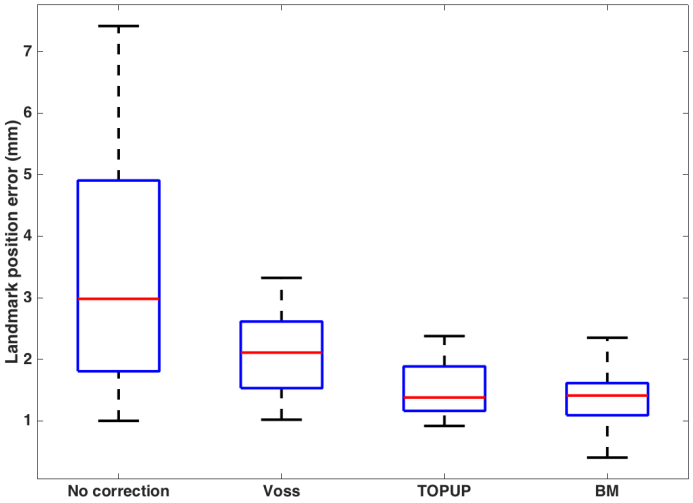

Figure 4.4: **Landmark position errors on the phantom.** Errors (in mm) box-plot before and after distortion correction with the Voss correction method, TOPUP and the proposed technique. Error differences are all significant (paired t-test see text for more details).

In addition to visual inspection, we computed landmark position errors based on the distance presented in Section 4.3.3.1, Eq. (4.18). These results are illustrated in Fig. 4.4, showing the box-plots of d_i distances over all i. Voss performs slightly and significantly better than uncorrected images (paired t-test, $p = 3 \times 10^{-3}$, average error of 2.09 mm compared to 3.46 mm untouched), illustrating its modest performance on this specific dataset. TOPUP also significantly reduces the distance errors, to an average of 1.54 mm, with respect to both uncorrected images (paired t-test, $p = 3 \times 10^{-4}$) and to Voss algorithm (paired t-test, $p = 1 \times 10^{-3}$). Finally, BM outperforms all other methods obtaining an average error of 1.38 mm, significantly different from uncorrected images (paired t-test, $p = 2 \times 10^{-4}$), Voss algorithm (paired t-test, $p = 4 \times 10^{-4}$) and TOPUP (paired t-test, $p = 0.028$), although both algorithms obtain close precision results, below the voxel size, and are therefore comparable. Overall, these results confirm the visual results, showing that both BM and TOPUP achieve the best results with BM having the lowest distance error and less variance.

4.4.2 Results on *in vivo* Data

4.4.2.1 Qualitative Results

We present in Fig. 4.5 results of our distortion correction method by visualizing pairs of b_0 EPI with opposite PED, corresponding images corrected by BM and structural T1 reference images. The two lines correspond to a different phase en-

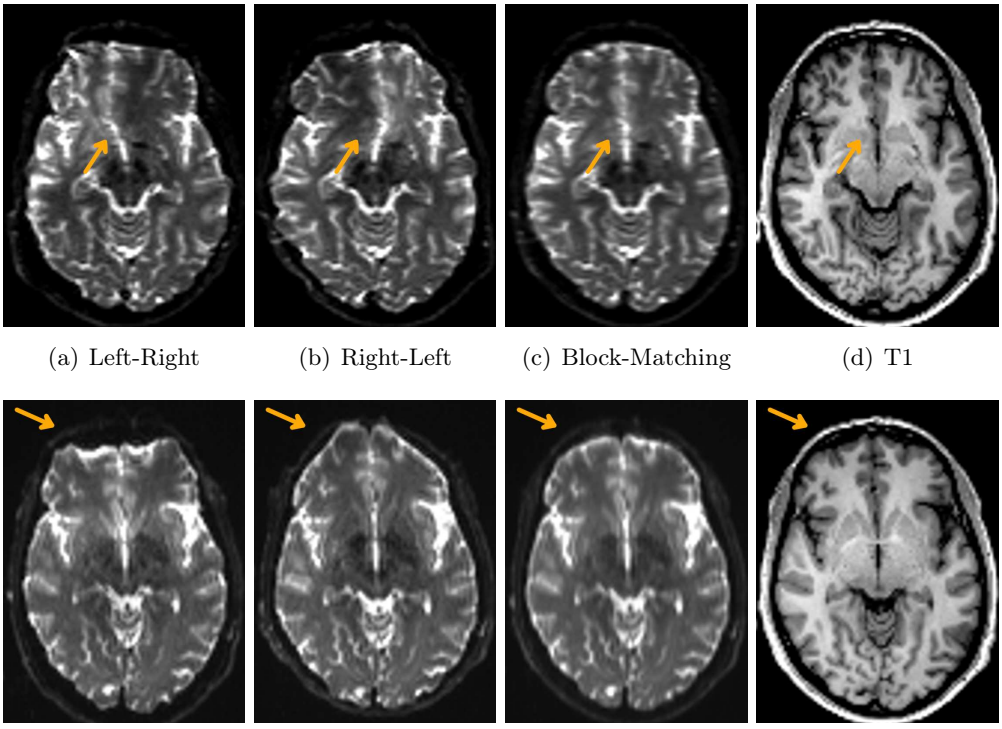

(a) Left-Right (b) Right-Left (c) Block-Matching (d) T1

(e) Anterior-Posterior (f) Posterior-Anterior (g) Block-Matching (h) T1

Figure 4.5: **Illustration of BM EPI distortion corrections on b_0 images acquired with opposite PEDs on one subject.** (a-b, d-e) pair of EPI with opposite PEDs along the left-right axis for the first row, along the anterior-posterior axis for the second row; (c,f) corresponding BM corrected images for each pair of EPI; (d,g) structural T1 reference.

coding orientation to show distortion in different orientations. It can clearly be seen on Fig. 4.5 that left-right and right-left PED images suffer from large spatial displacement around the falx cerebri (see arrows on Fig. 4.5.a,b). On the contrary, our distortion correction method allows for a good matching of the structures in the T1 image and on the b_0 corrected image (see arrows on Fig. 4.5.c,d). On the second line, anterior-posterior and posterior-anterior PED images suffer deformations, which include massive contractions and dilatations in addition to spatial displacements, around the frontal lobe (see arrow 4.5.e,f). Again the BM correction restores an image with a structure in phase with the T1 anatomical reference (see arrow 4.5.g,h).

Generally, in a clinical use, it is reasonable to acquire an entire DWI serie in one PED and a single b_0 with reversed PED. To correct b_0 EPI, a deformation field is estimated from the pair of reversed PED b_0. Then, considering no motion, this deformation field is used to correct the entire DWI serie. We present color fractional anisotropy (CFA), estimated from the original and the corrected DWI series, and their corresponding T1 (not distorted) images. The color in CFA map depends on

the principal direction of the tensor (red is Left/Right, green Anterior/Posterior and blue Foot/Head) and the intensity of the color is proportional to the FA value. The colors and intensities of original and corrected CFA are similar. However the position of the left-right corrected CFA offers a better matching with the structural T1 around the falx cerebri (see arrows 4.6.a,b,c) and for the anterior-posterior corrected CFA around the brainstem (see arrows 4.6.d,e,f). Such a good correction will then allow, for example, for a better definition of regions of interest from the T1 image to seed fiber tracts on the diffusion image, or to study diffusion model properties in specific anatomical regions.

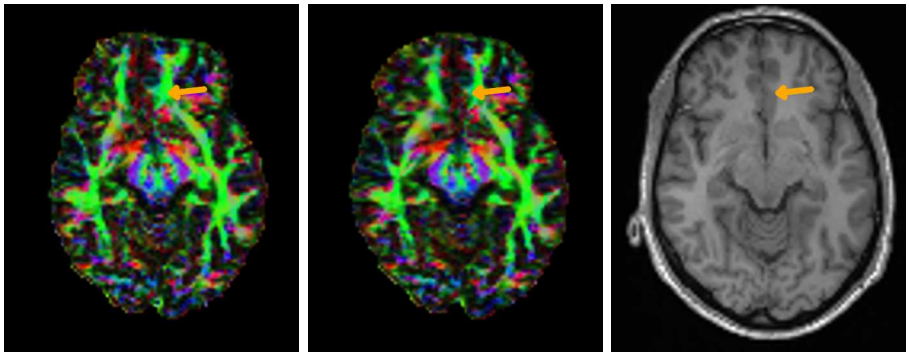

(a) left-right CFA (b) block-matching CFA (c) T1

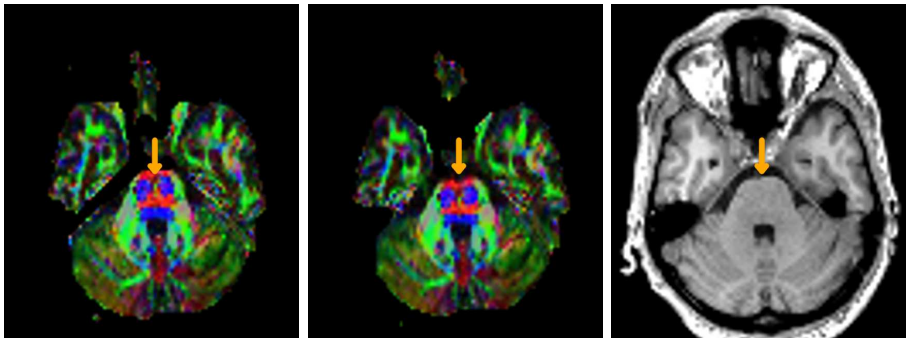

(d) anterior-posterior CFA (e) block-matching CFA (f) T1

Figure 4.6: **Colored FA visualization of distortion correction results.** The distortion field is computed from the two b_0 images and applied to an entire DWI volume with a left-right PED for the first line and a anterior-posterior PED for the second one. The FA is then estimated from the original and the corrected DWI. (a,d): uncorrected FA, (b,c): block-matching corrected FA, (c, f): structural T1 reference.

We then illustrate on Fig. 4.7 distortion correction results of the different evaluated methods on a pair of EPI with opposite PED (anterior-posterior and posterior-anterior). On this strongly affected area, we compared the three different distortion correction methods with respect to a structural image (T1 image). We first noticed that the three corrected images are more similar to the structural image than the

original ones, suggesting that each method is able to strongly reduce the distortions. However the image corrected using Voss et al. method (Fig 4.7.d) still presents a mismatch around the lateral ventricles (see arrow on Fig 4.7.b). TOPUP and BM both obtain a corrected image very close to the structural T1 image.

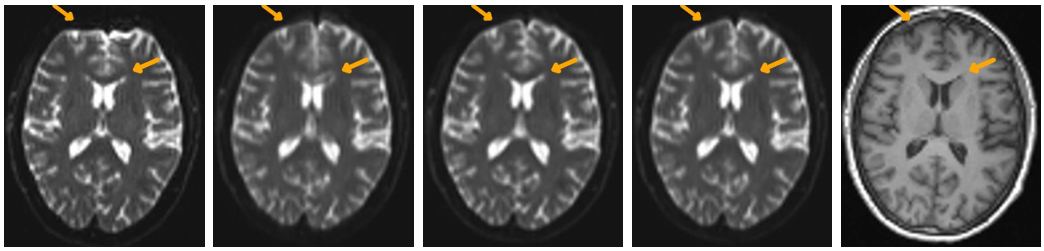

(a) AP b_0 (b) Voss b_0 (c) TOPUP b_0 (d) BM b_0 (e) T1

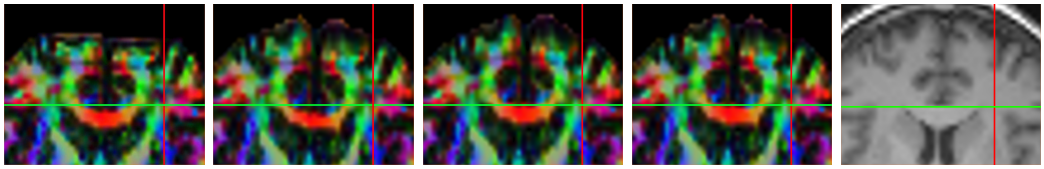

(f) AP CFA (g) Voss CFA (h) TOPUP CFA (i) BM CFA (j) T1

Figure 4.7: **Registration results on a subject according different distortion correction methods**. First row : (a) b_0 acquired with anterior-posterior PED; Mean of opposed PEDs corrected images : (b) by Voss; (c) by TOPUP; (d) by BM; (e) T1 structural reference. Second row (f) to (i) : zoom on the lateral ventricles of the corresponding colored FA; (j) T1 zoomed.

4.4.2.2 Quantitative Results

We performed experiments on an Intel Xeon 2.5 Ghz computer on 20 cores. The mean time per subject is very short (about 5s) for the Voss algorithm, 170s for the BM and 500s for TOPUP. Unlike TOPUP, BM is multi-threaded, allowing a faster computation time which may be useful in the clinic.

To obtain a quantitative evaluation of the quality of the corrected images, the similarity metric (Sim) introduced in Section 4.3.3.2 was computed on the dataset of 5 subjects after correction by the different methods. The Sim metric results between the two corrected images $C_{AP/PA}$ and $C_{LR/RL}$ are presented in Table 4.1. These results are consistent with visual inspection and highlight that BM performs better than Voss et al. on all subjects, showing a significant improvement of the correction compared to the initialization (Wilcoxon signed-rank test, $p = 0.03$). Between BM and TOPUP, the best score depends on the subject, the average similarity for the 5 subjects is better for BM than TOPUP however it is not statistically significant (Wilcoxon signed-rank test, $p = 0.69$).

Sim	Untouched	Voss	BM	TOPUP
Subject 1	0.842	0.901	0.916	0.927
Subject 2	0.818	0.904	0.918	0.937
Subject 3	0.812	0.875	0.894	0.859
Subject 4	0.886	0.923	0.939	0.954
Subject 5	0.872	0.913	0.921	0.898
Mean	0.852	0.903	0.918	0.915

Table 4.1: Correlation results (*Sim* measure) between AP/PA and LR/RL images. Columns from left to right: no correction, Voss, BM and TOPUP.

4.5 Discussion and Conclusion

This chapter presented a new block-matching based algorithm for EPI distortion correction using an additional EPI with reversed PED. To this end, we have developed specific linear transformations constrained to fit *a priori* with the distortion model at the block level. This transformation definition, integrated into a symmetric BM algorithm, ensures a robust computation of an opposite symmetric transformation.

We have tested our distortion correction and two state-of-the-art methods on a phantom with a known ground truth shape. Our results perform significantly better than Voss et al. correction, which is not adapted for images with uniform intensity regions. Moreover BM performs significantly better than TOPUP algorithm but at a sub-voxel level (though one should not over interpret this difference). Then, we have evaluated the BM registration on 5 subjects with 2 pairs of b_0 EPI. A similarity measure based on local correlation between the 2 corrected images $C_{AP/PA}$ and $C_{LR/RL}$ show a significant improvement between the Voss initialization and the BM correction. TOPUP algorithm and BM obtain similar levels of similarity. These results demonstrate the ability of our BM approach to compute a robust EPI distortion correction. Our algorithm is implemented in a multi-threaded fashion using ITK allowing for faster computation time than TOPUP.

A common problem with reversed PED methods is motion since the *a priori* distortion model is not true any more in that case. The best way to avoid motion problems is to perform an acquisition with continuously alternating PEDs and to correct all pairs independently. For clinical use it is also possible to acquire only one PA and a series of AP and then correct the entire series from the deformation field estimated. This is more subject to the motion issue but also reduces the acquisition time, which is crucial.

The intensity of distortion in EPI is related to susceptibility-induced fields and eddy current-induced fields. The general trend to increase the scanner field strength increases distortions [Wang 2005]. Thus it is essential to have efficient tools to correct these distortions. With that goal, we proposed a new simple and robust method, computationally efficient, ready for a clinical use. We studied its application for diffusion MRI, however it can be used for other modalities based on EPI acquisitions

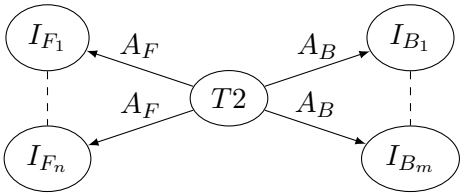

Figure 4.8: Illustration of multiple correlation BM with n b_0 forward images, m b_0 backward images and a non-distorted structural T2-weighted image in the middle.

such as fMRI.

4.6 Perspectives

4.6.1 Motivations

To increase the quality of the distortion correction, we want to extend the BM correction method adding an extra image as reference. Indeed for almost all protocols including EPI, at least one non-distorted structural image, as T1-weighted, T2-weighted, FLAIR, is acquired. Thus, there is a possibility to use this free extra-information to enhance the distortion correction. To do so, we developed a new BM algorithm with a structural image in the middle using a specific metric: the multiple correlation. To our knowledge, the concept of block-matching with more than 2 images has never been proposed before. We present this part in the perspective section as the results are not yet improving distortion correction and this subject requires more future research work.

4.6.2 New Block-Matching general framework

Now we consider that instead of a pair of b_0 with opposite PED, we have one set of n forward b_0 images, one set of m backward b_0 images for a total of $p = n + m$ EPI and one structural image as a T2-weighted image, see Fig 4.8. We want to use the non-distorted structural image to recover through correlation measures a transformation applicable to the DWI images. The underlying assumption made is that non-distorted b_0 images should have the same structure than a T2-weighted image. In the following, we present a metric, well adapted to our framework, named multiple correlation.

4.6.2.1 Multiple correlation

The multiple correlation is a metric taking one target variable y and several independent variables $\{x_i\}_{i=1,..,p}$. The multiple correlation coefficient is expressed as:

$$R = \sqrt{c^\top R_{x,x}^{-1} c} \tag{4.20}$$

where $c = (r_{y,x_1}, .., r_{y,x_p})^\top$ is a vector of correlation coefficients with r_{y,x_i} being the correlation between the target variable y and the independent variable x_i. $R_{x,x}$ is the covariance matrix of the independent variables:

$$R_{x,x} = \begin{pmatrix} r_{x_1,x_1} & \cdots & r_{x_1,x_n} \\ \vdots & \ddots & \vdots \\ r_{x_n,x_1} & \cdots & r_{x_n,x_n} \end{pmatrix} \tag{4.21}$$

where r_{x_i,x_j} is the correlation between x_i and x_j. The multiple correlation coefficient R belongs to the range $[0, 1]$ and denotes a correlation between y and a linear combination of x_i [Huberty 2003]. In the following, we describe how this measure is well adapted to our case and propose a algorithm for BM with several image.

4.6.2.2 Multiple correlation BM algorithm

Block-matching algorithm typically considers only two images to register. However, adding a structural image in the middle as a reference requires a new BM framework presented here. Now the structural image is represented by the target variable y and all the b_0 forward and backward registered images are represented by the independent variables x_i. Instead of classic BM, we look for the best parameters associated with both forward and backward log-transformations as:

$$A_F = \begin{pmatrix} 1 & 0 & 0 & 0 \\ k & s & m & t \\ 0 & 0 & 1 & 0 \\ 0 & 0 & 0 & 1 \end{pmatrix} \quad \text{and} \quad A_B = \begin{pmatrix} 1 & 0 & 0 & 0 \\ -k & -s & -m & -t \\ 0 & 0 & 1 & 0 \\ 0 & 0 & 0 & 1 \end{pmatrix} \tag{4.22}$$

where A_F is the forward log-transformation associated to the forward b_0 images and A_B is the backward log-transformation associated to the backward b_0 images (see Fig 4.8). For each block, the multiple correlation BM algorithm maximizes the multiple correlation between the target variable (the structural image) and the independent variables, forward and backward images registered by their respective transformations.

4.6.2.3 Results and discussions

We presented a mathematical framework of a new multiple correlation BM algorithm. In practice, the problem resides in getting of a non-distorted structural image enough similar to a b_0 EPI. In our experiments, we tried to use T2-weighted images. The forward b_0 images $\{x_i\}_{i=1,..,n}$ and the backward b_0 images $\{x_i\}_{i=n+1,..,p}$ are respectively averaged in one forward image x_F and one backward image x_B.

Fig 4.9 presents distortion correction results using, classic BM correction, multiple correlation BM correction, and the structural T2-weighted image used as target variable. The first line shows these results on an axial slice where the T2-weighted

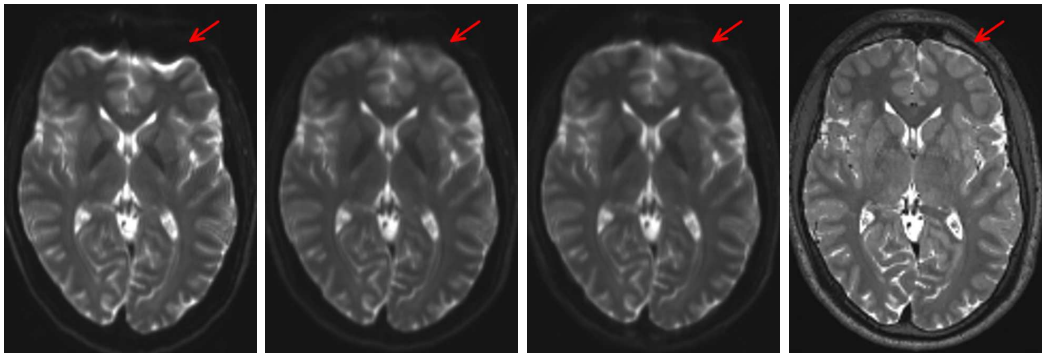

(a) Anterior-Posterior (b) Classic BM (c) Multiple correlation (d) T2-weighted

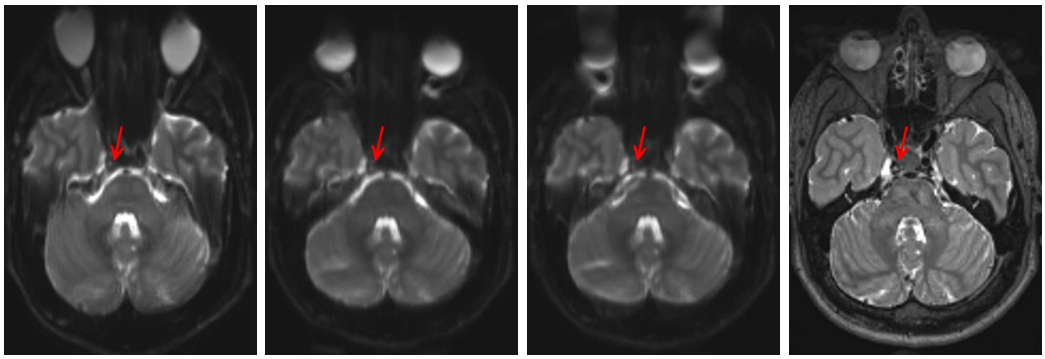

(e) Anterior-Posterior (f) Classic BM (g) Multiple correlation (h) T2-weighted

Figure 4.9: Illustration of the multiple correlation BM. From left to right: AP b_0 PED, classic BM from two b_0 (AP and PA), multiple correlation BM estimated from two b_0 as independent variables and one T2-weighted image as the target variable, the T2-weighted image. Line one: The multiple correlation BM offers a sharper reconstruction of the strongly distorted areas than the classical BM. Line two: The multiple correlation BM is not able to recover the eyes and more importantly presents issues around the brainstem.

image seem highly similar of how we expect a non distorted b_0 image. The remarkable result obtained on strong warped area by the multiple correlation shows the potential of this registration method. However, the second line shows results on a different slice where the T2-weighted images shows more details than the b_0 image does. The multiple correlation BM is not able to recover properly the eyes and also encounters issues around the brainstem whose boundaries get corrupted.

This new multiple correlation BM registration method presents promising results. Unfortunately for now, we are not able to obtain a good correction for the entire brain. The acquisition of a non-distorted image very similar to the b_0 should be a solution. A recent new sequence named readout-segmented EPI could provide such an image [Porter 2009].

Chapter 5

Interpolation of multi-compartment models

Contents

5.1 Introduction

Diffusion-weighted magnetic resonance imaging (DWI) is a unique MRI acquisition strategy, which can provide invaluable insights into the white matter architecture *in vivo* and non-invasively. A number of diffusion models have been devised, with the aim to characterize the underlying tissue microstructure. The most widespread model is known as diffusion tensor imaging (DTI) [Basser 1996] which, under the assumption of homogeneous diffusion in each voxel, describes the random motion of water as a single Gaussian process with a diffusion tensor. However, many regions of crossing fibers exist in low-resolution clinical DWI and the DTI model fails at correctly representing them. multi-compartment model (MCM) have been extensively proposed and studied as alternative diffusion models to cope with the intrinsic voxelwise diffusion heterogeneity [Ferizi 2014a]. The key principle of MCM is to explicitly model the diffusion in a number of pre-specified compartments akin to groups of cells inducing similar diffusion properties. MCMs may have a great impact on

patient diagnosis or care, as they allow for a better characterization of brain tissue microstructure, which enables the identification of more specific biomarkers such as proportion of free water (edema), proportion of water in axons (partial disruption or complete loss of axons, axonal injury), etc.

A critical step to identify relevant biomarkers on a large database is the creation of an atlas from individual estimated MCM images. This is achieved using registration and interpolation of MCMs. To date, only few approaches have addressed this issue. Among them, Barmpoutis et al. [Barmpoutis 2007] or Geng et al. [Geng 2009a] introduced registration methods specifically tuned for orientation distribution functions (ODF) on the sphere. Goh et al. [Goh 2011a] introduced an interpolation method for ODFs in a spherical harmonics basis as a Riemannian average. However, this approach does not apply to MCMs as they are not expressed in the same basis. Taquet et al. [Taquet 2012] proposed an interpolation approach seen as a simplification problem of all weighted compartments from a set of voxels into a smaller set of compartments. However, they assume that a single compartment belongs to the exponential family which is not the case for all MCMs.

We introduce in this chapter a new interpolation and averaging method for MCM images also seen as a simplification problem. It relies on the fuzzy spectral clustering [Ng 2002] of input compartments, from MCMs provided e.g. from trilinear interpolation, into a predefined number of output compartments. Then, each cluster is used to compute an interpolated compartment, providing an output MCM. This method is very generic as it relies only on the definition of a similarity measure between compartments and of a weighted averaging scheme for compartments. It can therefore be applied to any MCM as long as those two components may be defined.

The MCM interpolation / averaging simplification problem is presented in Section 5.2. We present in Section 5.4.2 the averaging schemes and distances for tensors, diffusion direction imaging (DDI) model and free water models. Then, we define 4 possible compartment averaging methods for the DDI model [Stamm 2012b] in Section 5.4.2 and similarity measures related to each of those averaging schemes. We demonstrate qualitatively and quantitatively the interest of both the averaging schemes and interpolation framework on simulated and *in vivo* data. We finally apply this framework to compute an atlas of DDI (Section 5.5) which clearly highlights a better averaging fiber crossing regions.

5.2 Model interpolation as a simplification problem

5.2.1 Global interpolation scheme

The interpolation and the atlas creation of MCM are two different problems which can be treated following almost the same framework. For the atlas creation, at a given voxel, we have m MCM, each coming from an individual image, each containing anisotropic compartments of constrained water diffusion and isotropic compartments describing unconstrained or restricted water diffusion. The natural average

of these m MCM is the superposition of the compartments with their corresponding weight multiply by the weights of their respective images $\alpha_1, ..., \alpha_m$. For the creation of an atlas, all the MCMs have the same weights which is the invert of the number of inputs:

$$\forall i = 1, .., m \quad \alpha_i = \frac{1}{m} \tag{5.1}$$

However, the high number of compartments composing that average MCM does not make it realistic according to the brain model and moreover causes algorithmic issues due to its important size. In this chapter, we describe how to simplify a MCM into a smaller one, i.e with less anisotropic and isotropic compartments.

For the interpolation scheme, we want to apply a transformation to a MCM. In the case of a trilinear interpolation, for each voxel in the interpolated MCM, we need to mix 8 neighboring voxels with weights α^i corresponding to the output voxel position. This problem is similar to the averaging of several MCM: the simplification of a large number of compartments into a smaller one. Here weights of the MCM α^i are defined by the spatial position of the trilinear interpolation.

We consider m MCM $M^i (i = 1, ..., m)$ each containing $c(i)$ compartments of anisotropic water diffusion and g compartments of isotropic water diffusion. This means that the input MCM do not necessarily have the same number of anisotropic compartments, however they are assumed to have the same number of isotropic compartment g (one free water and one restricted diffusion water for example). We note F^i_j the j-th anisotropic compartment of M^i and $F^i_{\text{iso, l}}$ its l-th isotropic compartments, their respective weights being w^i_j and $w^i_{\text{iso, l}}$ which sum up to 1. Each of these M^i has an associated weight α^i. We formulate the interpolation problem as merging the M^i into one MCM with a predetermined number of anisotropic compartments q and g isotropic compartments. There are therefore two different averaging parts: anisotropic compartments and isotropic compartments.

The averaging of all anisotropic compartments coming from M^i into q anisotropic compartments is performed using spectral clustering [Ng 2002]. Having defined a similarity matrix S between anisotropic compartments, spectral vectors are extracted from S. These spectral vectors are then clustered using fuzzy C-Means. Hence, we obtain q sets of n weights (n being the total number of anisotropic compartments) $\beta^i_{j,k}$ that are probabilities for the j-th anisotropic compartment of M^i to belong to the k-th cluster $k \in \{1, .., q\}$. We define $\theta^i_{j,k}$ the weight of the j-th anisotropic compartment of M^i in the k-th cluster and $\theta^i_{\text{iso},l}$ the weight of the l-th isotropic compartment of M^i:

$$\theta^i_{j,k} = \alpha^i w^i_j \beta^i_{j,k} \tag{5.2}$$

$$\theta^i_{\text{iso},l} = \alpha^i w^i_{\text{iso},l} \tag{5.3}$$

From $\theta^i_{j,k}$ and $\theta^i_{\text{iso},l}$, we compute weights ϕ_k and $\phi_{\text{iso},l}$ of the output compartments.

$$\forall k = 1, ..., q \quad \phi_k = \sum_{i=1}^{m} \sum_{j=1}^{c(i)} \theta_{j,k}^i \tag{5.4}$$

$$\forall l = 1, ..., g \quad \phi_{\text{iso},l} = \sum_{i=1}^{m} \theta_{\text{iso},l}^i \tag{5.5}$$

We also define $\hat{\theta}_{j,k}^i$ and $\hat{\theta}_{\text{iso},l}^i$ different sets of normalized weights from $\theta_{j,k}^i$ and $\theta_{\text{iso},l}^i$ as:

$$\forall k = 1, ..., q \quad \sum_{i=1}^{m} \sum_{j=1}^{c(i)} \hat{\theta}_{j,k}^i = 1 \tag{5.6}$$

$$\forall l = 1, ..., g \quad \sum_{i=1}^{m} \hat{\theta}_{\text{iso},l}^i = 1 \tag{5.7}$$

From these sets of weights, we are able to simplify the input MCM into a single one C containing q anisotropic compartments $\{C_k\}_{k=1,...,q}$ and g isotropic compartments $\{C_{\text{iso},l}\}_{l=1,...,g}$:

$$\forall k = 1, ..., q \quad C_k = \sum_{i=1}^{m} \sum_{j=1}^{c(i)} \theta_{j,k}^i F_j^i \tag{5.8}$$

$$\forall l = 1, ..., g \quad C_{\text{iso},l} = \sum_{i=1}^{g} \theta_{\text{iso},l}^i F_{\text{iso},l}^i \tag{5.9}$$

An illustration of this global interpolation scheme is presented in Fig 5.1. This framework is very generic and can be applied to any MCM as long as we provide a way to compute a similarity matrix between anisotropic compartments. The spectral clustering is described in Section 5.2.2. The isotropic compartment averaging is common to any MCM and is described in Section 5.3. We derive MCM compartments averaging and similarity measure for the multi-tensor in Section 5.4.1 and then for the DDI in Section 5.4.2.

5.2.2 Spectral clustering

Reducing a number of objects or variables into a smaller group (often denoted as clusters) is a common issue to many different domains: machine learning, data compression or image segmentation for example [Haralick 1985]. This is a difficult and open problem with a large litterature on it [Jain 1999]. Here we want to cluster n compartments into q comparments as in Fig 5.2.

Among the most popular algorithms proposed, the k-means consists in minimizing the distance across groups between points and their cluster centroids [Lloyd 1982]

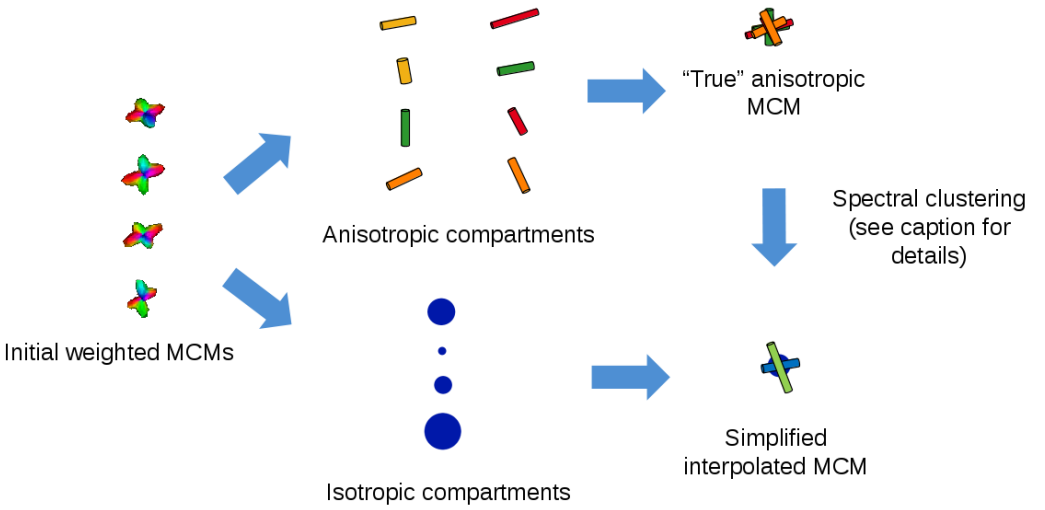

Figure 5.1: Global scheme of the interpolation of 4 MCMs with two anisotropic compartments and one isotropic compartment each. The detail of the spectral clustering is presented in Fig 5.1

[Likas 2003]. In this algorithm, each data point is affected to one and only one class. The algorithm thus alternates, from an initial position, between centroid computation and cluster affectation. The minimization of the distance in the k-means algorithm is a NP-hard problem [Mahajan 2009], for which a large number of approximations in a polynomial time have been proposed [Hartigan 1979, Kanungo 2002, Park 2009]. However these methods are sensitive to a random inizialization and the risk to converge to a local minimum is high [Bradley 1998]. Another clustering category considers a different way of affecting data points to classes by assiging a weight to each point which corresponds to a probability of membership to each cluster. The fuzzy C-means clustering belong to this category [Bezdek 1984, Pal 2005].

Here we use a normalized spectral clustering algorithm [Ng 2002], illustrated in Fig 5.2. From a similarity matrix S between inputs, spectral vectors of dimension q (where q is the number of clusters) are computed and used to initialize a clustering algorithm, generally the k-means, but we choose the fuzzy-C-means to keep continuity in the interpolation. Several choices are possible to define spectral vectors : we use the largest eigenvectors of the symmetric normalized Laplacian of S [Ng 2002]. This method only needs a similarity matrix between the inputs (here MCM compartments), is robust, well-reviewed with a large number of algorithms proposed [Von Luxburg 2007, Spielmat 1996]. For each type of compartments, we define specific semimetric $\{d(F_i, F_j)\}_{i,j=1,\dots,n}$ which are used to compute the similarity matrix. A semimetric d has the same properties than classic distance without the triangle inequality:

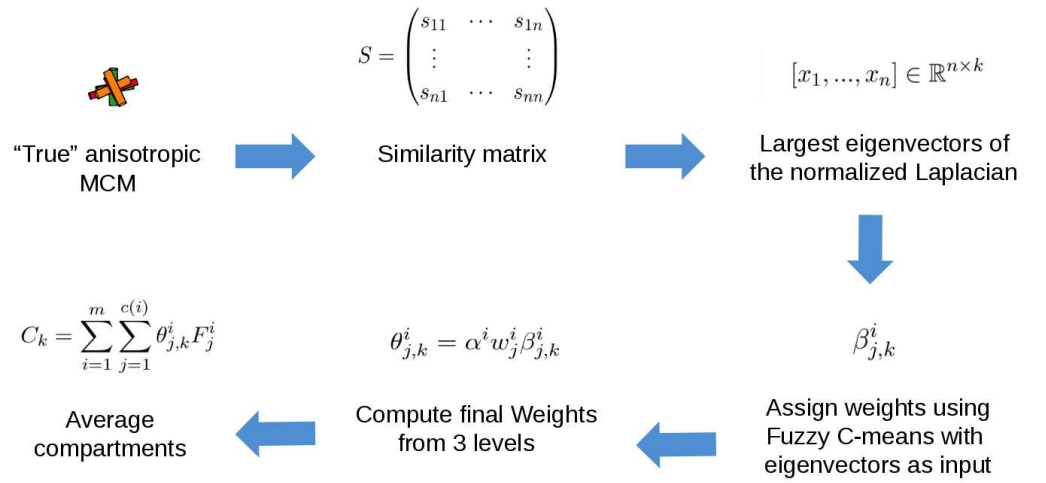

Figure 5.2: Illustration of spectral clustering using Fuzzy C-Means

$$\begin{cases} d(F_i, F_j) \geq 0 \\ d(F_i, F_j) = 0 \text{ if and only if } F_i = F_j \\ d(F_i, F_j) = d(F_j, F_i) \end{cases} \tag{5.10}$$

this allows to define a weak metric in spaces not equipped with a natural distance. From this semimetric, we compute the similarity matrix as:

$$S_{i,j} = \left\{ e^{\frac{-d^2(F_i, F_j)}{2\sigma^2}} \right\}_{i,j=1,...,n} \tag{5.11}$$

where σ is a normalization coefficient to avoid computational errors. We describe how distances $\{d(F_i, F_j)\}_{i,j=1,...,n}$ are defined for isotropic compartments in Section 5.3 for the multi-tensor and several DDI semimetrics in Section 5.4.

5.3 Isotropic compartments averaging

Isotropic compartments are treated differently from other compartments as they represent specific tissues with no preferred direction and known properties. Each MCM M^i has g isotropic diffusivities $d^i_{\text{iso},l}$ from its isotropic compartments $F^i_{\text{iso},l}$, associated to weights $\theta_{\text{iso},l}$. Isotropic diffusions follow a Gaussian distribution with covariance matrix $D^i_{\text{iso},l}$ defined as :

$$\forall l = 1, ..., g \quad D^i_{\text{iso},l} = d^i_{\text{iso},l} I_3 \tag{5.12}$$

where I_3 is the identity matrix. These covariance matrices $D^i_{\text{iso},l}$ define tensors and then belong to $\mathcal{S}^+_3(\mathbb{R})$, the space of positive-definite matrices and can be averaged following the log-Euclidean framework described in Section 3.3.4.6. Then the average isotropic tensors are defined as:

$$\forall l = 1, ..., g \quad D_{\text{iso},l} = \exp\left(\sum_{i=1}^{m} \hat{\theta}^i_{\text{iso},l} \log(D^i_{\text{iso},l})\right) \tag{5.13}$$

In this simple case, the exponential and the logarithm of identity matrices multiplied by a scalar are given by:

$$\exp(\alpha I_3) = \exp(\alpha) I_3 \tag{5.14}$$

$$\log(\alpha I_3) = \log(\alpha) I_3 \tag{5.15}$$

which simplify Eq (5.13) and lead to the mean diffusivities:

$$\forall l = 1, ..., g \quad d_{\text{iso},l} = \exp\left(\sum_{i=1}^{m} \hat{\theta}^i_{\text{iso},l} \log(d^i_{\text{iso},l})\right) \tag{5.16}$$

5.4 Anisotropic compartments averaging

Each MCM has one or several anisotropic compartments which represent a constrained water diffusion along particular tissues. Within an axon, the water is indeed trapped and then diffuses along the axon direction. A bundle of axons oriented in the same direction creates an unisotropic water diffusion at the voxel level. This water diffusion is represented as an anisotropic compartment following different models depending on the MCM considered. We present the interpolation scheme for two MCM: the multi-tensor model (MTM) in Section 5.4.1 and the diffusion direction imaging (DDI) in Section 5.4.2.

For each cluster k, we wish to average the set of F^i_j with weights $\hat{\theta}^i_{j,k}$ into a compartment C_k with weight ϕ_k. To simplify notations in the following section, we now just consider n anisotropic compartments with their corresponding weights w_i that we want to average into a single one. To perform spectral clustering, we also need to be able to compute a similarity measure between two anisotropic compartments. In each part of the following sub-section, we define the similarity measure induced by the semimetric used to average compartments.

5.4.1 Multi-tensor

The multi-tensor model (MTM) is one of the classical MCM (see Section 3.5.3.1). It contains several anisotropic tensors and one or several isotropic compartments. We want to average these anisotropic tensors and define a distance between them. Let $\{T_i\}_{i=1..n}$ be a set of tensors with their corresponding weights $\{w_i\}_{i=1..n}$. All $\{T_i\}_{i=1..n}$ belong to $\mathcal{S}^+_3(\mathbb{R})$, the space of positive-definite matrices and can be average following a log-Euclidean framework. The computation is done in the log-Euclidean space and the average tensor is recovered as:

$$T = \exp\left(\sum_{i=1}^{n} w_i \log(T_i)\right) \tag{5.17}$$

From this, we can easily and efficiently average any number of tensors into a unique one. A distance between two tensors is also directly defined in the log-Euclidean space as:

$$d(T_1, T_2) = ||\log(T_1) - \log(T_2)||_F \tag{5.18}$$

where $||.||$ is the Frobenius norm:

$$||M||_F = \sqrt{\mathrm{Tr}(M^T M)} = \sum_j \lambda_j^2 \tag{5.19}$$

where Tr is the trace operator and λ_j are the eigenvalues of M. The similarity matrix used for spectral clustering is thus derived from Eq 5.11. Examples of the multi-tensor averaging are given in the results part (Section 5.5). In the following, we continue to focus on the compartments averaging on an other MCM: the DDI. We introduce the DDI model and then compare several metrics to average the DDI anisotropic compartments.

5.4.2 DDI model

5.4.2.1 Presentation of the DDI model

In addition to one or several isotropic water compartments, a number of axonal compartments are added to the DDI to model how water molecules diffuse in axonal bundles with various orientations. Diffusing water molecules in a particular axonal compartment are assumed to undergo a random displacement that is the independent sum of a von Mises & Fisher (VMF) vector on the sphere S^2 of radius r and a Gaussian vector on $\mathbb{R}^3$ [Stamm 2012c]. The VMF is an orientation distribution with the following PDF on the unit sphere [Banerjee 2005]:

$$f(x|\mu, \kappa) = \frac{\kappa}{2\pi(e^{\kappa} - e^{-\kappa})} e^{\kappa \mu^T x} \tag{5.20}$$

where $x \in S^2$, $\mu \in S^2$ is the principal axis of diffusion, $\kappa \in [0, \infty[$ is an index of the concentration of diffusion around μ ($\kappa = 0$ is an isotropic distribution and $\kappa \to \infty$ is a distribution focused on one point, see Fig 5.3). This definition of a VMF distribution is extended to a sphere of radius r :

$$f(x|\mu, \kappa, r) = \frac{\kappa}{2\pi r^{\frac{3}{2}}(e^{\kappa} - e^{-\kappa})} e^{\frac{\kappa \mu^\top x}{r}} \tag{5.21}$$

Hence, the resulting PDF describing this random displacement is given by the 3D convolution of the VMF distribution with the Gaussian distribution:

$$p_0(x|\mu, \kappa, d, \nu) = f(x|\mu, \kappa, r) * \frac{e^{-\frac{1}{2} x^T \Sigma^{-1} x}}{(2\pi)^{\frac{3}{2}} |\Sigma|^{\frac{1}{2}}} \tag{5.22}$$

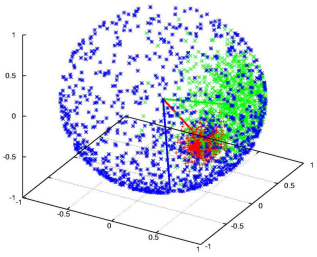

Figure 5.3: *From Wikimedia Commons* : Points sampled from three von Mises-Fisher distributions on the sphere (blue: $\kappa = 1$, green: $\kappa = 10$, red: $\kappa = 100$). The mean directions μ are shown with arrows.

where r is the radius of the VMF sphere given by $r = \sqrt{\nu d}$ and Σ the covariance matrix of the Gaussian part defined as:

$$\Sigma = \frac{(1-\nu)d}{\kappa+1}[I_3 + \kappa\mu\mu^T] \tag{5.23}$$

where d is the diffusivity along μ and ν the non Gaussianity proportion of the compartment. The VMF distribution present a favorite direction along μ. However an anisotropic compartment represents a bundle of axons which is assumed to be in a unique orientation with no privileged forward or backward direction within a voxel. Therefore the water diffusion is equal in both direction $\pm\mu$, thus to consider orientation instead of direction, the PDF is symmetrized:

$$p(x|\mu,\kappa,d,\nu) = \frac{p(x|\mu,\kappa,d,\nu) + p(x|-\mu,\kappa,d,\nu)}{2} \tag{5.24}$$

We now consider n compartments $F_i (i = 1, ..., n)$ with their corresponding weights w_i that we want to average into one compartment F. From this model, let $\mu_i, \kappa_i, \nu_i, d_i$ be the parameters of all the compartments F_i and μ, κ, ν, d be the parameters of the final average compartment F. We propose four different methods to compute this average: simplest, tensor, log VMF, and covariance analytic.

5.4.2.2 Simplest averaging

In the DDI model, each μ_i is a unit direction in S^2. However, as we saw previously, they do not represent a direction but an orientation. The simplest way to solve this problem (as two opposite directions) is to put all μ_i in the top hemisphere and average them on the sphere to obtain μ :

$$\begin{cases} \rho = \sum_{i=1}^{n} w_i \rho_i \\ \varphi = \sum_{i=1}^{n} w_i \varphi_i \end{cases} \tag{5.25}$$

where $\rho_i \in [0, \pi]$ and $\varphi_i \in [0, \pi]$ represent the spherical coordinates of the μ_i put in the top half sphere, ρ and φ the average angles of μ. The rest of the parameters are simply estimated as a weighted Euclidean averaging :

$$\begin{cases} \kappa = \sum_{i=1}^{n} w_i \kappa_i \\ d = \sum_{i=1}^{n} w_i d_i \\ \nu = \sum_{i=1}^{n} w_i \nu_i \end{cases} \tag{5.26}$$

In this average, all parameters are estimated independently and we wish to compute a similarity measure to this semimetric. A weighted sum of distances using all parameters is used and defined as:

$$d_{\text{simple}}(F_1, F_2) = | < \mu_1, \mu_2 > | + \alpha|\kappa_1 - \kappa_2| + \beta|d_1 - d_2| + \gamma|\nu_1 - \nu_2| \tag{5.27}$$

with α, β, γ normalization terms to give each parameters the same influence in the similarity between compartments. The similarity matrix S used for spatial clustering related to this average is then defined using the semimetric defined in Eq 5.27 along Eq 5.11.

5.4.2.3 Tensor averaging

The simple averaging is only a partial solution, especially for directions close to the sphere equator which might generate discontinuities in averaging. We now consider μ_i as orientations instead of directions. To do so, μ_i is represented as a cigar-shaped tensor T_i defined as:

$$T_i = \mu_i \mu_i^T + \varepsilon I_3 \tag{5.28}$$

with $\varepsilon = 10^{-6}$ to have non degenerated tensors and I_3 the identity matrix. Then, $T_i \in \mathcal{S}_3^+(\mathbb{R})$ and we can use the log-Euclidean framework. The T_i are averaged in the log space in a similar way to MTM:

$$T = \exp\left(\sum_{i=1}^{n} w_i \log(T_i)\right) \tag{5.29}$$

We define the average μ as the principal direction of T (i.e the eigenvector with the largest eigenvalue). The other parameters are obtained by weighted Euclidean averaging as for the simple averaging. Also the semimetric between compartments is defined as:

$$d_{\text{tensor}}(F_1, F_2) = ||\log(T_1) - \log(T_2)||_F + \alpha|\kappa_1 - \kappa_2| + \beta|d_1 - d_2| + \gamma|\nu_1 - \nu_2| \tag{5.30}$$

where α, β and γ are normalization coefficients. This semimetric is then used along Eq 5.11 to compute the similarity matrix.

5.4.2.4 Covariance analytic

Another approach uses information from covariance matrices Σ_i of the DDI compartments. These Σ_i matrices belong to $S_3^+(\mathbb{R})$ and can be averaged into Σ using the log-Euclidean framework similarly to Eq. (5.29):.

$$\Sigma = \exp\left(\sum_{i=1}^{n} w_i \log(\Sigma_i)\right) \tag{5.31}$$

We then wish to extract all parameters from the average Σ. We start by approximating Σ by a cigar-shaped tensor to match the DDI compartment model. To do this, we need to enforce two equal secondary eigenvalues $\lambda_\perp$. In the log-Euclidean framework, this amounts to compute $\lambda_\perp$ as $\lambda_\perp = \sqrt{\lambda_2 \lambda_3}$ where λ_2, λ_3 are the two lowest eigenvalues of Σ. We now have $\hat{\Sigma}$ the cigar-shaped tensor of F:

$$\hat{\Sigma} = \frac{(1-\nu)d}{\kappa+1}[I_3 + \kappa\mu\mu^T] \tag{5.32}$$

A tensor in $S_3^+(\mathbb{R})$ with 3 different eigenvalues has 6 specific parameters, however our tensor is cigar-shaped and then only has 4 specific parameters. We want to recover 2 parameters for the direction μ and 1 for κ, μ and d. For the missing 5-th parameter, we process by identification using the given relation $r^2 = \nu d$. To exploit this relation, we define the average radius as the one whose sphere surface is the average of the input sphere surfaces. This corresponds to a weighted Euclidean average of the individual r_i^2:

$$r = \left(\sum_{i=1}^{n} w_i r_i^2\right)^{\frac{1}{2}} \tag{5.33}$$

This therefore gives us a direct relation between ν and d leading to only 4 parameters to estimate (μ, κ and ν), d being computed as $d = r^2/\nu$. Then, we can estimate all the parameters by the resolution of the eigensystem of $\hat{\Sigma}$. Interestingly, we can develop the product $\hat{\Sigma}\mu$ as follows:

$$\hat{\Sigma}\mu = \frac{(1-\nu)d}{\kappa+1}[I_3 + \kappa\mu\mu^\top]\mu \tag{5.34}$$

Additionally, μ belong to S^2 and thus $\mu^\top\mu = 1$. We thus obtain:

$$\hat{\Sigma}\mu = \frac{(1-\nu)d}{\kappa+1}(1+\kappa)\mu \tag{5.35}$$

$$\hat{\Sigma}\mu = (1-\nu)d\mu \tag{5.36}$$

We can therefore see that μ is an eigenvector of $\hat{\Sigma}$ and $\lambda = (1-\nu)d$ is its corresponding eigenvalue. We note $\mu_\perp$ any perpendicular vector to μ and compute $\hat{\Sigma}$:

$$\hat{\Sigma}\mu_\perp = \frac{(1-\nu)d}{\kappa+1}[I_3 + \kappa\mu\mu^\top]\mu_\perp \tag{5.37}$$

the dot product $\mu^\top \mu_\perp$ being null, then:

$$\hat{\Sigma}\mu_\perp = \frac{(1-\nu)d}{1+\kappa}\mu_\perp \tag{5.38}$$

any $\mu_\perp \in \text{Vect}(\mu)^\perp$ is an eigenvector of $\hat{\Sigma}$ forming a two-dimension eigenspace with an unique eigenvalue associated $\lambda_\perp = \frac{(1-\nu)d}{1+\kappa}$. We can notice that $\lambda > \lambda_\perp$ is the largest eigenvalue because $\kappa > 0$, then μ corresponds to the principal direction of $\hat{Sigma}$ that can be computed from the numerical resolution of the eigensystem. We have $\lambda = (1-\nu)d$, $\lambda_\perp = \frac{(1-\nu)d}{1+\kappa}$ and $d = \frac{r^2}{\nu}$. Resolving the system, we obtain these estimations for κ and ν:

$$\begin{cases} \lambda = \frac{(1-\nu)r^2}{\nu} & \longrightarrow \quad \nu = \frac{r^2}{\lambda + r^2} \\ \lambda_\perp = \frac{(1-\nu)r^2}{(1+\kappa)\nu} & \longrightarrow \quad \kappa = \frac{\lambda}{\lambda - \lambda_\perp} \end{cases} \tag{5.39}$$

In the covariance analytic method, all the parameters except r are estimated from the eigenanalysis of $\hat{\Sigma}$, the average of the covariance matrices. Therefore the natural choice to define a distance in this case is to compute directly the log-Euclidean distance following Eq 5.18:

$$d_{\text{covariance analytic}}(F_1, F_2) = ||\log(\Sigma_1) - \log(\Sigma_2)||_F \tag{5.40}$$

This metric (which is a distance in this case) is used to compute the similarity matrix following Eq 5.11

5.4.2.5 log VMF

We now explore the option to use the VMF to compute μ and κ and recover only ν from $\hat{\Sigma}$. We want to consider a VMF distribution as a point in a Riemannian manifold following geometric information methods. To define a metric on PDF spaces, a theoretical framework exists using partial derivatives of the PDF though Christoffel symbols[Amari 2007]. We tried to apply such a framework to VMF distributions, unfortunately, the corresponding partial derivative equations are not solvable. Therefore, to consider a VMF as a point of a Riemannian manifold, the two parameters need to be treated separately.

The space $\mathcal{S}^2 \times R^+$ where the couple of parameters (μ, κ) evolves is a Riemannian manifold as a product of two Riemannian manifolds. Therefore the averaging of the two parameters μ and κ can be treated independently. To average several points, a geodesic on these manifolds is defined (refer to [McGraw 2006] for details). Following this geodesic, the orientation averaging is similar to tensor averaging as in Section 5.4.1. The interpolation of κ is done recursively by projection as in McGraw et al. Letting $\kappa = \kappa_1$, we repeat until convergence (i.e until $l_\kappa < \varepsilon$):

$$l_\kappa = \sum_{i=1}^{n} w_i \log\left(\frac{\kappa_i}{\kappa}\right) \tag{5.41}$$

$$\kappa = \kappa \exp(l_\kappa) \tag{5.42}$$

This iterative methods converges to the Frechet mean in the tangent space. Similarly to the covariance analytic method, we then use the relation $r^2 = \nu d$. Then knowing all parameters except ν, we obtain it from $\hat{\Sigma}$ using (Eq 5.36 and Eq 5.38). As 2 equations are available to estimate one parameter, we compute the least square solution to ensure more stability:

$$\nu = \frac{r^2[2r^2 + \lambda + \lambda_\perp(1+\kappa)]}{2(r^2+\lambda)[r^2 + \lambda_\perp(1+\kappa)]} \tag{5.43}$$

The log VMF metric in the Riemiannian manifold $S^2 \times R^+$ belongs to the log-space for both direction and concentration parameters. Therefore we compute the distance of tensors and the distance of κ with their corresponding Riemannian metric which give the following semimetric between compartments:

$$d_{\text{logVMF}}(F_1, F_2) = ||\log(T_1) - \log(T_2)||_F + \alpha|\log(\kappa_1) - \log(\kappa_2)| + \beta||r_1 - r_2||_2^2 \tag{5.44}$$

where α, β and γ are normalization coefficients.

5.5 Experiments and results

5.5.1 DDI compartment averaging evaluation on simulated data

We first evaluate DDI compartment averaging into a single one. To do so, we simulate random DDI compartments by drawing parameter values from uniform distributions between different bounds depending on the parameter: $[0, 20]$ for κ, $[5.10^{-4}, 5.10^{-3}] mm^2.s^{-1}$ for d, $[0, 1]$ for ν, and random orientation on S^2 for μ. Four random DDI compartments are computed, that correspond to the four corners of a grid of size 11×11 that we want to extrapolate. The reference is a grid containing 4 compartments per pixel with a weight proportional to the position of the voxel with respect to each corner (see Fig. 5.4.e). For each method, we average each pixel of the reference image into only one DDI compartment. To quantitatively evaluate DDI averaging, we simulate, for each method and the reference, a DWI signal from DDI models following Eq. (6) in [Stamm 2012b] on 60 directions for each of 3 different b-values (1000, 2000 and 3000 $s.mm^{-2}$). A Euclidean distance between simulated DWIs of the 4 methods and the reference provides quantitative results.

To perform a robust experiment, we created a database of 500 sets of 4 corners. Then taken as the Euclidean distances on the 500 random images are normalized so that the simplest error mean is 100. The result for the different methods are simplest: 100, tensor: 31.6, log VMF: 28.0, covariance analytic: 11.1. We present in Fig. 5.4 representative images from averaged DDI models superimposed on the corresponding error maps. The simplest method has a large error explained by direction averaging. The tensor method is better: thanks to the orientation averaging part. However, there are still large errors which can be explained by large κ values in regions averaging orthogonal directions, which is not realistic. log VMF suffers

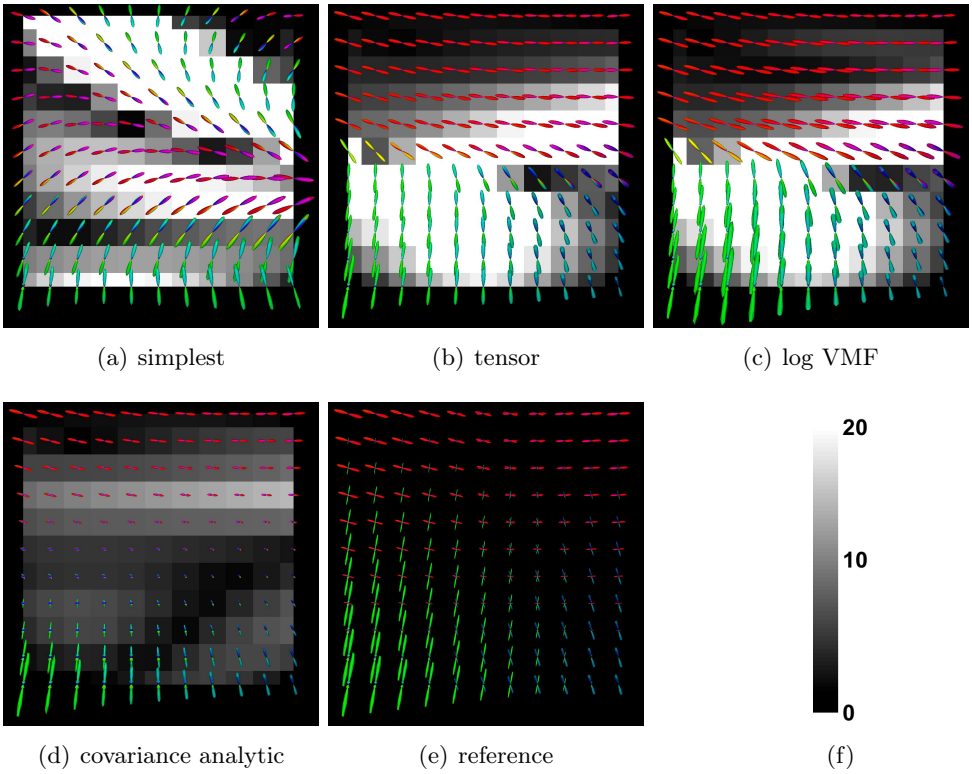

(a) simplest (b) tensor (c) log VMF

(d) covariance analytic (e) reference (f)

Figure 5.4: First four images (a-d) illustrate DDI averaging using the four methods superimposed on their local error maps. Image (e) is the reference. (f) Error map corresponding scalar bar.

from the same problem as tensor. Covariance analytic performs much better than all other methods. This is mainly due to smaller errors in crossing fibers. This is logical as when two orthogonal compartments are averaged, the best single compartment representing them is almost spherical, meaning a low κ value. The Euclidean distance map in the DWI signal confirms this idea.

5.5.2 MCM interpolation experiments on real data

5.5.2.1 Multi-tensors model

We now test the entire MCM interpolation pipeline including spectral clustering and isotropic compartments averaging. A MTM is estimated from a subject of the Human Connectome Project (HCP) data [Van Essen 2012] which is a DWI with $145 \times 174 \times 145$ voxels with a $1.25 \times 1.25 \times 1.25$ mm^3 resolution and 270 gradient directions over 3 b-values (1000, 2000, and 3000 $s.mm^{-2}$). The estimated MTM includes 3 anisotropic compartments (tensors) and 2 isotropic compartments (one free water with a diffusivity $d_{\text{free}} = 3 \times 10^{-3}$ $mm^2 s^{-1}$ and one restricted water with a diffusivity $d_{\text{restricted}} = 1 \times 10^{-3}$ $mm^2 s^{-1}$).

To test the global interpolation scheme, a rotation of angle 120 degrees is picked

around a random axis and then applied 3 consecutive times to the original MTM image. We then compare the final MTM obtained to the original one. To visualize the MTM, we compute the MTM PDF values on several points of a sphere and deform it using these values. As a consequence, the sphere will be elongated along the most probable diffusion directions and contracted elsewhere.

The visual representation of the original and interpolated MTM is presented in Fig 5.5. At the brain level, the MTM seem very similar to the original one though smoother. In the zoomed area, despite crossing in the original MTM, the rotated MTM stay close to the original models even in the crossing zone. As expected, the image is smoothed by the interpolation but all main orientations are recovered. We cannot perform quantitive evaluation on only one method, however at least visually after 3 consecutive interpolations the result seems very correct compared to the original MTM image.

5.5.2.2 DDI model

We then tested the entire MCM interpolation pipeline for the DDI model. To perform the validation of the different DDI interpolation methods on real data, we tested methods on a set of 46 real DDI images estimated from DWI with $128 \times 128 \times 55$ voxels with a $2 \times 2 \times 2$ mm^3 resolution, 30 gradient directions with one b-value $= 1000$ $s.mm^{-2}$. Input DDI models have been estimated with three DDI compartments and one free water compartment [Stamm 2016].

For each input DDI, we compute a rotation of angle 120 degrees and then apply it 3 consecutive times for each four methods: simpliest, tensors, log VMF and covariance analytic. From the 4 resulting DDI, one for each method, and the original one we compute the corresponding DWI images. These DWI are estimated from a set of 270 gradient on 3 shells ($b = 1000, b = 2000, b = 3000$ $s.mm{-}2$) coming from the HCP database [Van Essen 2012]. We then compute the Euclidean distance between each rotated DDI and the original one on the DWI corresponding images. All DDI methods and their corresponding DWI Euclidean distances are illustrated in Fig 5.6. The DDI image of the simpliest method seems very different to the original DDI image showing that the orientation of the interpolated compartments is not well estimated. At this scale, the DDI images of the three other methods look similar to the original DDI image. Regarding the DWI Euclidean distances, the two worst images correspond to the simplest and the log VMF methods, the best of all being the covariance analytic method. A deeper visual analysis of the 2 best methods will be made in the following, but first, we present the quantitative results.

For each DWI difference image the sum of the Euclidean distances is divided by the size of the mask of the brain, then the global results are normalized to set the median of the simplest method to 100. The results are presented in Fig 5.7. Means are respectively: simpliest 101.2, tensor: 69.1, logVMF: 118.1, covariance analytic: 58.0. The methods are classified in the same order for all 46 subjects showing very robust results (all paired t-tests, $p < 1.0 \times 10^{-18}$). The logVMF suffers from the

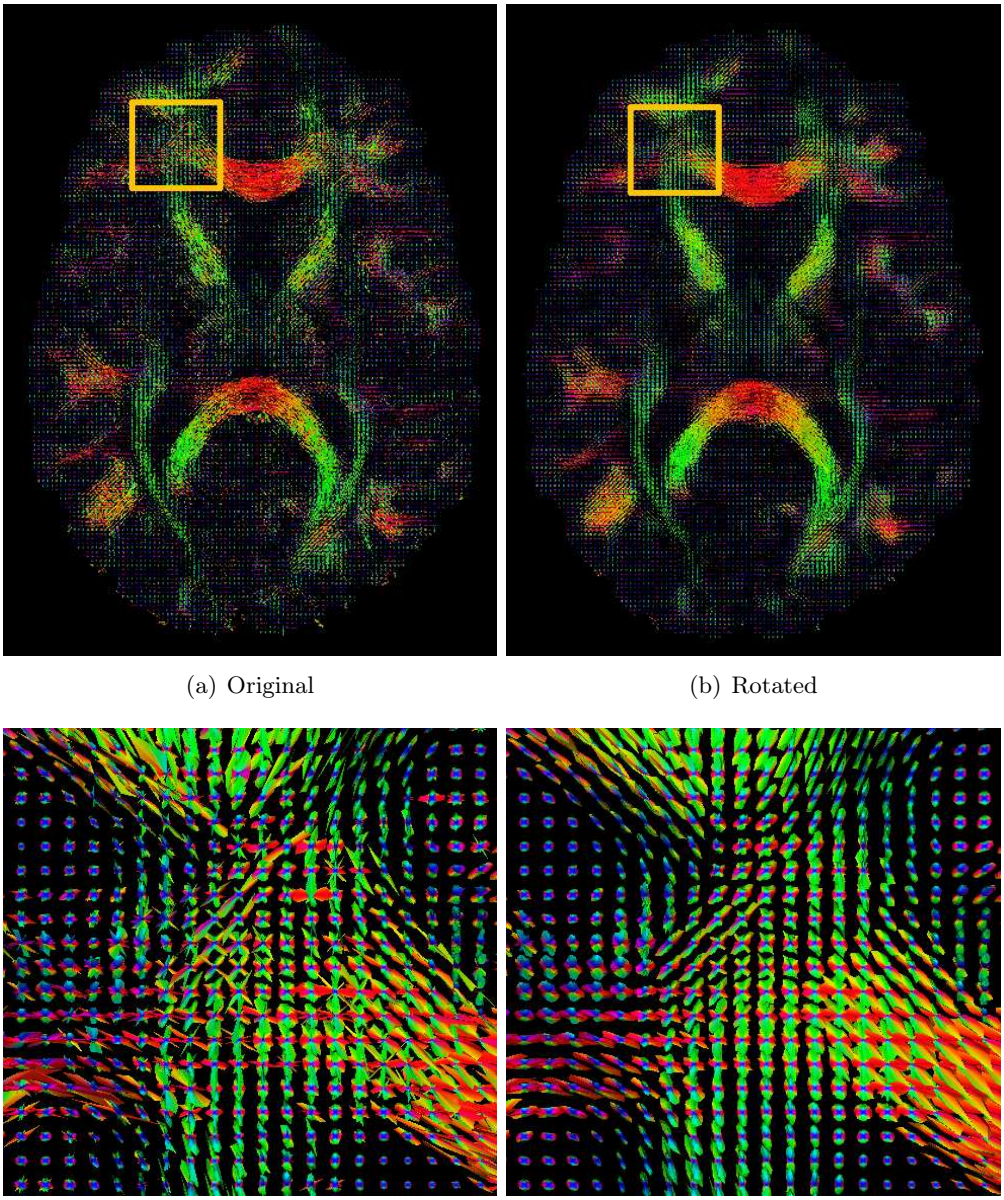

(a) Original (b) Rotated

(c) Original zoomed (d) Rotated zoomed

Figure 5.5: Visualisation of an original MTM image and its corresponding interpolation after 3 rotations. The MTM is estimated from a subject of the HCP data [Van Essen 2012] which is a DWI with $145 \times 174 \times 145$ voxels with a $1.25 \times 1.25 \times 1.25\ mm^3$ resolution and 270 gradient directions over 3 b-values (1000, 2000, and 3000 $s.mm^{-2}$). The estimated MTM includes comports 3 anisotropic compartments (tensors) and 2 isotropic compartments (one free water with a diffusivity $d_{\text{free}} = 3 \times 10^{-3}\ mm^2 s^{-1}$ and one restricted water with a diffusivity $d_{\text{restricted}} = 1 \times 10^{-3}\ mm^2 s^{-1}$).

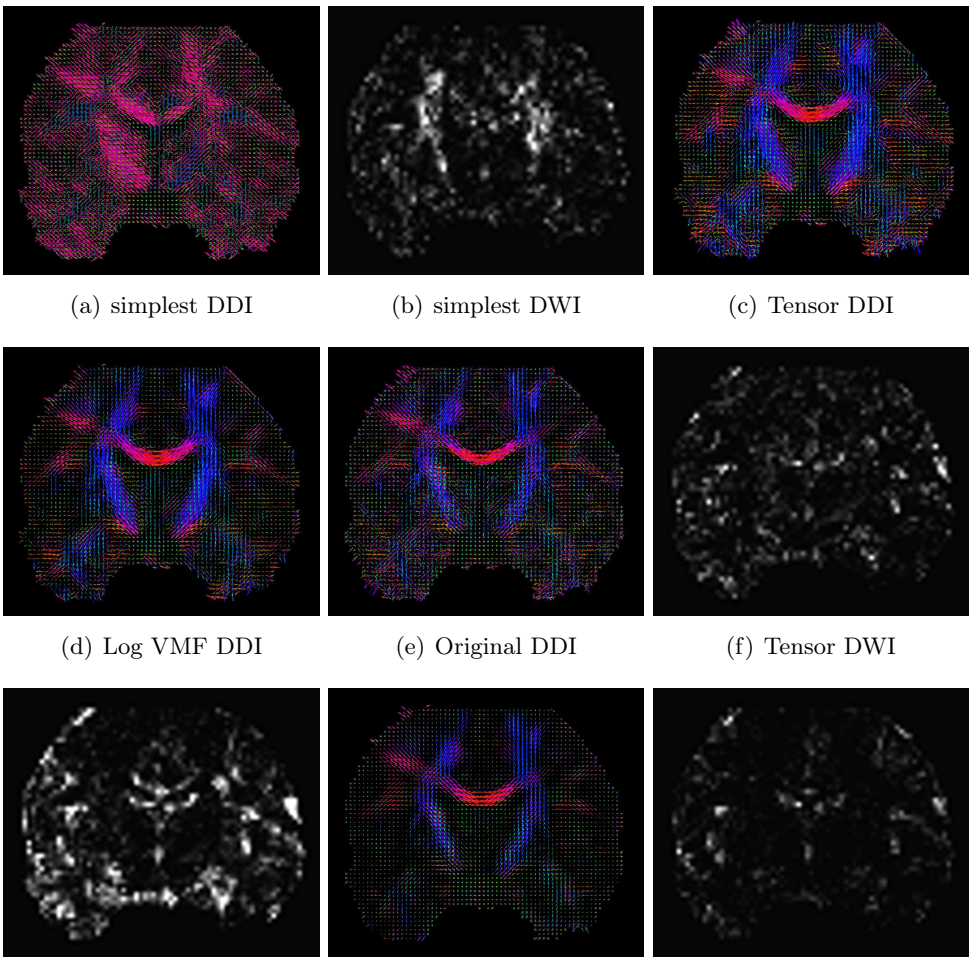

(a) simplest DDI (b) simplest DWI (c) Tensor DDI

(d) Log VMF DDI (e) Original DDI (f) Tensor DWI

(g) Log VMF DWI (h) Covariance DDI (i) Covariance DWI

Figure 5.6: Illustration of the 4 DDI interpolation methods: simplest, tensor, log VMF and covariance analytic. These DDI have been estimated from DWI with $128 \times 128 \times 55$ voxels, a $2 \times 2 \times 2$ mm^3 resolution and 30 gradient directions with one b-value = 1000 $s.mm^{-2}$. The interpolation is done after 3 consecutive rotation of 120 degrees. Each method is represent by two contiguous images, the interpolated DDI and the DWI Euclidean distances. The original DDI image is located at the center of the 9 images.

multiple interpolations and obtains worse results than the simplest method, which stays far from the two best methods. The covariance analytic performs significantly better than the tensor showing better robustness for several successive interpolations.

Following the same process than for MTM, we visualize the original DDI and the one rotated, for one of the 46 subjects of our dataset, by the 2 methods which obtained the best results, tensor and covariance analytic(see Fig 5.8). On the first line, the 3 images have the same aspect though the rotated DDI seems smoother

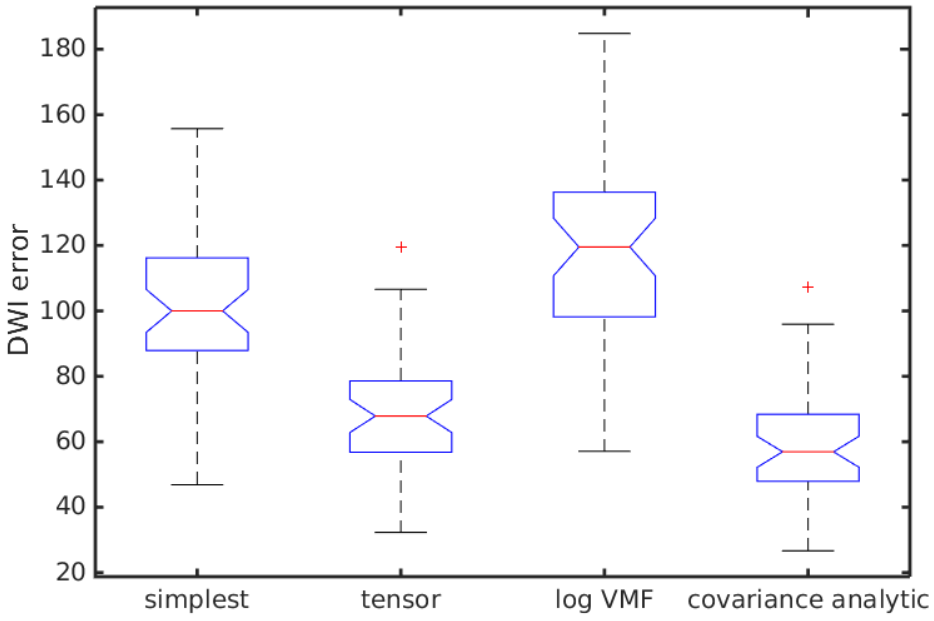

Figure 5.7: Error between the DWI corresponding images of the original DDI and the one estimated after 3 rotations following the 4 different methods.

than the original one, however more interesting observations come with a zoom. On the second line, the covariance analytic method compartments are smaller than the original ones probably due to an under estimation of the diffusivity. On the same line, the compartments size of the tensor method seem slightly bigger than the original DDI. The third line represents all the compartments at the same size to focus on the orientation. We can see that orientations of the compartments obtained with covariance analytic methods are very similar to the original ones while the compartments from the tensor method orientations seem different. These observations show that all these methods have imperfections confirming the complexity of the interpolation of MCM.

5.5.3 DDI Atlas Construction

The ultimate goal of the registration of MCM images is the production of an average atlas of the white matter microstructure. We computed an atlas from 46 DDI images following Guimond et al. atlas construction method [Guimond 2000]. This atlas construction was performed using non linear DTI registration as proposed by Suarez et al. [Suarez 2012]. Then, the obtained transformations were applied to the DDI models. We interpolated the DDI models using our clustering approach with the covariance analytic averaging. In addition, when applying a transformation to oriented models, it is necessary to apply the local linear part of the transformation

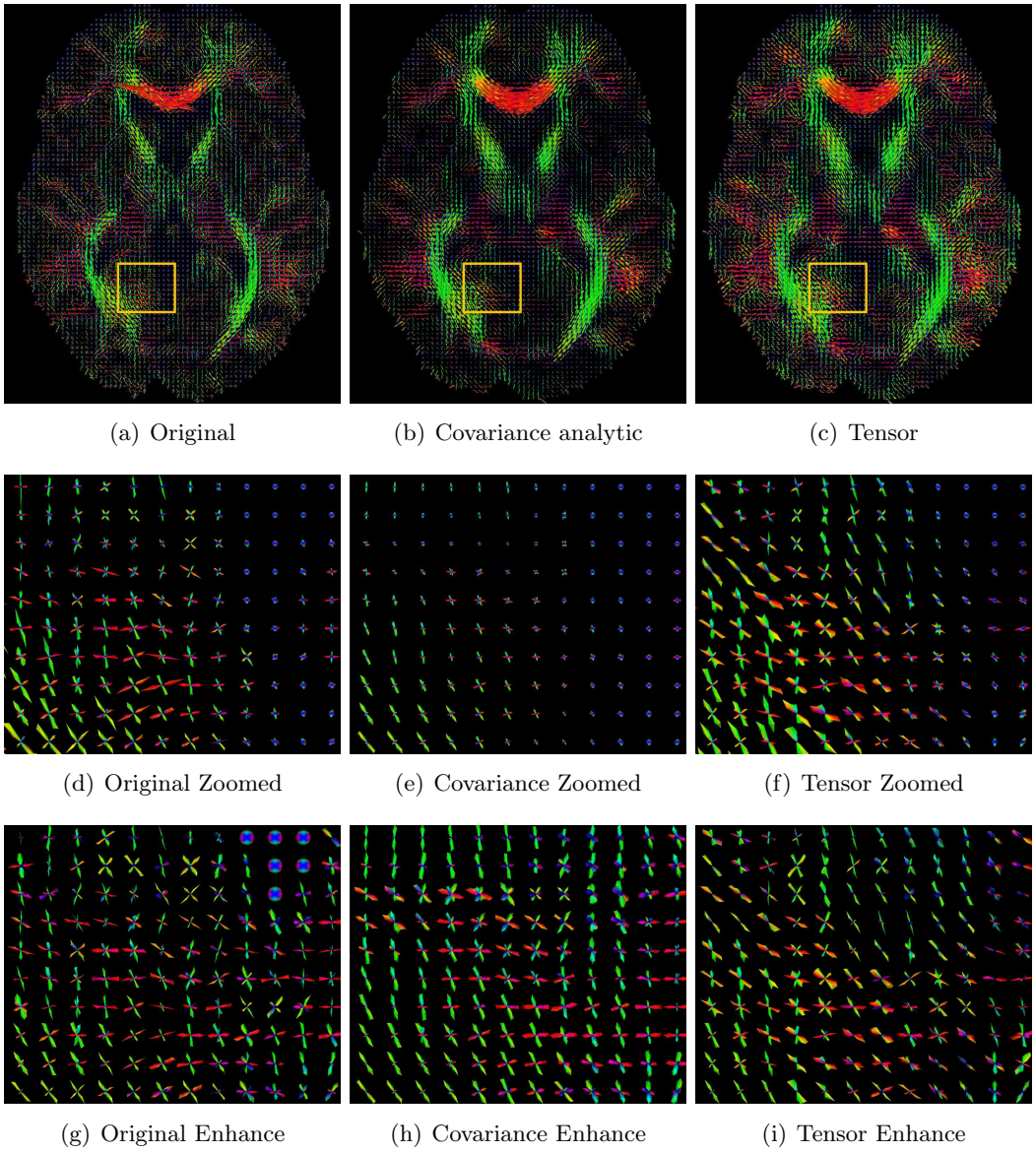

(a) Original (b) Covariance analytic (c) Tensor

(d) Original Zoomed (e) Covariance Zoomed (f) Tensor Zoomed

(g) Original Enhance (h) Covariance Enhance (i) Tensor Enhance

Figure 5.8: Illustration of 2 DDI interpolation methods, covariance analytic and tensor, compared to the original DDI. The interpolation is made applying 3 consecutive rotation of 120 degrees. The first line represent the original DDI and the two interpolated by the covariance analytic method and the tensor method. The second line represents the same DDI images zoomed on the yellow rectangle. The third line represents the same zoom with all the compartments normalized to the same size to focus on the orientation of the DDI compartments.

to the interpolated models. We used a technique similar to finite-strain reorientation for tensors [Ruiz-Alzola 2002a] by applying the local rotation to the μ_i directions of each anisotropic compartment of the interpolated DDI. We present the visual result

of the atlas and a zoomed area in Fig. 5.9. This atlas provides a clear distinction of crossing fibers and will be of great interest in future studies for example of white matter microstructure destruction in diseases.

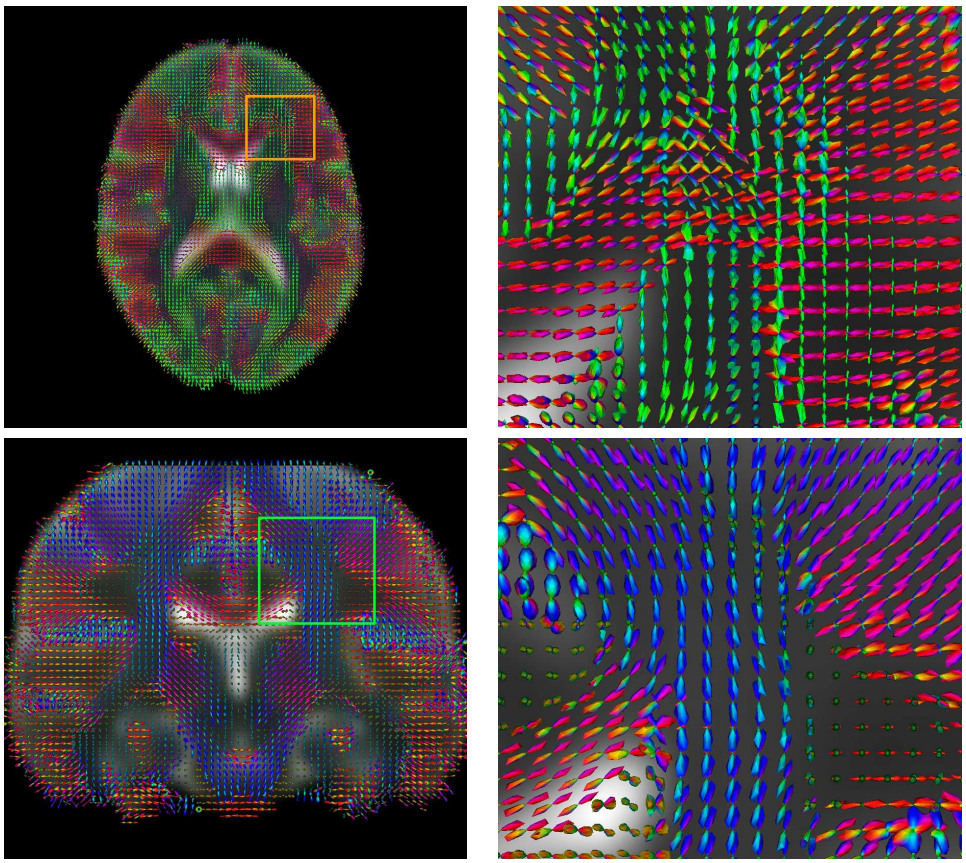

Figure 5.9: Example of a DDI atlas superimposed on the average B0 image: Axial view on the first line and coronal view. This atlas is constructed from our database of 46 real DDI images estimated from DWI with $128 \times 128 \times 55$ voxels with a $2 \times 2 \times 2$ mm^3 resolution, 30 gradient directions with one b-value = 1000 $s.mm^{-2}$.

5.6 Conclusion and perspective

We have addressed the problem of interpolation and averaging of MCM images. As MCMs become increasingly popular and used, the issue of interpolation (e.g. for a registration purpose) or averaging (e.g. for atlas creation) becomes acute in the absence of relevant dedicated solutions yet. We have proposed to perform interpolation as a MCM simplification problem, relying on spectral clustering and compartment averaging methods handling both isotropic and anisotropic compartment parameters. For this latter part, we have proposed and compared four different alternatives, for the DDI model these methods being evaluated with synthetic and real data. Ac-

cording to these different experimental conditions, the covariance analytic solution exhibits significantly better performance than the others. As we saw in the visual analysis there are still some question to be analyzed further on the attenuation of the diffusivity with the covariance analytic method, nevertheless it is able to robustly recover the orientation after several transformations.

Another accute problem is the number of clusters of the model. In our experiments, the number of anisotropic compartments is the same for the entire image. *A priori*, some parts of the brain do not need 3 compartments in addition to a free water compartment. Tools based on akaike information criterion (AIC) [Sakamoto 1986] exist to compute a specific number of compartments for each voxel . The number of compartments after interpolation in our algorithm is however fixed for the entire image. Simple solutions towards handling better images with varying number of anisotropic compartments include taking the mean or maximum of the number of clusters of the input voxels do not support successive transformations.

We can also imagine smart algorithms to estimate automatically the optimal number of clusters after interpolation. Such methods already exist for spectral clustering based on rotation of the spectral vector [Zelnik-Manor 2004] or the selection of eigenvalues [Sanguinetti 2005]. Unfortunately they cannot consider one cluster as a solution and are thus not directly applicable to our problem.

Chapter 6

From Multi-Compartment Models to Statistics

Contents

6.1 Introduction

A clinical study often includes data from a group of healthy subjects, named controls, and a group of patients affected by the same disease. From such a database, we are looking for biomarkers that highlight anatomical abnormalities. A longitudinal study can also compare the evolution of the symptoms along the successive MRI scanners. One solution is to manually select region of interest (ROI) of damage tissues for a particular disease for one or several patients [Filippi 2001, Werring 2000].

Then a comparison can be made with healthy tissue to follow the evolution of one patient along several MRI scans or compute statistic for a population.

For now, the majority of clinical dMRI is made from DWI acquisitions with a limited number of b-values and directions, using scalar maps as MD or simple models as DTI to investigate the brain microstructure. More complex models, such as MCM, are instead specifically designed to reveal this microstructure. Therefore, fine biomarkers can be considered to better interpret the damage and evolution of a disease.

From a group of patients and a group of controls, there are mainly two ways to study the influence of a disease. First, the two populations (controls and patients) can be aligned on a template to perform a voxel-wise comparison or tract-based statistics. One method is to make a patient population versus a control population comparison [Whitcher 2007, Lepore 2008]. This method allows to highlight general biomarkers common to a population and, therefore, improves the understanding of a particular disease. These techniques are interesting in that they do not require the tedious ROI delimitation. However, diseases with too much variability, such as multiple sclerosis (MS), are not well-adapted for this kind of statistics. Here, we prefer to compare one patient again the entire group of control [Commowick 2008]. Contrarily to the population versus population, this method does not reveal statistically robust biomarker for a disease at a population level. Instead, it offers the possibility to highlight particular changes of some parameters specific to a patient evolution for each patient individually and thus to perform longitudinal studies.

In this chapter, we propose two different approaches that exploit the potential of MCM to better understand and describe patient disease and evolution: one solution from voxel-based analysis and one solution from tract-based analysis. The classical voxel-based method considers each voxel independently to compute statistics. For the second method, a tractography is computed from an average control derived from the atlas. Parameters are extracted along the fibers for the patient and the controls and subsequently used to compute statistic. The voxel-based and the tract-based methods are respectively presented in Sections 6.4 and Section 6.5.

6.2 Atlas based patient to group statistics

6.2.1 General method

An atlas, in neuroscience, is a collection of brain images, brain representation or brain labeling. First, print atlases were used to guide surgical operations [Talairach 1988, Schaltenbrand 1998]. Now, progress in image processing allows to automatically estimate all kinds of atlas [Woods 1999, Commowick 2007, Lancaster 2000, Cabezas 2011]. We consider in this chapter an atlas as a collection of control acquisitions registered on the same support.

It is possible to compute an evolving atlas that can easily integrate an extra acquisition to the current average atlas through weighted average or geodesic[Beg 2006]. However, these methods are more adaptive to big data as the HCP when it is highly

time consuming to compute an other atlas. Here, we follow a process to create an atlas from a data collection once and for all. We want to perform patient to group comparison. To do so, the following steps are processed:

- **Creation of an atlas.** For one or several modalities, the entire collection of data control is first pre-processed: denoising, distortion correction, MCM model estimation (see Section 6.3). Then the pre-processed images are registered on the same space. The resulting collection of images is called an atlas $\mathcal{A}$. From this point on, the control subjects in $\mathcal{A}$ all have the same position in space and scalar or compartment values extracted at a given voxel or along a given tract are comparable. The atlas creation and the registration method are respectively detailed in Section 6.2.2 and Section 6.2.3. The creation of the atlas is made off-line, once and for all.

- **Patient to population comparison.** For each new patient, the DWI acquisition is registered on the atlas using the same pre-processing and registration technique. The patient image is thus aligned with all controls in $\mathcal{A}$ and may be compared to the population. We present two different approaches for statistical comparison: one voxel-based solution in Section 6.4 and one tract-base solution in Section 6.5.

6.2.2 Atlas construction

We assume in this section that we are able to compute a transformation between two individual brain images. The registration algorithm used for this task will be presented in Section 6.2.3. Unfortunately we do not currently use a specific MCM registration method which is part of the perspective of this work. Therefore, the atlas is created from the DTI models. Then, the corresponding transformations can be applied to any MCM, using the MCM interpolation method proposed in Chapter 5, to contruct a MCM atlas. From a database of control images $T_1, ..., T_N$ (here the DTIs computed from the DWI images) , the atlas is computed iteratively as follows [Guimond 2000]:

- T_R is the DTI reference, at first iteration $T_R = T_1$.

- Until convergence, i.e until the average diffeomorphic transformation $\mathcal{D}_{\text{avg}}$ is almost null, do:

  1. Register all DTIs $T_1, ..., T_N$ on T_R following Section 6.2.3. Let $\mathcal{R}_1, ..., \mathcal{R}_N$ be the corresponding transformations (at the first iteration $\mathcal{R}_1$ is null). Each $\mathcal{R}_i$ is the composition of an affine and a diffeomophic transformation $\mathcal{R}_i = \mathcal{A}_i \circ \mathcal{D}_i$
  2. Average all the registered DTIs into a single one T_{avg} in the log-Euclidean space of tensors:

$$\log(T_{\text{avg}}(x)) = \frac{1}{N}\sum_{i=1}^{N}\log(\tilde{T}_i(x)) \tag{6.1}$$

where log denotes the matrix logarithm and $\tilde{T}_i$ is T_i resampled with $\mathcal{R}_i$ with its tensors reoriented appropriately [Ruiz-Alzola 2002b].

3. Average all the diffeomorphic transformations with the log-Euclidean framework for diffeomorphisms to recover an average transformation $\mathcal{D}_{\text{avg}}$:

$$\log(\mathcal{D}_{\text{avg}}) = \frac{1}{N}\sum_{i=1}^{N}\log(\mathcal{D}_i) \tag{6.2}$$

where log denotes here the logarithm of a diffeomorphism.

4. The new DTI reference T_R is obtained applying $\mathcal{D}_{\text{avg}}^{-1}$ to T_{avg}.

Finally, we have the initial DTIs with the corresponding final transformations $\mathcal{R}_1, ..., \mathcal{R}_N$. These transformations can be used to estimate a DTI atlas. They are applied to the MCMs computed from the original DWIs to create a MCM atlas.

6.2.3 Registration

From a group of images (medical or not), there exist several ways to register them. A non-exhaustive review of the large literature on the non-linear registration methods has been proposed recently [Klein 2009]. Here, from two sets of DWI, we assume one fix subject F and one moving subject M. We want to compute a global transformation $\mathcal{R}$ that sends F to M, i.e $F(x) = M \circ \mathcal{R}(x)$. This purpose is however an ill-posed problem, hence, T has regularity constraints. As mentioned in the previous section, wa have not yet developed registration tools for MCM (especially the similarity measure between MCMs). Therefore, from the two sets of DWI, the corresponding DTI, T_F and T_M are estimated. Then the derived MD scalar maps A_F and A_M are computed. The global transformation comes from two transformations, i.e $\mathcal{R} = \mathcal{A} \circ \mathcal{D}$:

- An affine transformation $\mathcal{A}$ to roughly register the moving image on the fixed image.
- A dense transformation $\mathcal{R}$ estimated as a smooth constrained concatenation of local affine BM transformations [Commowick 2012c].

The first transformation is estimated with a block-matching algorithm from the two scalar maps A_F and A_M [Ourselin 2000]. Then, this transformation is applied to T_M. The dense transformation is recovered by matching this temporary registered DTI on the fixed DTI. Finally, the global transformation is the combination of these 2 transformations.

We do not remind the entire BM algorithm as it is largely described in Chapter 4 and [Commowick 2012c], yet we can notice some important differences. Contrary to

local transformations in distortion correction specifically designed for the distortion model, here, transformations are classical rigid transformations. These transformations are applied to DTI instead of scalar images. Thus a tensor interpolation is done following the log-Euclidean framework (see Section 3.3.4.6) and tensors are reoriented using finite strain reorientation [Ruiz-Alzola 2002b].

The similarity measure cannot be a well-defined correlation coefficient between blocks of scalar values anymore. Instead, we use a generalized correlation metric adaptable to the tensor case proposed by[Suarez 2012]. The total covariance matrix is expressed as:

$$\Lambda(X,Y) = \begin{pmatrix} \Sigma_{X,X} & \Sigma_{X,Y} \\ \Sigma_{Y,X} & \Sigma_{Y,Y} \end{pmatrix} \tag{6.3}$$

where X, Y are the 6D log-tensors respectively in the fixed and in the registered blocks. Each $\Sigma_{.,.}$ is the 6×6 covariance matrix between the 6D log-tensors. The correlation matrix $\Gamma(X,Y)$ is then defined as:

$$\Gamma(X,Y) = \Sigma_{X,X}^{-\frac{1}{2}} \Sigma_{X,Y} \Sigma_{Y,Y}^{-\frac{1}{2}} \tag{6.4}$$

The generalized squared correlation coefficient (GCC) is finally expressed as:

$$\mathrm{GCC}(X,Y) = \frac{1}{6}\mathrm{Tr}\left(\Gamma(X,Y)^{\top}\Gamma(X,Y)\right) \tag{6.5}$$

The general transformation obtained can be applied to the DTI as well as any MCM following the interpolation scheme presented in Chapter 5. For both cases, reorientation is done using finite-strain reorientation.

6.3 Experimental design

6.3.1 Database

The pipeline presented previously is tested on the USPIO dataset [Crimi 2014]. This study, named after the contrast agent ultrasmall super paramagnetic iron oxid (USPIO), consists of two groups: patients suffering MS (at a very early stage: first event suggestive of MS, i.e clinically isolated syndromes (CIS)) and control subjects. Images were acquired in 5 French centers, for a total of 36 patients and 46 controls. For each patient and control among other modalites, we used the following images:

- **A DWI acquisition** with a spatial resolution $128 \times 128 \times 55$, a corresponding voxel size $2 \times 2 \times 2$ mm^3 with 30 gradient directions acquired on one shell ($b = 1000$ $s.mm^{-2}$).
- **A T2 TSE** with a spatial resolution $192 \times 256 \times 44$, a corresponding voxel size $1 \times 1 \times 3$ mm^3. The other parameters were set to obtain a T2-weighted image (TR $= 6530ms$, TE $= 84ms$). A T1-weighted image was also acquired. For a better comparison, in all the figure illustrations of this chapter, these structural image, are resampled on the DWI acquisition for anatomy visualization.

From the entire dataset, a subset of 46 controls and 20 patients is used as our dataset. Our atlas $\mathcal{A}$ is thus constituted from the 46 controls registered for DDI, DTI models and also structural images. The DDI are resampled using the covariance analytic metric presented in Section 5.4.2.4 and with finite strain reorientation of the anisotropic compartments.

6.3.2 Preprocessing pipeline

For all patients and controls some preprocessing steps to enhance the DWI acquisitions were performed.

6.3.2.1 Distortion correction

We have seen in Chapter 4 that EPI suffers from distortion artifacts and we proposed a method to correct these distortions. Unfortunately, the USPIO study started in 2009 and extra acquisitions with reversed PED were not included in the protocol at this time. Therefore, although we advocate for reversed PED based correction for future studies, the distortion correction is here roughly performed using a simple registration from the b_0 image to the T2-weighted image [Ourselin 2000, Commowick 2012c]. All the new protocols of our team concerning dMRI now include a reversed PED image to correct distortion as presented in Chapter 4.

6.3.2.2 Denoising

A denoising step is then performed to enhance images quality. This is done using a non-local means (NLM) method specifically adapted for the Rician noise in DWI acquisitions [Wiest-Daesslé 2007]. The algorithm uses the redundancy of information on the whole DWI dataset to denoise each DWI image.

6.3.2.3 Model estimation

From the preprocessed DWI acquisitions, DDI models are estimated. The non-linearity of the cost function makes it hard to minimize. Hence, the minimization is performed trough successive steps by revealing the parameters progressively [Stamm 2016]. First a stick model is estimated, then a zeppelin model and finally the DDI model (see Section 3.5.3.1 for more details). Each DDI is computed with 3 anisotropic compartments and one isotropic compartment (with a fixed diffusivity equal to $d_{\text{free}} = 3.10^{-3} mm^2.s^{-1}$ corresponding to a free water compartment). Each DTI is estimated with a linear least square solution on the log acquired signals [Westin 2002].

6.3.3 Scalar parameters evaluation

We describe in this section microstructure parameters potentially of interest that can be evaluated from the DDI images in our framework. Each DDI comports one

free water compartment with a fixed diffusivity and a corresponding weight w^1_{iso}, and several anisotropic compartments and their corresponding weights w^i. Each anisotropic compartment is described by 5 parameters : d is the diffusivity along the axon, κ is the orientation concentration index, ν is a non Gaussianity parameter, μ is the main diffusion orientation. The only parameter of the free water compartment is its weight w_{iso}. However, for anisotropic compartments, classical diffusivity and anisotropy measures can be derived from their parameters [Stamm 2013]:

- **The axial diffusivity** $d_{\parallel}$ that represents the diffusivity along the principal direction of diffusion is expressed as:

$$d_{\parallel} = d(1 - 2\nu\xi(\kappa)) \tag{6.6}$$

with

$$\xi(\kappa) = \frac{\cosh(\kappa)}{\kappa \sinh(\kappa)} - \frac{1}{\kappa^2} \tag{6.7}$$

where cosh is the hyperbolic cosine and sinh is the hyperbolic sine.

- **The radial diffusivity** $d_{\perp}$ represents the diffusivity in the orthogonal plane of the axial diffusivity:

$$d_{\perp} = d\left(\frac{1-\nu}{1+\kappa} + \nu\xi(\kappa)\right) \tag{6.8}$$

- **The mean diffusivity (MD)** that represents the average diffusivity in all directions it thus defined as:

$$\hat{\lambda} = \frac{d_{\parallel} + 2d_{\perp}}{3} \tag{6.9}$$

- **The fractional anisotropy (FA)** describes the degree of anisotropy of the compartment, FA belong to $[0, 1]$:

$$\text{FA} = \frac{d_{\parallel} - d_{\perp}}{\sqrt{d_{\parallel}^2 + 2d_{\perp}^2}} \tag{6.10}$$

6.3.4 Statistical test

We consider our atlas $\mathcal{A}$ containing n registered images $\{C^i\}_{i=1,..,n}$ of diffusion models (DDI or DTI) of control subjects. From one image of a patient C^0 registered on the atlas, it is thus possible to compute different statistics. The statistical test is common to the voxel-based and the tract-based approaches. Hence, let us assume that we have in one point x (voxel or tract) a parameter p extracted. For each point x, $\{C^i_{x,p}\}_{i=1,..,n}$ denotes the value of p for all the control images and $C^0_{x,p}$ the value of p for the patient image. Hence, a z-score can be computed:

$$z_x = \frac{C^0_{x,p} - \mu_{x,p}}{\sigma_{x,p}} \tag{6.11}$$

where $\mu_{x,p}$ and $\sigma_{x,p}$ are respectively the mean and standard deviation of the parameter p at the voxel x for the entire population, the control group excluding the patient. The z-score is a normalized measure, i.e it does not depend on the mean and the standard deviation of a variable. A negative z-score means a patient parameter value is lower than the average value of the control parameters and inversely for a positive value. The scaled z-score is assumed to follow a Fisher distribution $F(1, n-1)$ and is thus used to compute a p-value:

$$p(z_x) = 1 - F_{1,n-1}\left(\frac{N(N-1)}{N^2-1} z_x^2\right) \tag{6.12}$$

where $F_{1,n-1}$ is the cumulative distribution function of a Fisher distribution with parameters 1 and n-1 and p is the corresponding p-value.

6.4 Voxel based method

6.4.1 Voxel specific measures

We present a visual result of the voxel-based analysis for one patient. The comparison is made between the DDI model and the DTI model. For the DTI models, the classical FA and MD values are computed following respectively Eq 3.15 and Eq 3.16. For the DDI models, the free water and anisotropic compartments are separated. For the free water compartment, the weight of the compartment is computed. For the anisotropic compartments, the three AD and RD extracted for each compartment are averaged into two global measures:

$$\begin{cases} \hat{d_{\parallel}} = \sum_{i=1}^{3} \frac{d_{\parallel}^i}{3} \\ \hat{d_{\perp}} = \sum_{i=1}^{3} \frac{d_{\perp}^i}{3} \end{cases} \tag{6.13}$$

where $d_{\parallel}^i$ and $d_{\perp}^i$ are respectively the axial diffusivity and radial diffusivity of the i-th anisotropic compartment. The global MD and FA are derived from these average axial and radial diffusivity following Eq 6.9 and Eq 6.10.

6.4.2 Results

The z-scores of all these parameters for DDI and DTI models are presented Fig 6.1. As expected around the lesions, the destruction of myelined fibers results into an increase of the MD combined with a decrease of the FA. For the DDI model, the injury of myelin and axons results in a strong increase of the free water compartment weight. This also results into a small decrease of the MD into the average anisotropic compartments measure. We propose an explanation of such a behavior in the next section with tract-based analysis.

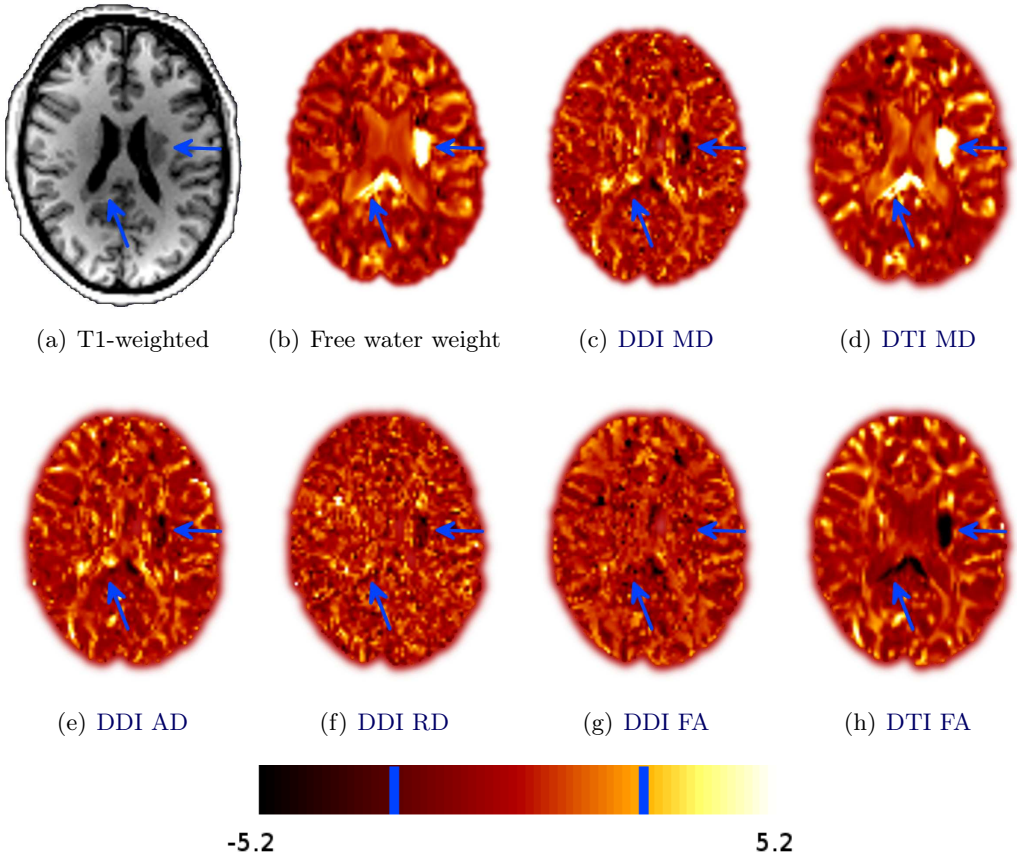

(a) T1-weighted (b) Free water weight (c) DDI MD (d) DTI MD

(e) DDI AD (f) DDI RD (g) DDI FA (h) DTI FA

(i) Scalar bar

Figure 6.1: Illustration of the z-score (patient vs atlas controls) on several parameters. The z-score scalar bar is presented in (i), a negative z-score means a patient parameter value under the average controls and a positive z-score a value superior to the average. Values outside the blue marks denote a p-value under 0.05. (a) T2-weighted image. (b) DDI free water compartment weight. (c) DDI mean diffusivity. (d) DTI mean diffusivity. (e) DDI axial diffusivity. (f) DDI radial diffusivity. (g) DDI fractional anisotropy. (h) DTI fractional anisotropy. The DDI free water compartment weight and the DTI MD clearly highlight the lesion indicated with the horizontal arrow with an important positive z-score. The DTI FA and, to a lesser extent, the DDI MD and the DDI AD also highlight the lesion with a negative z-score. This denotes the free water DDI weight and the DTI MD and FA as the best to characterize lesions. The other DDI parameters are relatively weaker biomarkers. This can be explained by the difficulty to analyze together parameters of several anisotropic compartments at a voxel-level.

We illustrate in the Fig 6.2 and 6.3, the DDI free water weight of a patient compared to the average free water scalar map of all the controls in the atlas. This results, as shown before, into an important increase of the free water compartment weight that is clearly highlighted by the corresponding z-scores. We can already conclude on the fact that the increase of MD is probably attributed to a large increase in free water, showing the interest of MCM to better understand from dMRI, what is happening .

6.5 Tracts-based method

6.5.1 Introduction to tractography

Before going into more details about the tract-based framework, we first briefly present tractography. Tractography is a method to model the WM tracts in the brain, from dMRI, represented by 3D curves without diameters. A tractography is computed from a diffusion model, generally the DTI, but not necessarily. There are various algorithms to perform this task. They can be mainly classified in two types: deterministic and probabilistic [Yamada 2009]. The DTI model has some issues and strengths due to its simplicity (see Section 3.3). Hence, a tractography performed from a DTI has the corresponding problems, in particular in crossing fiber areas [Yamada 2007, Wedeen 2008]. In Section 6.5.3, we propose a deterministic tractography algorithm specifically designed for MCM.

As basic dMRI, tractography is used in clinic in several diseases: strokes, multiple sclerosis (MS), epilepsy, brain tumors, spinal cord disorders and more [El-Sourgy 2015, Ciccarelli 2008, Hagler 2009, Hesseltine 2007, Akai 2005, Holodny 2001, Parmar 2004]. A tractography provides useful information for surgical operation to avoid damage of motor tracts. It is used for both surgical planning and post-procedure evaluation [Romano 2009, Berman 2009, Yu 2005]. The tractography is generally performed once for all before the surgery with fixed parameters. However, recent work on real-time fiber tracking can offer a direct and adaptable visualization during the surgery [Chamberland 2014]. Tractography can also be used to do statistics as we will see in the following [Smith 2006].

6.5.2 Tract-based statistical test

We assume that we have a tractography $\mathcal{T}$ adapted for all the registered images computed from an average DDI. The computation of such a tractography in described in details in Section 6.5.3. For now, let just notice that a tractography is a sequence of spatial positions and thus the derived local directions can be estimated. For each DDI registered on our atlas (both control and patient), parameter values are added to $\mathcal{T}$. Contrarily to the voxel-based approach, the parameters are directly extracted from one compartment. For each point r that belongs to $\mathcal{T}$, we do the following:

- Estimate, for one patient C^0 and all DDI control images registered $\{C^i\}_{i=1,\dots,n}$

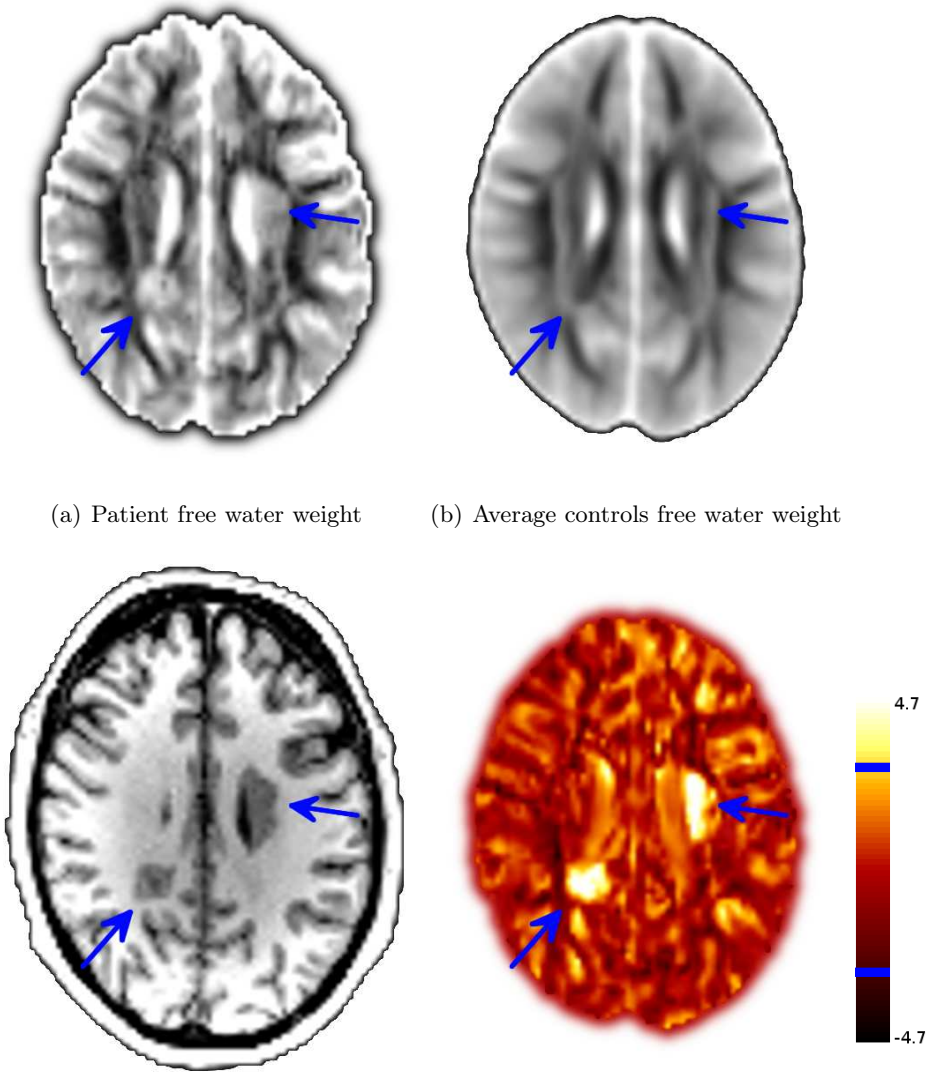

(a) Patient free water weight

(b) Average controls free water weight

(c) T1-weighted

(d) Patient free water z-score

Figure 6.2: Illustration of the voxel-based analysis. (a) Patient free water weight scalar map. (b) Average of the free water weight scalar map of all the DDI controls on the atlas. (c) T2-weighted image of a patient, MS lesions are highlighted with blue arrows. (d) Z-score of the patient free water weight scalar map compared to the atlas. A negative z-score means a patient parameter value under the average controls and a positive z-score a value superior to the average. Values outside the blue marks denote a p-value under 0.05.

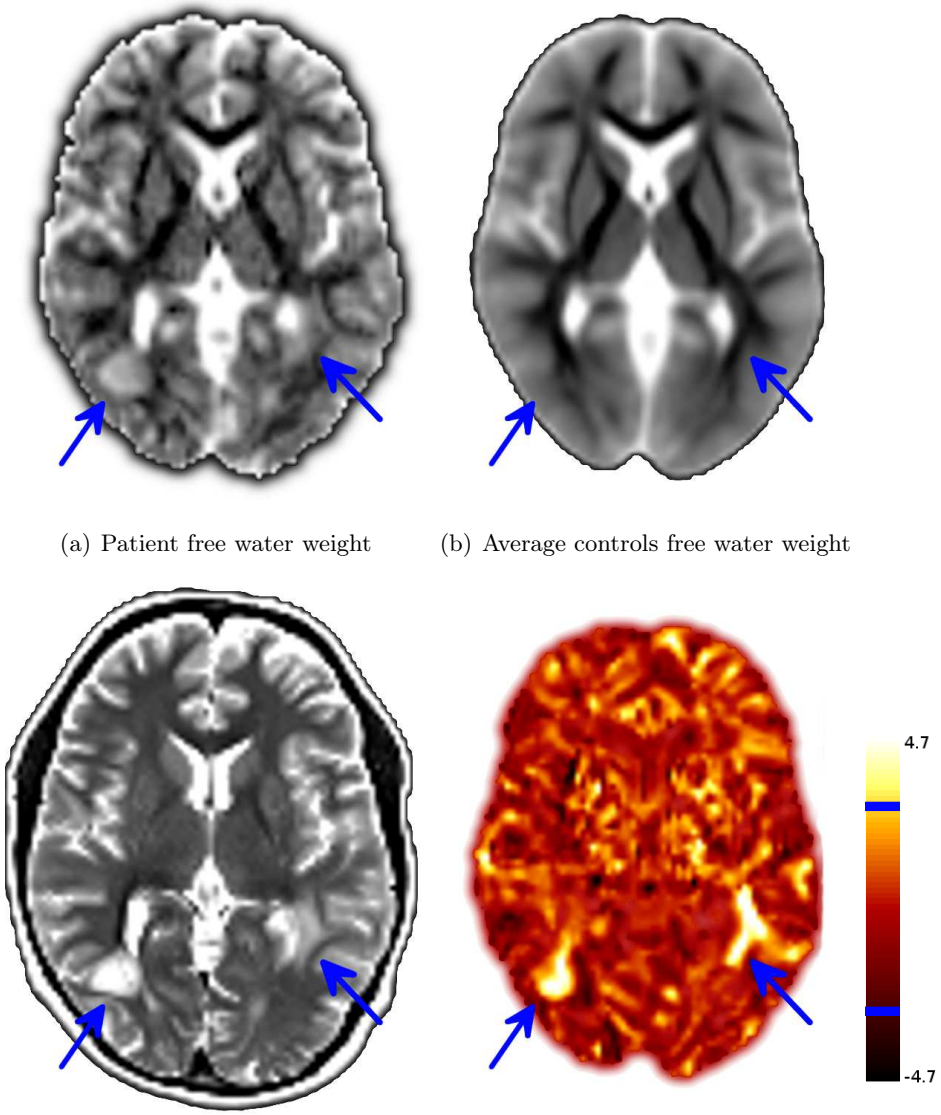

(a) Patient free water weight

(b) Average controls free water weight

(c) T1-weighted

(d) Patient free water z-score

Figure 6.3: Illustration of the voxel-based statistic. (a) Patient free water weight scalar map. (b) Average of the free water weight scalar map of all the DDI controls on the atlas. (c) T2-weighted image of a patient, MS lesions are highlighted with blue arrows. (d) Z-score of the patient free water weight scalar map compared to the atlas. A negative z-score means a patient parameter value under the average controls and a positive z-score a value superior to the average. Values outside the blue marks denote a p-value under 0.05.

at the spatial position P_r of point r, the interpolated MCM $\{M_r^i\}_{i=0,\dots,n}$ using the MCM interpolation framework (see Chapter 5).

- At each point r, let $D_r^{\mathcal{T}}$ be the direction of $\mathcal{T}$. For each $\{M_r^i\}_{i=0,\dots,n}$, select the anisotropic compartment $\{M_r^{i,q(i)}\}_{i=0,..,n}$ with the closest orientation compared to $D_r^{\mathcal{T}}$:

$$q(i) = \underset{i\in[1,\dots,p]}{\arg\max} \; | < D_n, O^i_{\mathcal{M}_n} > | \tag{6.14}$$

  where $| < D_n, O^i_{\mathcal{M}_n} > |$ is the cosine between the i-th anisotropic compartment and the current direction and $q(i)$ is the selected compartment number.

- For all of the $n+1$ DDI registered $\{M_r^i\}_{i=0,\dots,n}$, extract the corresponding parameter $\{C^i_{r,p}\}_{i=0,..,n}$ from the selected compartment $M_r^{i,q(i)}$.

- Finally, compute the statistical test for the patient versus controls with the z-score and p-value computation and affect these values to $\mathcal{T}$.

6.5.3 Tractography from MCM

6.5.3.1 Tractography algorithm

Our atlas of 46 DDI subjects registered is now used to obtain an average DDI model using the MCM interpolation framework. The tractography is thus estimated on this average model as follows:

- A masked of the average DDI model is computed as the intersection of the registered masks of the 46 original DDI models.

- Seeds are placed on each voxel on the entire masked image.

- For each seed in the image, a tract, i.e a sequence of spatial position, is estimated. The entire tractography is composed by the union of all these tracts.

There are several methods to perform the estimation of a tract from one seed. The final tractography highly depends of the algorithm type (deterministic or probabilistic) and the stop conditions of the fiber tract. Our deterministic algorithm for MCM is an extension to MCM of the usual FACT tractography [Mori 1999]:

For a current point n and a previous point $n-1$ in a sub-tract with their corresponding spatial positions P_n and P_{n-1}, do:

1. Estimate the model $\mathcal{M}_n$ at the current position P_n using the MCM interpolation scheme (see Chapter 5)

2. Compute the current direction from the spatial locations:

$$D_n = \frac{P_n - P_{n-1}}{||P_n - P_{n-1}||} \tag{6.15}$$

3. We note $\{O^i_{\mathcal{M}_n}\}_{i=1,..,p}$ the orientation of the p anisotropic compartments of $\mathcal{M}_n$. Then, the closest orientation $O^m_{\mathcal{M}_n}$ compared to the current direction is selected:

$$m = \underset{t\in[1,...,p]}{\arg\max} \ | < D_n, O^t_{\mathcal{M}_n} > | \tag{6.16}$$

$O^m_{\mathcal{M}_n}$ is now considered to be the selected direction, i.e the one that is the closest to the current direction. For more regularity, the next direction is computed as a weighted sum of the current direction and the selected direction:

$$D_{n+1} = W(r)O^m_{\mathcal{M}_n} + (1 - W(r))D_n \tag{6.17}$$

where D_{n+1} is the next direction and $W(r)$ is a weight balancing the selected $O^m_{\mathcal{M}_n}$ and the previous direction to make the fiber smoother.

4. The next direction is added to the current position to give the next position:

$$P_{n+1} = P_n + sD_{n+1} \tag{6.18}$$

where s is a scalar step that involves the velocity of the fiber progression. In our algorithm s is set to 1 mm.

6.5.3.2 Implementation details

Each tract from one seed is composed by two sub-tracts: one forward and one backward. They are computed separately and finally regrouped. For the first position, D_1, the orientation of the main anisotropic compartment is taken, i.e the one with the largest weight within $\mathcal{M}_1$. Both directions correspond to the anisotropic compartment orientation, one is used to initialize the forward sub-tract, the other to initialize the backward sub-tract.

Optionally, it is possible to add the compartment weight (or a function of it) in front of the dot product Eq 6.16 to give more importance to "heavy" compartments. The weight used to smooth the fiber is expressed as:

$$W(r) = (1 - r)\mathrm{FA}(O^m_{\mathcal{M}_n}) + r \tag{6.19}$$

where $\mathrm{FA}(O^m_{\mathcal{M}_n})$ is the FA of the selected direction $O^m_{\mathcal{M}_n}$ and $r \in [0, 1]$ is a minimal weight attributed to the new direction. For $r = 1$, the next direction is the selected direction and the previous direction is not taken into account. For $r = 0$, the weight of the selected compartment corresponds to its FA value. Therefore, a very anisotropic compartment has more value than an isotropic one in the computation of the next direction. In our algorithm, $r = 0.25$ is chosen, giving some significance to the previous direction and, hence, some smoothness to the tract.

The tract progresses until one stop condition is reached. There are various possibilities of stop conditions and the parameters chosen highly influence the final result. In this tractography, we use as stop conditions:

- The point needs to belong to the brain mask.
- The maximum tract angle between two following directions is 60 degrees.
- The maximum length of a tract is 150 mm, i.e when the maximum is reached, the fiber tract stops.
- The minimum length of a tract is 10 mm, i.e tracts shorter than 10 mm are not considered in the final tractography.
- The tract is stopped for a total weight of isotropic compartments up to 0.8. This is explained by the incertitude regarding the selection of an anisotropic compartment with low weight.

This algorithm is applied to the average DDI of our atlas. This results in a tractography adapted to perform statistics on the entire atlas and for all patients.

6.5.4 Results

From the average MCM tractography $\mathcal{T}$, we compute statistics for several parameters: compartment AD, MD and FA. Two subsets are extracted from the whole brain tractography: the left and the right corticospinal tract (CST). These tracts are chosen for a patient with lesions on the left CST and no lesion on the right CST. The patient is the one illustrated in the voxel-based approach on Fig 6.1 and Fig 6.2.

The results are presented for three parameters, one figure per parameter: AD in Fig 6.4, MD in Fig 6.5 and in FA Fig 6.6. For each figure, the first line corresponds to the left CST and the second line to the right CST. From left to right these figures show: the patient parameter value, the average parameter value computed from the entire atlas, the p-value range between 0 and 0.25 superimposed with a lesion manual segmentation.

These figures show visually the ability of the AD and MD parameters to characterize a lesion within the brain. Both measures present a reasonable number of false positive areas. The FA does not seem to be an adapted measure on this image.

Normally, DTI MD within a MS lesion is supposed to be higher than for normal WM tissues [Filippi 2000]. In this example, the change of the DTI MD is contained, in the DDI model, in the weight of the free water compartment (see Fig 6.1). Hence, the AD within the anisotropic compartments decrease and so does the MD. This may correspond to a physical reality. If the myelin and WM bounds are damaged, the water is less trapped within the axons and thus can hit glial cells interrupting its axial diffusion. However, this kind of interpretation needs to be taken with high caution, considering the difficulty to understand the microstructure process. What is sure is that DTI MD entangles everything and DDI separates information which is in itself interesting.

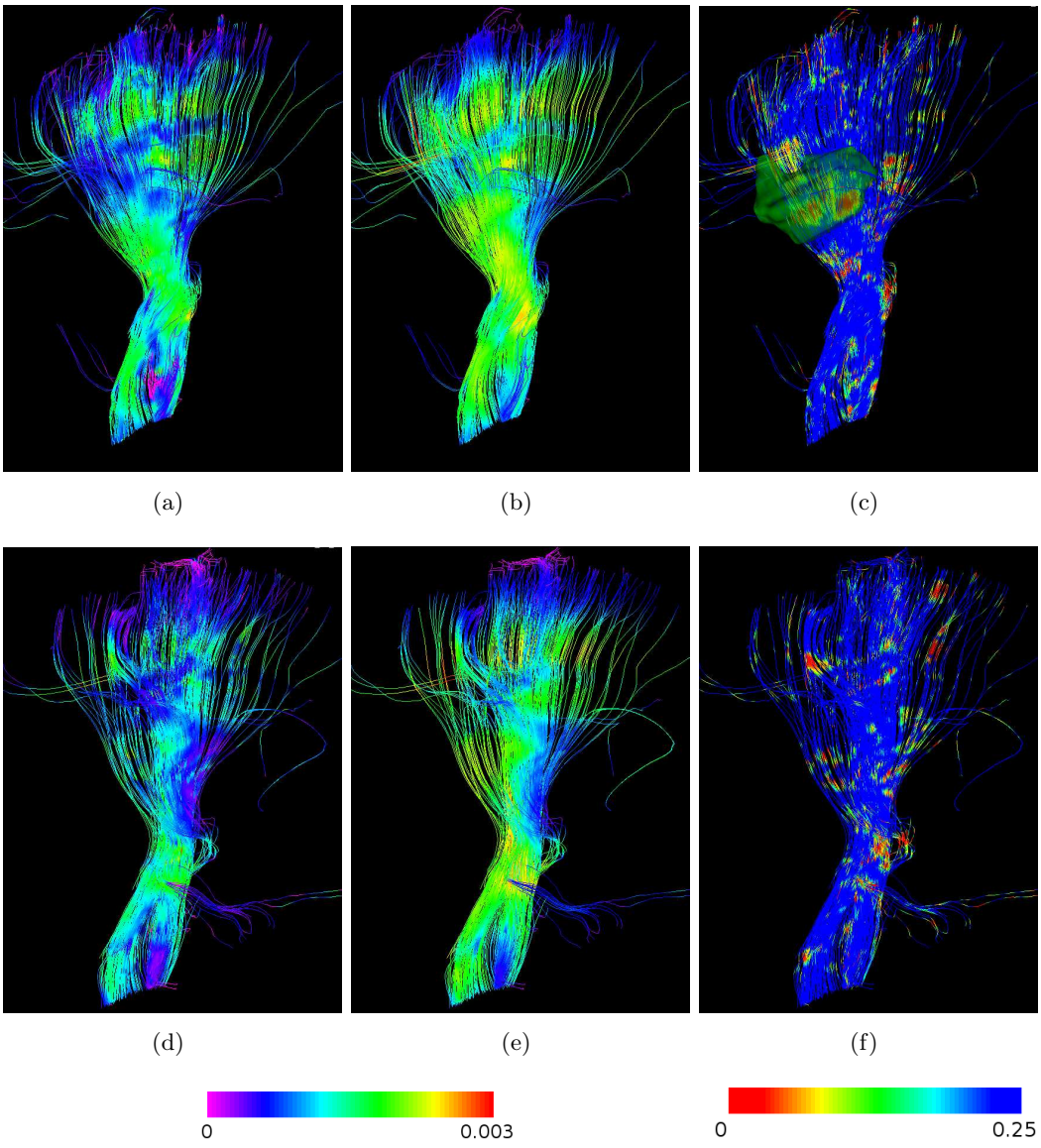

Figure 6.4: Compartment axial diffusivity study. First line: left CST, second line: right CST. The first column is the patient AD value and the second column the AD average value computed from the entire atlas. The corresponding scalar bar is low the two first columns and represents the diffusivity in $mm^2.s^{-1}$. The last column corresponds to the p-value rescaled between 0 and 0.25 (all values above 0.25 are put to 0.25). On the first line the green 3D volume represents a 3D lesion segmented manually on the T2-weighted image (see Fig 6.2). On the first line within the left CST, the AD value is lower on the patient than the average within the lesion leading to a significant difference in a large part of the lesion. On the second line the AD seems also lower for the patient than the average. These results are less significant according to the p-value, however there are still some small false positive area.

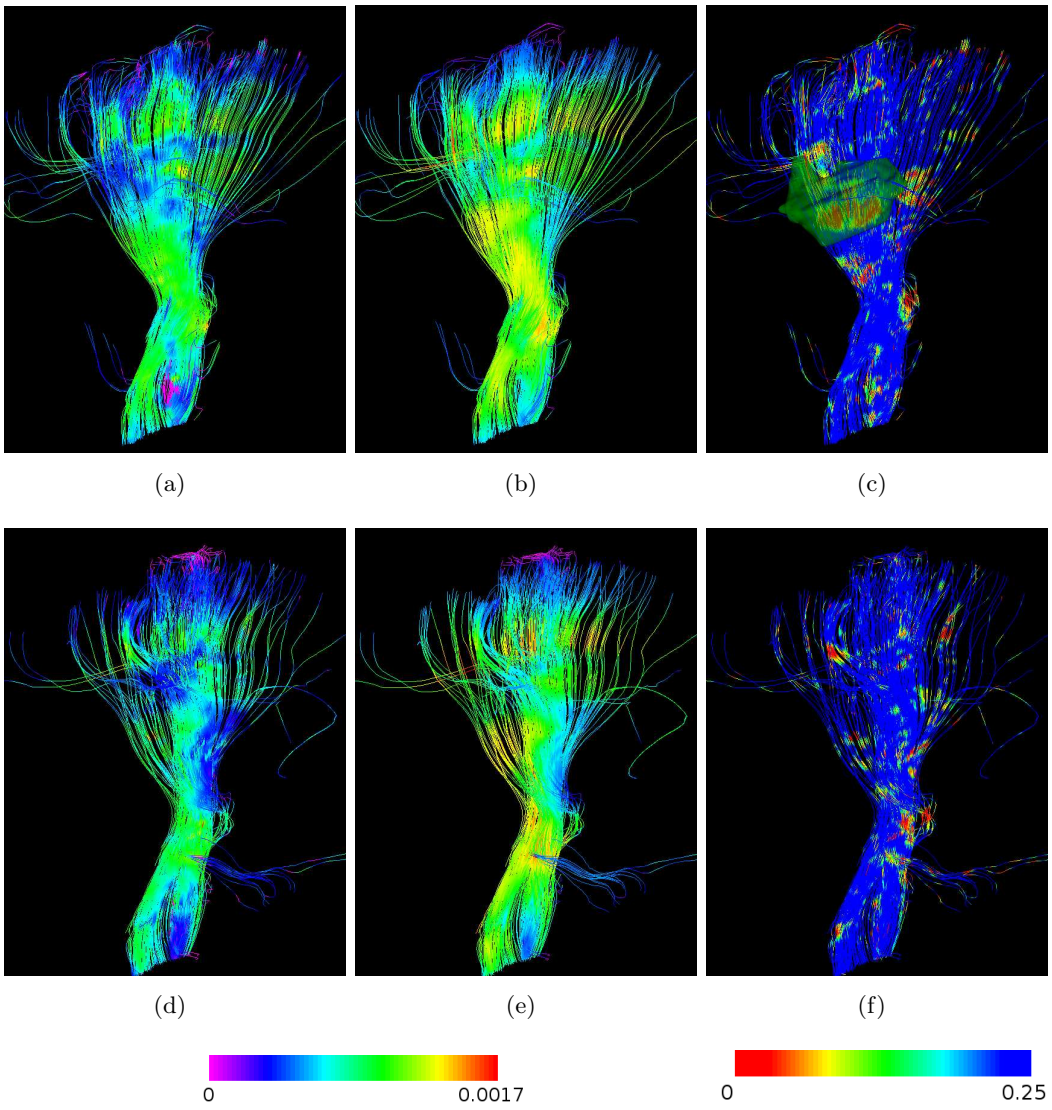

Figure 6.5: Compartment mean diffusivity study. First line: left CST, second line: right CST. The first column is the patient MD value and the second column the MD average value computed from the entire atlas. The corresponding scalar bar is low the two first columns and represents the diffusivity in $mm^2.s^{-1}$. The last column corresponds to the p-value rescaled between 0 and 0.25 (all values above 0.25 are put to 0.25). On the first line the green 3D volume represents a 3D lesion segmented manually on the T2-weighted image (see Fig 6.2). These results seem highly similar compared to the AD (see Fig 6.4). However the lesion comports more significant with the MD measure than with the AD measure.

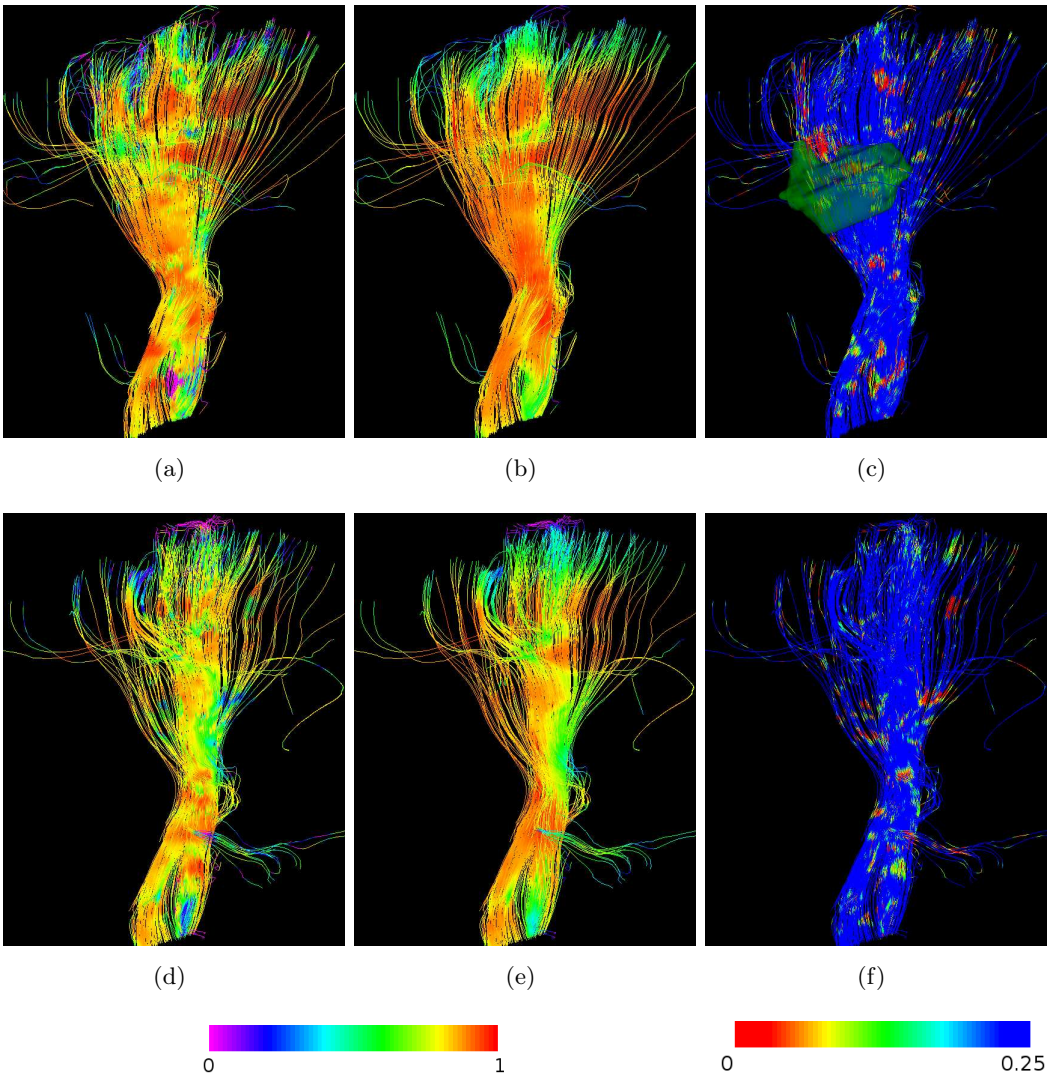

Figure 6.6: Compartment fractional anisotropy study. First line: left CST, second line: right CST. The first column is the patient FA value and the second column the FA average value computed from the entire atlas. The corresponding scalar bar is low the two first columns and represents the diffusivity in $mm^2.s^{-1}$. The last column corresponds to the p-value rescaled between 0 and 0.25 (all values above 0.25 are put to 0.25). On the first line the green 3D volume represents a 3D lesion segmented manually on the T2-weighted image (see Fig 6.2). Contrary to the AD and MD measures, the FA is not able to recover the major part of the lesion. However, interestingly, the measure seems almost complementary to the AD and MD measure.

6.6 Conclusion

In this chapter, we have presented two different approaches to perform statistics using MCM. The USPIO dataset contains both control subjects and patients suffering from MS. From 46 controls, we first computed a DDI atlas using the MCM interpolation framework presented in Chapter 5. We introduced specific parameters computed from the DDI anisotropic compartment and modalities to perform statistics from a set of measures. Then we proposed two different approaches: one voxel-based and one tract-based.

For the voxel-based method, we presented several scalar maps from both DDI and DTI models. The z-score shows the ability of the DDI free water compartment weight to characterize MS lesions for two patients, as well as the classical MD from the DTI. The other scalar measures, coming from anisotropic compartments average, seem less adapted to this kind of voxel-based measure.

To better use the MCM specificity, we have proposed a deterministic MCM tractography. From a tractography computed on the average DDI, we then computed statistics on tracts. The AD and MD, extracted from the anisotropic compartment, have an inverse behavior compared to the AD and MD computed from the DTI model at the voxel level. However, they appear to be relevant biomarkers with high p-value significance within a lesion. On the right CST, there are no lesions for the patient. Yet, the AD and the MD of the patient seem to be globally lower than the average control, although this trend is not statistically significant. That might be explained by difference between normal-appearing white matter (NAWM) diffusion between patient and control subjects [Wiest-Daesslé 2009]. As a future work, we can study this assumption with a patient population versus control population statistical test.

We demonstrated the possibility to perform statistics on MCMs at both the voxel level and the tract level. The parameters extracted from the DDI are complementary to the ones extracted from the DTI. However, the compartments separation offers a possible microstructure explanation contrary to the scalars from DTI that can lead to inaccurate interpretation. Behind this proof of concept, a lot of experiments can be done. This work can be extended to more patient or other diseases. It is also possible to compute a quantitative score (as a dice score) to estimate the performance of the model and use it to compare several models.

Chapter 7

Conclusion

Contents

7.1 Contributions summary

This manuscript has presented contributions to dMRI processing tools, in particular MCM. Several preprocessing steps are necessary before the exploitation of DWI acquisitions. With the goal of the clinical use of complicated models such as MCM, a lot of research studies are indeed necessary to evaluate prospective benefits. To perform quantitative evaluation, we need to be able to compute statistics on data and thus create an atlas, register MCM and more. In the following, we summarize the major contributions of this thesis. All the processing methods proposed have been integrated in our team code Anima. This open software is available on line with the corresponding documentation[1].

7.1.1 Distortion correction of EPI

The dMRI needs ultra fast acquisition modalities as echo planar imaging (EPI) that are corrupted by artifacts. To better exploit the diffusion model resulting from these DWI, preprocessing steps need to be performed. EPI suffers from large distortions mainly at the air/bone interfaces. We have proposed a new registration method to correct these distortions. This method uses b_0 images with opposite phase encoding direction (PED), the acquisition of such an extra image not being time consuming. The registration is based on a new BM algorithm specifically adapted to the distortion model.

[1] https://github.com/Inria-Visages/Anima-Public

The BM method has been tested on *in vivo* data. A quantitative evaluation performs on two pair of images with opposite PEDs show high similarity between the corrected images.

This work leads to several publications including one oral presentation at a peer reviewed international conference and one peer-reviewed international journal:

- **Journal article**
  Block-Matching Distortion Correction of Echo-Planar Images With Opposite Phase Encoding Directions
  Renaud Hédouin, Olivier Commowick, Elise Bannier, Benoit Scherrer, Maxime Taquet, Simon Warfield, Christian Barillot
  IEEE Transactions on Medical Imaging, Institute of Electrical and Electronics Engineers, May 2017, 36(5):1106-1115. doi: 10.1109/TMI.2016.2646920

- **Conference papers: Oral presentation**
  Symmetric Block-Matching Registration for the Distortion Correction of Echo-Planar Images
  Renaud Hédouin, Olivier Commowick, Maxime Taquet, Elise Bannier, Benoit Scherrer, Simon Warfield, Christian Barillot
  IEEE International Symposium on Biomedical Imaging (ISBI), Apr 2015, New York, United States. pp.717-720, 2015

- **Poster communication**
  Symmetric Block-Matching Registration for the Distortion Correction of Echo-Planar Images
  Renaud Hedouin, Olivier Commowick, Elise Bannier, Christian Barillot
  ESMRMB, Oct 2015, Edinburgh, United Kingdom. 2015

7.1.2 MCM interpolation

The interpolation of images is a prerequisite to perform many of classical processing steps: averaging, registration, atlas creation. A large number of algorithms perform interpolation on scalar data and interpolate each DWI individually. However it is better to directly work on the diffusion models and thus use an MCM interpolation scheme.

We have proposed such a general framework viewed as a simplification problem based on spectral clustering. This method is adaptable to any MCM as long as a weighted average and pseudo-distance between anisotropic compartments can be provided. We tested our interpolation scheme for two particular MCM: the DDI and the MTM. The MTM offers nice visual images while the analytic DDI anisotropic compartment average computation provides good quantitative results.

This work has been presented at the peer reviewed international conference MICCAI in Munich 2015:

- **Conference papers**
  Interpolation and Averaging of Multi-Compartment Model Images

Renaud Hédouin, Olivier Commowick, Aymeric Stamm, Christian Barillot
18th International Conference on Medical Image Computing and Computer Assisted Intervention (MICCAI), Oct 2015, Munich, Germany. 9350, pp.354-362, 2015

7.1.3 From MCM to statistics

We have presented a statistical framework on a dataset of patients suffering from MS at an early stage. From this dataset, DTI and DDI models were estimated. We detailed the construction of a DDI atlas using the MCM interpolation framework presented in Chapter 5. Statistics including z-scores and p-values have been computed from the parameters extracted from the DDI free water and anisotropic compartments as well as classic MD and FA DTI parameters.

Two different approaches were proposed to compute statistics: one voxel-based and one tract-based. With the voxel-based, the weight of the free water compartment z-score highlights lesions on several visual examples showing the interest of such a method to separate isotropic and anisotropic compartments. For the tract-based approach, a tractography algorithm adapted to MCM was specifically designed. Results show a decrease of AD and MD extracted from a single anisotropic compartment within lesions. Visual examples with p-value were presented to illustrate this behavior. This proof of concept demonstrates the interest of MCMs to characterize MS lesions showing a better and easier interpretability than with parameters extracted from DTI and offers the possibility of longitudinal studies.

7.2 Perspectives

7.2.1 Methodological perspectives

In dMRI, the distortion artifacts of the EPI acquisition are a major problem. It will become worse with stronger scanner magnetic fields. Hence, the correction of these artifacts stays an open problem. In addition to DWI acquisitions with one or several PED, a structural image is generally acquired in a classical MRI exam. The use of a structural image as a reference to correct distortion has already been proposed [Irfanoglu 2015]. Our new block-matching algorithm currently takes two b_0 images with opposite PED. Therefore, we want to adapt this method to an additional undistorted image as a reference for improved correction.

Such a block-matching with three images instead of two would be an innovation to our knowledge. This framework offers a well-adapted multiple correlation metric with a structural image as a target variable. Unfortunately, the T2-weighted image presents more details than the b_0 images in some brain areas and thus the block-matching is corrupted in these areas. We have not currently handled these issues, however this method offers promising results. We can try to adapt a specific brain mask to this task to remove unwanted extra information from the T2-weighted image. An additional specific weight could also be added to treat this issue. Other

similarity measures are also an option to penalize areas where the two b_o images with reversed PED do not match and thus recover the best of classic and multiple correlation BM. Last but not least a non-distorted structural image more similar to a b_0 image could be provided with new MRI sequences such as the readout-segmented EPI [Holdsworth 2008, Porter 2009]. This BM extension constitutes a major perspective of this thesis that we started to explore rapidly as shown in Section 4.6.

Behind the preprocessing steps, various works can be done directly on diffusion models. First, we have proposed a method to interpolate MCM. This framework was developed for two anisotropic compartment types: tensor and DDI. However, the method is very generic and can be extended to any anisotropic compartment modeling. Hence the use of this interpolation framework can be extended with specific metrics for other classical anisotropic compartments such as NODDI or CHARMED.

These interpolation tools can be used to create an atlas and then compute statistic on patient and control populations. The MCM atlas is made through several steps:

1. DTI and MCM are estimated from the original DWI.

2. The DTI atlas is created following Section 6.2.2 using a specific DTI registration technique.

3. The transformations used for the DTI atlas are applied to the MCM using the interpolation framework to create a MCM atlas.

It is better to use DTI to register models than a registration on T1-weighted images applied to the tensors [Ruiz-Alzola 2002b]. However, it would be even better to do the registration directly on MCM and perform the entire pipeline with the MCMs to be more coherent and obtain more accurate registration. Thus, a generic MCM registration method is a natural extension of the interpolation framework proposed in Chapter 5, where only a new MCM based similarity metric needs to be defined.

These preprocessing steps allow to compute statistics from a dataset. In Chapter 6, we have presented some results from the USPIO database that concerns patients suffering from early stage MS. This evaluation could be extended with quantitative results on the entire database and comparison with other diffusion models. Moreover, the two statistical approaches, voxel-based and tract-based, can be applied to other diseases such as Alzheimer's disease, traumatic brain injury, brain tumors...

Previous propositions are natural evolutions of the work presented in this thesis. However, more general considerations about dMRI can also be studied. The dMRI is blind to myelin due to the short T2 relaxation time of the water within the myelin [Brunberg 1995]. Other MRI modalities such as relaxometry can detect and quantify the myelin sheath. The ratio between the axon diameter, known as g-ratio, and the axon with its myelin sheath diameter is a known biomarker from particular diseases [Stikov 2011]. MS damages indeed in majority the myelin sheath and the

demyelination causes important change in this ratio. Hence, a combination of dMRI and relaxometry could offer useful information to compute this kind of biomarker on a compartment basis.

7.2.2 Clinical perspectives

Nowadays, dMRI is a routine process in clinic to diagnose several brain diseases. Generally a DWI sequence is made of 3 different gradient directions and a b_0 image to compute a MD scalar map. Recently, the Observatoire français de la sclérose en plaques (OFSEP), that studies MS, recommended to acquire at least 6 different gradient directions and one b_0 that allows to estimate a DTI [Cotton 2015]. Thus the standard protocol (i.e, not in clinic research) does not offer the possibility to estimate a MCM. Therefore, there is a challenge to transfer MCM from pure research to clinical applications. A MCM, in clinical research, is estimated with at least 30 gradient directions and many MCMs need more than one b-value shell. Therefore, the acquisition time is a central problem for a routine clinical use. In this domain that goes beyond the topic of this thesis, many recent developments (specific sequences such as CUSP [Scherrer 2012], compressed sensing, multi-band acquisitions) are very promising. As a future work, we can study how these fast and multi-shell sequences can be useful for computing more precise biomarkers in the clinics.

In addition to this consideration, MCM has to provide intelligible information easy to interpret for the medical corpus. To convince radiologists of the interest of MCMs, solid studies that related diffusion models to the ground truth are also required. One way to do that is to practice dissections or biopsy on animals. An interesting database of dMRI and histology towards such a validation was proposed in 2017 at International Society for Magnetic Resonance in Medicine (ISMRM) and will be of great interest for relating specific MCM parameters to tissue damage[2]. Elaborated diffusion models can be the future of dMRI provided that we are able to explain and prove their interest in an improved comprehension of brain diseases.

[2] doi.org/10.17605/OSF.IO/YP4QG

Acronyms

AIC akaike information criterion . . . 81
AD axial diffusivity . . . 23
ADC Apparent Diffusion Coefficient . . . 15
ALS amyotrophic lateral sclerosis . . . 13
AP anterior-posterior . . . 41
BM block-matching . . . 8
CEA commissariat a l'energie atomique . . . 48
CHARMED Composite Hindered And Restricted Model of Diffusion . . . 38
CIS clinically isolated syndromes . . . 87
CFA color fractional anisotropy . . . 54
CNS central nervous system . . . 6
CSF cerebrospinal fluid . . . 24
CST corticospinal tract . . . 97
CT computed tomography . . . 5
CUSP cube and sphere
DDI diffusion direction imaging . . . 8
dMRI diffusion MRI . . . 6
DSI diffusion spectrum imaging . . . 20
DTI diffusion tensor imaging
DWI diffusion-weighted magnetic resonance imaging
EAP ensemble average propagator . . . 20
EEG electroencephalography . . . 14
EPI echo planar imaging . . . 7
FA fractional anisotropy . . . 24
FDA food and drug administration . . . 5
FLAIR Fluid-attenuated inversion recovery
fMRI functional MRI . . . 7
GCC generalized squared correlation coefficient . . . 87
GM grey matter . . . 11
HARDI high-angular-resolution diffusion imaging
HCP Human Connectome Project . . . 34

ISMRM International Society for Magnetic Resonance in Medicine 107
LR left-right 41
MCM multi-compartment model iii
MD mean diffusivity 20
MDD major depressive disorder 24
mq-DPI multiple q-shell diffusion propagator imaging 33
MRI magnetic resonance imaging
MS multiple sclerosis 13
MTM multi-tensor model 8
NAWM normal-appearing white matter 101
NODDI neurite orientation dispersion and density imaging 34
NLM non-local means 88
NMR nuclear magnetic resonance 5
OCD obsessive-compulsive disorder 24
ODF orientation distribution functions 32
OECD Organisation for Economic Co-operation and Development
OFSEP Observatoire français de la sclérose en plaques 107
PA posterior-anterior 41
PCA principal component analysis
PDF probability density function 20
PED phase encoding direction 7
PET positron emission tomography 13
PGSE pulse gradient spin echo 19
PNS peripheric nervous system 9
PTSD posttraumatic stress disorder 13
PSF point spread functions 40
RD radial diffusivity 23
ROI region of interest 83
RTO return-to-origin 33
RF radiofrequency 17
RL right-left 41
SH spherical harmonics 31
SPF spherical polar Fourier 33
SVF stationary velocity field 43

Bibliography

[Ahn 1986] CB Ahn, JH Kim and ZH Cho. *High-speed spiral-scan echo planar NMR imaging-I.* IEEE transactions on medical imaging, vol. 5, no. 1, pages 2–7, 1986. (Cited on page 21.)

[Akai 2005] Hiroyuki Akai, Harushi Mori, Shigeki Aoki, Yoshitaka Masutani, Nobutaka Kawahara, Jyunichi Shibahara and Kuni Ohtomo. *Diffusion tensor tractography of gliomatosis cerebri: fiber tracking through the tumor.* Journal of computer assisted tomography, vol. 29, no. 1, pages 127–129, 2005. (Cited on page 92.)

[Alexa 2002] Marc Alexa. *Linear combination of transformations.* In ACM Transactions on Graphics (TOG), volume 21, pages 380–387. ACM, 2002. (Cited on page 45.)

[Alexander 2010] Daniel C Alexander, Penny L Hubbard, Matt G Hall, Elizabeth A Moore, Maurice Ptito, Geoff JM Parker and Tim B Dyrby. *Orientationally invariant indices of axon diameter and density from diffusion MRI.* Neuroimage, vol. 52, no. 4, pages 1374–1389, 2010. (Cited on page 34.)

[Amari 2007] Shun-ichi Amari and Hiroshi Nagaoka. Methods of information geometry, volume 191. American Mathematical Soc., 2007. (Cited on pages 27 and 72.)

[Andersson 2003] Jesper LR Andersson, Stefan Skare and John Ashburner. *How to correct susceptibility distortions in spin-echo echo-planar images: application to diffusion tensor imaging.* Neuroimage, vol. 20, no. 2, pages 870–888, 2003. (Cited on pages 40, 42 and 50.)

[Arsigny 2006] Vincent Arsigny, Pierre Fillard, Xavier Pennec and Nicholas Ayache. *Log-Euclidean metrics for fast and simple calculus on diffusion tensors.* MRM, vol. 56, no. 2, pages 411–421, 2006. (Cited on pages 29 and 30.)

[Arsigny 2009] Vincent Arsigny, Olivier Commowick, Nicholas Ayache and Xavier Pennec. *A fast and log-euclidean polyaffine framework for locally linear registration.* Journal of Mathematical Imaging and Vision, vol. 33, no. 2, pages 222–238, 2009. (Cited on pages 45, 47 and 48.)

[Ascherio 2007] Alberto Ascherio and Kassandra L Munger. *Environmental risk factors for multiple sclerosis. Part I: the role of infection.* Annals of neurology, vol. 61, no. 4, pages 288–299, 2007. (Cited on page 13.)

[Assaf 2004] Yaniv Assaf, Raisa Z Freidlin, Gustavo K Rohde and Peter J Basser. *New modeling and experimental framework to characterize hindered and restricted water diffusion in brain white matter.* Magnetic Resonance in Medicine, vol. 52, no. 5, pages 965–978, 2004. (Cited on pages 35 and 38.)

[Assaf 2005] Yaniv Assaf and Peter J Basser. *Composite hindered and restricted model of diffusion (CHARMED) MR imaging of the human brain.* Neuroimage, vol. 27, no. 1, pages 48–58, 2005. (Cited on page 38.)

[Assaf 2008] Yaniv Assaf, Tamar Blumenfeld-Katzir, Yossi Yovel and Peter J Basser. *AxCaliber: a method for measuring axon diameter distribution from diffusion MRI.* Magnetic resonance in medicine, vol. 59, no. 6, pages 1347–1354, 2008. (Cited on page 38.)

[Assemlal 2009] Haz-Edine Assemlal, David Tschumperlé and Luc Brun. *Efficient and robust computation of PDF features from diffusion MR signal.* Medical image analysis, vol. 13, no. 5, pages 715–729, 2009. (Cited on page 33.)

[Atkinson 2012] Kendall Atkinson and Weimin Han. Spherical harmonics and approximations on the unit sphere: an introduction, volume 2044. Springer Science & Business Media, 2012. (Cited on page 31.)

[Avants 2008] Brian B Avants, Charles L Epstein, Murray Grossman and James C Gee. *Symmetric diffeomorphic image registration with cross-correlation: evaluating automated labeling of elderly and neurodegenerative brain.* Medical image analysis, vol. 12, no. 1, pages 26–41, 2008. (Cited on page 42.)

[Banerjee 2005] Arindam Banerjee, Inderjit S Dhillon, Joydeep Ghosh and Suvrit Sra. *Clustering on the unit hypersphere using von Mises-Fisher distributions.* Journal of Machine Learning Research, vol. 6, no. Sep, pages 1345–1382, 2005. (Cited on page 68.)

[Barkhof 1997] Frederik Barkhof, Massimo Filippi, David H Miller, Philip Scheltens, Adriana Campi, Chris H Polman, Giancarlo Comi, Herman J Ader, Nick Losseff and Jacob Valk. *Comparison of MRI criteria at first presentation to predict conversion to clinically definite multiple sclerosis.* Brain, vol. 120, no. 11, pages 2059–2069, 1997. (Cited on page 13.)

[Barmpoutis 2007] Angelos Barmpoutis, Baba C Vemuri and John R Forder. *Registration of high angular resolution diffusion MRI images using 4th order tensors.* In MICCAI, pages 908–915. 2007. (Cited on page 62.)

[Basser 1994] Peter J Basser, James Mattiello and Denis LeBihan. *Estimation of the effective self-diffusion tensor from the NMR spin echo.* Journal of Magnetic Resonance, Series B, vol. 103, no. 3, pages 247–254, 1994. (Cited on page 23.)

[Basser 1996] Peter J. Basser and Carlo Pierpaoli. *Microstructural and Physiological Features of Tissues Elucidated by Quantitative Diffusion-Tensor MRI.* Journal of Magnetic Resonance, Series B, vol. 111, no. 3, pages 209 – 219, 1996. (Cited on page 61.)

[Basser 2000] Peter J Basser and Sinisa Pajevic. *Statistical artifacts in diffusion tensor MRI (DT-MRI) caused by background noise.* Magnetic Resonance in Medicine, vol. 44, no. 1, pages 41–50, 2000. (Cited on page 22.)

[Batchelor 2005] PG Batchelor, M Moakher, D Atkinson, F Calamante and A Connelly. *A rigorous framework for diffusion tensor calculus.* Magnetic Resonance in Medicine, vol. 53, no. 1, pages 221–225, 2005. (Cited on page 25.)

[Beaulieu 2002] Christian Beaulieu. *The basis of anisotropic water diffusion in the nervous system–a technical review.* NMR in Biomedicine, vol. 15, no. 7-8, pages 435–455, 2002. (Cited on page 36.)

[Beg 2006] Mirza Faisal Beg and Ali Khan. *Computing an average anatomical atlas using LDDMM and geodesic shooting.* In Biomedical Imaging: Nano to Macro, 2006. 3rd IEEE International Symposium on, pages 1116–1119. IEEE, 2006. (Cited on page 84.)

[Behrens 2003] Timothy EJ Behrens, MW Woolrich, Mark Jenkinson, H Johansen-Berg, RG Nunes, S Clare, PM Matthews, J Michael Brady and Stephen M Smith. *Characterization and propagation of uncertainty in diffusion-weighted MR imaging.* Magnetic resonance in medicine, vol. 50, no. 5, pages 1077–1088, 2003. (Cited on pages 36 and 37.)

[Berman 2009] Jeffrey Berman. *Diffusion MR tractography as a tool for surgical planning.* Magnetic resonance imaging clinics of North America, vol. 17, no. 2, pages 205–214, 2009. (Cited on page 92.)

[Bezdek 1984] James C Bezdek, Robert Ehrlich and William Full. *FCM: The fuzzy c-means clustering algorithm.* Computers & Geosciences, vol. 10, no. 2-3, pages 191–203, 1984. (Cited on page 65.)

[Bilgic 2012] Berkin Bilgic, Kawin Setsompop, Julien Cohen-Adad, Anastasia Yendiki, Lawrence L Wald and Elfar Adalsteinsson. *Accelerated diffusion spectrum imaging with compressed sensing using adaptive dictionaries.* Magnetic Resonance in Medicine, vol. 68, no. 6, pages 1747–1754, 2012. (Cited on page 33.)

[Bloch 1946] Felix Bloch. *Nuclear induction.* Physical review, vol. 70, no. 7-8, page 460, 1946. (Cited on page 14.)

[Bodammer 2004] Nils Bodammer, Jörn Kaufmann, Martin Kanowski and Claus Tempelmann. *Eddy current correction in diffusion-weighted imaging using pairs of images acquired with opposite diffusion gradient polarity.* Magnetic Resonance in Medicine, vol. 51, no. 1, pages 188–193, 2004. (Cited on page 22.)

[Bonkowsky 2010] Joshua Leitch Bonkowsky, C Nelson, JL Kingston, FM Filloux, MB Mundorff and Rajendu Srivastava. *The burden of inherited leukodystrophies in children.* Neurology, vol. 75, no. 8, pages 718–725, 2010. (Cited on page 13.)

[Boorstin 1985] Daniel J Boorstin. The dicsoverers: A history of man's search to know his world and himself. Paperback, 1985. (Cited on page 14.)

[Boothby 1986] William M Boothby. An introduction to differentiable manifolds and riemannian geometry, volume 120. Academic press, 1986. (Cited on page 26.)

[Bowtell 1994] R Bowtell, DJO McIntyre, MJ Commandre, PM Glover and P Mansfield. *Correction of geometric distortion in echo planar images.* In Soc. Magn. Res. Abstr, volume 2, page 411, 1994. (Cited on page 40.)

[Bracewell 1986] Ronald Newbold Bracewell and Ronald N Bracewell. The fourier transform and its applications, volume 31999. McGraw-Hill New York, 1986. (Cited on page 30.)

[Bradley 1998] Paul S Bradley and Usama M Fayyad. *Refining Initial Points for K-Means Clustering.* In ICML, volume 98, pages 91–99. Citeseer, 1998. (Cited on page 65.)

[Brex 2002] Peter A Brex, Olga Ciccarelli, Jonathon I O'riordan, Michael Sailer, Alan J Thompson and David H Miller. *A longitudinal study of abnormalities on MRI and disability from multiple sclerosis.* New England Journal of Medicine, vol. 346, no. 3, pages 158–164, 2002. (Cited on page 13.)

[Brown 1828] Robert Brown. *XXVII. A brief account of microscopical observations made in the months of June, July and August 1827, on the particles contained in the pollen of plants; and on the general existence of active molecules in organic and inorganic bodies.* Philosophical Magazine Series 2, vol. 4, no. 21, pages 161–173, 1828. (Cited on page 16.)

[Brozek 1961] Josef Brozek and Austin Henschel. *Techniques for measuring body composition.* In Conference on Techniques for Measuring Body Composition (1959: Natick, Mass.). National Academy of Sciences-National Research Council, 1961. (Cited on pages 1 and 5.)

[Brunberg 1995] James A Brunberg, Thomas L Chenevert, PE McKeever, Donald A Ross, Larry R Junck, Karin M Muraszko, Robert Dauser, James G Pipe and AT Betley. *In vivo MR determination of water diffusion coefficients and diffusion anisotropy: correlation with structural alteration in gliomas of the cerebral hemispheres.* American Journal of Neuroradiology, vol. 16, no. 2, pages 361–371, 1995. (Cited on pages 36 and 106.)

[Budde 2009] Matthew D Budde, Mingqiang Xie, Anne H Cross and Sheng-Kwei Song. *Axial diffusivity is the primary correlate of axonal injury in the experimental autoimmune encephalomyelitis spinal cord: a quantitative pixelwise analysis.* Journal of Neuroscience, vol. 29, no. 9, pages 2805–2813, 2009. (Cited on page 24.)

[Burt 1983] Peter J Burt and Edward H Adelson. *The Laplacian pyramid as a compact image code.* Communications, IEEE Transactions on, vol. 31, no. 4, pages 532–540, 1983. (Cited on page 43.)

[Cabezas 2011] Mariano Cabezas, Arnau Oliver, Xavier Lladó, Jordi Freixenet and Meritxell Bach Cuadra. *A review of atlas-based segmentation for magnetic resonance brain images.* Computer methods and programs in biomedicine, vol. 104, no. 3, pages e158–e177, 2011. (Cited on page 84.)

[Calvo 2001] E Calvo, I Palacios, E Delgado, J Ruiz-Cabello, P Hernandez, O Sanchez-Pernaute, J Egido and G Herrero-Beaumont. *High-resolution MRI detects cartilage swelling at the early stages of experimental osteoarthritis.* Osteoarthritis and Cartilage, vol. 9, no. 5, pages 463–472, 2001. (Cited on pages 2 and 6.)

[Carr 1954] Herman Y Carr and Edward M Purcell. *Effects of diffusion on free precession in nuclear magnetic resonance experiments.* Physical review, vol. 94, no. 3, page 630, 1954. (Cited on page 15.)

[Caruyer 2012] Emmanuel Caruyer and Rachid Deriche. *Diffusion MRI signal reconstruction with continuity constraint and optimal regularization.* Medical image analysis, vol. 16, no. 6, pages 1113–1120, 2012. (Cited on page 33.)

[Chamberland 2014] Maxime Chamberland, Kevin Whittingstall, David Fortin, David Mathieu and Maxime Descoteaux. *Real-time multi-peak tractography for instantaneous connectivity display.* Frontiers in neuroinformatics, vol. 8, page 59, 2014. (Cited on page 92.)

[Chandrasekhar 1943] Subrahmanyan Chandrasekhar. *Stochastic problems in physics and astronomy.* Reviews of modern physics, vol. 15, no. 1, page 1, 1943. (Cited on page 16.)

[Chang 1992] Hsuan Chang and J Michael Fitzpatrick. *A technique for accurate magnetic resonance imaging in the presence of field inhomogeneities.* IEEE Transactions on medical imaging, vol. 11, no. 3, pages 319–329, 1992. (Cited on page 40.)

[Chang 2005] Lin-Ching Chang, Derek K Jones and Carlo Pierpaoli. *RESTORE: robust estimation of tensors by outlier rejection.* Magnetic resonance in medicine, vol. 53, no. 5, pages 1088–1095, 2005. (Cited on page 23.)

[Chaudhuri 2006] K Ray Chaudhuri, Daniel G Healy and Anthony HV Schapira. *Non-motor symptoms of Parkinson's disease: diagnosis and management.* The Lancet Neurology, vol. 5, no. 3, pages 235–245, 2006. (Cited on page 13.)

[Chavel 2006] Isaac Chavel. Riemannian geometry: a modern introduction, volume 98. Cambridge university press, 2006. (Cited on page 26.)

[Chung 2011] J.Y. Chung, M.H. In, S.H. Oh, M. Zaitsev, O. Speck and Z.H. Cho. *An improved PSF mapping method for EPI distortion correction in human brain at ultra high field (7T).* MAGMA, vol. 24, no. 3, pages 179–190, 2011. (Cited on page 40.)

[Ciccarelli 2008] Olga Ciccarelli, Marco Catani, Heidi Johansen-Berg, Chris Clark and Alan Thompson. *Diffusion-based tractography in neurological disorders: concepts, applications, and future developments.* The Lancet Neurology, vol. 7, no. 8, pages 715–727, 2008. (Cited on page 92.)

[Clark 2000] Chris A Clark and Denis Le Bihan. *Water diffusion compartmentation and anisotropy at high b values in the human brain.* Magnetic Resonance in Medicine, vol. 44, no. 6, pages 852–859, 2000. (Cited on page 34.)

[Cohen 2010] Ronald A Cohen and Lawrence H Sweet. Brain imaging in behavioral medicine and clinical neuroscience. Springer Science & Business Media, 2010. (Cited on page 17.)

[Commowick 2007] Olivier Commowick. *Création et utilisation d'atlas anatomiques numériques pour la radiothérapie.* PhD thesis, Université Nice Sophia Antipolis, 2007. (Cited on page 84.)

[Commowick 2008] Olivier Commowick, Pierre Fillard, Olivier Clatz and Simon Warfield. *Detection of DTI white matter abnormalities in multiple sclerosis patients.* Medical Image Computing and Computer-Assisted Intervention–MICCAI 2008, pages 975–982, 2008. (Cited on page 84.)

[Commowick 2012a] Olivier Commowick, Nicolas Wiest-Daesslé and Sylvain Prima. *Automated diffeomorphic registration of anatomical structures with rigid parts: Application to dynamic cervical MRI.* In Medical Image Computing and Computer-Assisted Intervention–MICCAI 2012, pages 163–170. Springer, 2012. (Cited on pages 41, 43 and 47.)

[Commowick 2012b] Olivier Commowick, Nicolas Wiest-Daesslé and Sylvain Prima. *Block-matching strategies for rigid registration of multimodal medical images.* In 2012 9th IEEE International Symposium on Biomedical Imaging (ISBI), pages 700–703. IEEE, 2012. (Cited on page 41.)

[Commowick 2012c] Olivier Commowick, Nicolas Wiest-Daesslé and Sylvain Prima. *Block-matching strategies for rigid registration of multimodal medical images.*

In Biomedical Imaging (ISBI), 2012 9th IEEE International Symposium on, pages 700–703. IEEE, 2012. (Cited on pages 86 and 88.)

[Commowick 2015] Olivier Commowick, Adil Maarouf, Jean-Christophe Ferré, Jean-Philippe Ranjeva, Gilles Edan and Christian Barillot. *Diffusion MRI abnormalities detection with orientation distribution functions: A multiple sclerosis longitudinal study.* Medical image analysis, vol. 22, no. 1, pages 114–123, 2015. (Cited on page 32.)

[Compston 1998] Alastair Compston, H Lassmann and I McDonald. *The story of multiple sclerosis.* McAlpine's Multiple Sclerosis. 3rd ed. London: Churchill Livingstone, 1998. (Cited on page 13.)

[Consortium 2011] International Multiple Sclerosis Genetics Consortium, Wellcome Trust Case Control Consortium 2*et al. Genetic risk and a primary role for cell-mediated immune mechanisms in multiple sclerosis.* Nature, vol. 476, no. 7359, pages 214–219, 2011. (Cited on page 13.)

[Cotton 2015] F Cotton, S Kremer, S Hannoun, S Vukusic, V Dousset*et al. OFSEP, a nationwide cohort of people with multiple sclerosis: Consensus minimal MRI protocol.* Journal of Neuroradiology, vol. 42, no. 3, pages 133–140, 2015. (Cited on page 107.)

[Crimi 2014] Alessandro Crimi, Olivier Commowick, Adil Maarouf, Jean-Christophe Ferré, Elise Bannier, Ayman Tourbah, Isabelle Berry, Jean-Philippe Ranjeva, Gilles Edan and Christian Barillot. *Predictive value of imaging markers at multiple sclerosis disease onset based on gadolinium-and USPIO-enhanced MRI and machine learning.* PloS one, vol. 9, no. 4, page e93024, 2014. (Cited on page 87.)

[Culver 1966] Walter J. Culver. *On the Existence and Uniqueness of the Real Logarithm of a Matrix.* Proceedings of the American Mathematical Society, vol. 17, no. 5, pages 1146–1151, 1966. (Cited on page 27.)

[Damadian 1976] Raymond Damadian, Lawrence Minkoff, Michael Goldsmith, Michael Stanford and Jason Koutcher. *Field focusing nuclear magnetic resonance (FONAR): visualization of a tumor in a live animal.* Science, vol. 194, no. 4272, pages 1430–1432, 1976. (Cited on page 14.)

[De Meyer 2003] Bernard De Meyer and Hadiza Moussa Saley. *On the strategic origin of Brownian motion in finance.* International Journal of Game Theory, vol. 31, no. 2, pages 285–319, 2003. (Cited on page 16.)

[Descoteaux 2007] Maxime Descoteaux, Elaine Angelino, Shaun Fitzgibbons and Rachid Deriche. *Regularized, fast, and robust analytical Q-ball imaging.* Magnetic Resonance in Medicine, vol. 58, no. 3, pages 497–510, 2007. (Cited on page 31.)

[Descoteaux 2009] Maxime Descoteaux, Rachid Deriche, Thomas R Knosche and Alfred Anwander. *Deterministic and probabilistic tractography based on complex fibre orientation distributions.* IEEE transactions on medical imaging, vol. 28, no. 2, pages 269–286, 2009. (Cited on page 31.)

[Descoteaux 2011] Maxime Descoteaux, Rachid Deriche, Denis Le Bihan, Jean-François Mangin and Cyril Poupon. *Multiple q-shell diffusion propagator imaging.* Medical image analysis, vol. 15, no. 4, pages 603–621, 2011. (Cited on page 33.)

[Einstein 1905] Albert Einstein. *Über die von der molekularkinetischen Theorie der Wärme geforderte Bewegung von in ruhenden Flüssigkeiten suspendierten Teilchen.* Annalen der physik, vol. 322, no. 8, pages 549–560, 1905. (Cited on page 16.)

[El-Sourgy 2015] Lamiaa El-Sourgy, Nermin Ahmad, Mohamed El-Rakhawy, Mohamed Gomaa and Mohamed Abo Hegazi. *Applications of MR fiber tractography imaging in multiple scleros.* The Egyptian Journal of Radiology and Nuclear Medicine, vol. 46, no. 2, pages 449–454, 2015. (Cited on page 92.)

[Ellis 2000] Kenneth J Ellis. *Human body composition: in vivo methods.* Physiological reviews, vol. 80, no. 2, pages 649–680, 2000. (Cited on pages 1 and 5.)

[Feragen 2016] Aasa Feragen and Andrea Fuster. *Geometries and interpolations for symmetric positive definite matrices.* 2016. (Cited on page 30.)

[Ferizi 2014a] Uran Ferizi, Torben Schneider*et al. A ranking of diffusion MRI compartment models with in vivo human brain data.* MRM, vol. 72, no. 6, pages 1785–1792, 2014. (Cited on page 61.)

[Ferizi 2014b] Uran Ferizi, Torben Schneider, Eleftheria Panagiotaki, Gemma Nedjati-Gilani, Hui Zhang, Claudia A. M. Wheeler-Kingshott and Daniel C. Alexander. *A ranking of diffusion MRI compartment models with in vivo human brain data.* Magnetic Resonance in Medicine, vol. 72, no. 6, pages 1785–1792, 2014. (Cited on page 40.)

[Fick 1855] Ann Fick. *Concerns diffusion and concentration gradient.* Annalen der Physik, vol. 170, no. 59, page 13, 1855. (Cited on page 15.)

[Filippi 2000] Massimo Filippi, Giuseppe Iannucci, Mara Cercignani, Maria Assunta Rocca, Arianna Pratesi and Giancarlo Comi. *A quantitative study of water diffusion in multiple sclerosis lesions and normal-appearing white matter using echo-planar imaging.* Archives of neurology, vol. 57, no. 7, pages 1017–1021, 2000. (Cited on page 97.)

[Filippi 2001] M Filippi, M Cercignani, M Inglese, MA Horsfield and G Comi. *Diffusion tensor magnetic resonance imaging in multiple sclerosis.* Neurology, vol. 56, no. 3, pages 304–311, 2001. (Cited on page 83.)

[Fletcher 2004] P Thomas Fletcher and Sarang Joshi. *Principal geodesic analysis on symmetric spaces: Statistics of diffusion tensors.* In Computer Vision and Mathematical Methods in Medical and Biomedical Image Analysis, pages 87–98. Springer, 2004. (Cited on page 28.)

[Floater 2005] Michael S Floater and Kai Hormann. *Surface parameterization: a tutorial and survey.* In Advances in multiresolution for geometric modelling, pages 157–186. Springer, 2005. (Cited on page 28.)

[Ford 1998] J Chetley Ford, David B Hackney, Ehud Lavi, Micheal Phillips and Upen Patel. *Dependence of apparent diffusion coefficients on axonal spacing, membrane permeability, and diffusion time in spinal cord white matter.* Journal of Magnetic Resonance Imaging, vol. 8, no. 4, pages 775–782, 1998. (Cited on page 35.)

[Funai 2008] Amanda K Funai, Jeffrey A Fessler, Desmond TB Yeo, Valur T Olafsson and Douglas C Noll. *Regularized field map estimation in MRI.* IEEE transactions on medical imaging, vol. 27, no. 10, pages 1484–1494, 2008. (Cited on page 22.)

[Gandhi 2005] Sonia Gandhi and Nicholas W Wood. *Molecular pathogenesis of Parkinson's disease.* Human molecular genetics, vol. 14, no. 18, pages 2749–2755, 2005. (Cited on page 13.)

[Gebker 2007] Rolf Gebker, Osama Gomaa, Bernhard Schnackenburg, Janina Rebakowski, Eckart Fleck and Eike Nagel. *Comparison of different MRI techniques for the assessment of thoracic aortic pathology: 3D contrast enhanced MR angiography, turbo spin echo and balanced steady state free precession.* The international journal of cardiovascular imaging, vol. 23, no. 6, pages 747–756, 2007. (Cited on pages 2 and 6.)

[Geng 2009a] Xiujuan Geng, Thomas J. Ross*et al. Diffusion MRI Registration Using Orientation Distribution Functions.* In IPMI '09, volume 5636 of *LNCS*, pages 626–637, 2009. (Cited on page 62.)

[Geng 2009b] Xiujuan Geng, Thomas J Ross, Wang Zhan, Hong Gu, Yi-Ping Chao, Ching-Po Lin, Gary E Christensen, Norbert Schuff and Yihong Yang. *Diffusion MRI registration using orientation distribution functions.* In International Conference on Information Processing in Medical Imaging, pages 626–637. Springer, 2009. (Cited on page 32.)

[Gerstl 1967] B Gerstl, LF Eng, RB Hayman, MG Tavaststjerna and PR Bond. *On the composition of human myelin.* Journal of neurochemistry, vol. 14, no. 6, pages 661–670, 1967. (Cited on page 12.)

[Goh 2011a] Alvina Goh, Christophe Lenglet, Paul M. Thompson and René Vidal. *A nonparametric Riemannian framework for processing high angular*

resolution diffusion images and its applications to ODF-based morphometry. Neuroimage, vol. 56, pages 1181–1201, 2011. (Cited on page 62.)

[Goh 2011b] Alvina Goh, Christophe Lenglet, Paul M Thompson and René Vidal. *A nonparametric Riemannian framework for processing high angular resolution diffusion images and its applications to ODF-based morphometry.* NeuroImage, vol. 56, no. 3, pages 1181–1201, 2011. (Cited on page 32.)

[Gómez Paccard 2006] Miriam Gómez Paccard. *Étude de la variation de la direction et de l'intensité du champ géomagnétique en Espagne durant les deux derniers millénaires.* PhD thesis, Rennes 1, 2006. (Cited on page 17.)

[Guimond 2000] Alexandre Guimond, Jean Meunier and Jean-Philippe Thirion. *Average brain models: A convergence study.* Computer vision and image understanding, vol. 77, no. 2, pages 192–210, 2000. (Cited on pages 78 and 85.)

[Hagler 2009] Donald J Hagler, Mazyar E Ahmadi, Joshua Kuperman, Dominic Holland, Carrie R McDonald, Eric Halgren and Anders M Dale. *Automated white-matter tractography using a probabilistic diffusion tensor atlas: Application to temporal lobe epilepsy.* Human brain mapping, vol. 30, no. 5, pages 1535–1547, 2009. (Cited on page 92.)

[Hahn 1950] Erwin L Hahn. *Spin echoes.* Physical review, vol. 80, no. 4, page 580, 1950. (Cited on page 15.)

[Hall 2015] Brian C Hall. Lie groups, lie algebras, and representations: an elementary introduction, volume 222. Springer, 2015. (Cited on page 27.)

[Haralick 1985] Robert M Haralick and Linda G Shapiro. *Image segmentation techniques.* Computer vision, graphics, and image processing, vol. 29, no. 1, pages 100–132, 1985. (Cited on page 64.)

[Harris 1980] Kenneth R Harris and Lawrence A Woolf. *Pressure and temperature dependence of the self diffusion coefficient of water and oxygen-18 water.* Journal of the Chemical Society, Faraday Transactions 1: Physical Chemistry in Condensed Phases, vol. 76, pages 377–385, 1980. (Cited on page 34.)

[Hartigan 1979] John A Hartigan and Manchek A Wong. *Algorithm AS 136: A k-means clustering algorithm.* Journal of the Royal Statistical Society. Series C (Applied Statistics), vol. 28, no. 1, pages 100–108, 1979. (Cited on page 65.)

[Hartung 2000] Hans-Peter Hartung and Bernd C Kieseier. *The role of matrix metalloproteinases in autoimmune damage to the central and peripheral nervous system.* Journal of neuroimmunology, vol. 107, no. 2, pages 140–147, 2000. (Cited on page 13.)

[Hartwig 2009] Valentina Hartwig, Giulio Giovannetti, Nicola Vanello, Massimo Lombardi, Luigi Landini and Silvana Simi. *Biological effects and safety in*

magnetic resonance imaging: a review. International journal of environmental research and public health, vol. 6, no. 6, pages 1778–1798, 2009. (Cited on page 5.)

[Hedström 2012] Anna K Hedström, Tomas Olsson and Lars Alfredsson. *High body mass index before age 20 is associated with increased risk for multiple sclerosis in both men and women.* Multiple Sclerosis Journal, vol. 18, no. 9, pages 1334–1336, 2012. (Cited on page 13.)

[Hennig 1986] J Hennig, A Nauerth and H Friedburg. *RARE imaging: a fast imaging method for clinical MR.* Magnetic resonance in medicine, vol. 3, no. 6, pages 823–833, 1986. (Cited on page 21.)

[Hesseltine 2007] Stephen M Hesseltine, Yulin Ge and Meng Law. *Applications of diffusion tensor imaging and fiber tractography.* Applied Radiology, vol. 36, no. 5, page 8, 2007. (Cited on page 92.)

[Hilgetag 2009] Claus C Hilgetag and Helen Barbas. *Are there ten times more glia than neurons in the brain?* Brain Structure and Function, vol. 213, no. 4-5, pages 365–366, 2009. (Cited on page 11.)

[Hobson 1931] Ernest William Hobson. The theory of spherical and ellipsoidal harmonics. CUP Archive, 1931. (Cited on page 31.)

[Holdsworth 2008] Samantha J Holdsworth, Stefan Skare, Rexford D Newbould, Raphael Guzmann, Nikolas H Blevins and Roland Bammer. *Readout-segmented EPI for rapid high resolution diffusion imaging at 3T.* European journal of radiology, vol. 65, no. 1, pages 36–46, 2008. (Cited on page 106.)

[Holland 2010] Dominic Holland, Joshua M Kuperman and Anders M Dale. *Efficient correction of inhomogeneous static magnetic field-induced distortion in Echo Planar Imaging.* Neuroimage, vol. 50, no. 1, pages 175–183, 2010. (Cited on pages 40 and 41.)

[Holodny 2001] Andrei I Holodny, Theodore H Schwartz, Martin Ollenschleger, Wen-Ching Liu and Michael Schulder. *Tumor involvement of the corticospinal tract: diffusion magnetic resonance tractography with intraoperative correlation: Case illustration.* Journal of neurosurgery, vol. 95, no. 6, pages 1082–1082, 2001. (Cited on page 92.)

[Huberty 2003] Carl J Huberty. *Multiple correlation versus multiple regression.* Educational and Psychological Measurement, vol. 63, no. 2, pages 271–278, 2003. (Cited on page 59.)

[Huettel 2004] Scott A Huettel, Allen W Song and Gregory McCarthy. Functional magnetic resonance imaging, volume 1. Sinauer Associates Sunderland, 2004. (Cited on page 40.)

[In 2015] Myung-Ho In, Oleg Posnansky, Erik B Beall, Mark J Lowe and Oliver Speck. *Distortion Correction in EPI Using an Extended PSF Method with a Reversed Phase Gradient Approach*. PloS One, vol. 10, no. 2, 2015. (Cited on page 41.)

[Irfanoglu 2015] M.O. Irfanoglu, P. Modi, A. Nayak, E.B. Hutchinson, J. Sarlis and C. Pierpaoli. *DR-BUDDI (Diffeomorphic Registration for Blip-Up blip-Down Diffusion Imaging) method for correcting echo planar imaging distortions*. Neuroimage, vol. 106, pages 284–299, 2015. (Cited on pages 41, 42 and 105.)

[Jack 2010] Clifford R Jack, David S Knopman, William J Jagust, Leslie M Shaw, Paul S Aisen, Michael W Weiner, Ronald C Petersen and John Q Trojanowski. *Hypothetical model of dynamic biomarkers of the Alzheimer's pathological cascade*. The Lancet Neurology, vol. 9, no. 1, pages 119–128, 2010. (Cited on page 13.)

[Jain 1999] Anil K Jain, M Narasimha Murty and Patrick J Flynn. *Data clustering: a review*. ACM computing surveys (CSUR), vol. 31, no. 3, pages 264–323, 1999. (Cited on page 64.)

[Jezzard 1995] P. Jezzard and R. S. Balaban. *Correction for geometric distortion in echo planar images from B0 field variations*. MRM, vol. 34, no. 1, pages 65–73, 1995. (Cited on pages 40, 41 and 42.)

[Jezzard 1998] Peter Jezzard, Alan S Barnett and Carlo Pierpaoli. *Characterization of and correction for eddy current artifacts in echo planar diffusion imaging*. Magnetic resonance in medicine, vol. 39, no. 5, pages 801–812, 1998. (Cited on pages 21 and 22.)

[Johansen-Berg 2009] H. Johansen-Berg and T.E.J. Behrens. Diffusion mri: From quantitative measurement to in-vivo neuroanatomy. Academic Press, 2009. (Cited on pages 18, 19, 23 and 40.)

[Johansen-Berg 2013] Heidi Johansen-Berg and Timothy EJ Behrens. Diffusion mri: from quantitative measurement to in vivo neuroanatomy. Academic Press, 2013. (Cited on page 21.)

[Jones 2004] Derek K Jones and Peter J Basser. *"Squashing peanuts and smashing pumpkins": How noise distorts diffusion-weighted MR data*. Magnetic Resonance in Medicine, vol. 52, no. 5, pages 979–993, 2004. (Cited on page 22.)

[Kanungo 2002] Tapas Kanungo, David M Mount, Nathan S Netanyahu, Christine D Piatko, Ruth Silverman and Angela Y Wu. *An efficient k-means clustering algorithm: Analysis and implementation*. IEEE transactions on pattern analysis and machine intelligence, vol. 24, no. 7, pages 881–892, 2002. (Cited on page 65.)

[Kendall 1990] Wilfrid S Kendall. *Probability, convexity, and harmonic maps with small image I: uniqueness and fine existence.* Proceedings of the London Mathematical Society, vol. 3, no. 2, pages 371–406, 1990. (Cited on page 28.)

[Kindlmann 2007] Gordon Kindlmann, Raul San Jose Estepar, Marc Niethammer, Steven Haker and Carl-Fredrik Westin. *Geodesic-loxodromes for diffusion tensor interpolation and difference measurement.* In International Conference on Medical Image Computing and Computer-Assisted Intervention, pages 1–9. Springer, 2007. (Cited on page 28.)

[Klein 2009] Arno Klein, Jesper Andersson, Babak A Ardekani, John Ashburner, Brian Avants, Ming-Chang Chiang, Gary E Christensen, D Louis Collins, James Gee, Pierre Hellier*et al. Evaluation of 14 nonlinear deformation algorithms applied to human brain MRI registration.* Neuroimage, vol. 46, no. 3, pages 786–802, 2009. (Cited on page 86.)

[Koay 2006] Cheng Guan Koay, Lin-Ching Chang, John D Carew, Carlo Pierpaoli and Peter J Basser. *A unifying theoretical and algorithmic framework for least squares methods of estimation in diffusion tensor imaging.* Journal of Magnetic Resonance, vol. 182, no. 1, pages 115–125, 2006. (Cited on page 23.)

[Koch 2004] Christof Koch. Biophysics of computation: information processing in single neurons. Oxford university press, 2004. (Cited on page 12.)

[Kötter 2001] R Kötter. *Neuroscience databases: tools for exploring brain structure–function relationships.* Philosophical Transactions of the Royal Society of London B: Biological Sciences, vol. 356, no. 1412, pages 1111–1120, 2001. (Cited on page 13.)

[Kreis 1993] R Kreis, Th Ernst and BD Ross. *Absolute quantitation of water and metabolites in the human brain. II. Metabolite concentrations.* Journal of magnetic resonance, Series B, vol. 102, no. 1, pages 9–19, 1993. (Cited on page 16.)

[Kutzelnigg 2005] Alexandra Kutzelnigg, Claudia F Lucchinetti, Christine Stadelmann, Wolfgang Brück, Helmut Rauschka, Markus Bergmann, Manfred Schmidbauer, Joseph E Parisi and Hans Lassmann. *Cortical demyelination and diffuse white matter injury in multiple sclerosis.* Brain, vol. 128, no. 11, pages 2705–2712, 2005. (Cited on page 24.)

[Laatsch 1962] Robert H Laatsch, Marian W Kies, Spencer Gordon and Ellsworth C Alvord Jr. *The encephalomyelitic activity of myelin isolated by ultracentrifugation.* The Journal of experimental medicine, vol. 115, no. 4, page 777, 1962. (Cited on page 12.)

[Lambrechts 2003] Diether Lambrechts, Erik Storkebaum, Masafumi Morimoto, Jurgen Del-Favero, Frederik Desmet, Stefan L Marklund, Sabine Wyns, Vincent Thijs, Jörgen Andersson, Ingrid van Marion*et al. VEGF is a modifier of*

amyotrophic lateral sclerosis in mice and humans and protects motoneurons against ischemic death. Nature genetics, vol. 34, no. 4, pages 383–394, 2003. (Cited on page 13.)

[Lancaster 2000] Jack L Lancaster, Marty G Woldorff, Lawrence M Parsons, Mario Liotti, Catarina S Freitas, Lacy Rainey, Peter V Kochunov, Dan Nickerson, Shawn A Mikiten and Peter T Fox. *Automated Talairach atlas labels for functional brain mapping.* Human brain mapping, vol. 10, no. 3, pages 120–131, 2000. (Cited on page 84.)

[Landman 2007] Bennett Landman, Pierre-Louis Bazin and Jerry Prince. *Diffusion tensor estimation by maximizing Rician likelihood.* In Computer Vision, 2007. ICCV 2007. IEEE 11th International Conference on, pages 1–8. IEEE, 2007. (Cited on page 23.)

[Le Bihan 1986] Denis Le Bihan, Eric Breton, Denis Lallemand, Philippe Grenier, Emmanuel Cabanis and Maurice Laval-Jeantet. *MR imaging of intravoxel incoherent motions: application to diffusion and perfusion in neurologic disorders.* Radiology, vol. 161, no. 2, pages 401–407, 1986. (Cited on page 15.)

[Le Bihan 2012] Denis Le Bihan and Heidi Johansen-Berg. *Diffusion MRI at 25: exploring brain tissue structure and function.* Neuroimage, vol. 61, no. 2, pages 324–341, 2012. (Cited on page 15.)

[Lee 2006] John M Lee. Riemannian manifolds: an introduction to curvature, volume 176. Springer Science & Business Media, 2006. (Cited on page 26.)

[Legler 1999] Julie M Legler, Lynn A Gloeckler Ries, Malcolm A Smith, Joan L Warren, Ellen F Heineman, Richard S Kaplan and Martha S Linet. *Brain and other central nervous system cancers: recent trends in incidence and mortality.* Journal of the National Cancer Institute, vol. 91, no. 16, pages 1382–1390, 1999. (Cited on page 12.)

[Lenglet 2006] Christophe Lenglet, Mikaël Rousson, Rachid Deriche and Olivier Faugeras. *Statistics on the manifold of multivariate normal distributions: Theory and application to diffusion tensor MRI processing.* Journal of Mathematical Imaging and Vision, vol. 25, no. 3, pages 423–444, 2006. (Cited on page 27.)

[Lentner 1981] C Lentner. *Geigy Scientific Tables. Vol 1: Units of Measurement, Body Fluids, Composition of the Body.* Nutrition. Basle, Switzerland: Ciba-Geigy Limited, 1981. (Cited on page 16.)

[Lepore 2008] Natasha Lepore, Caroline Brun, Yi-Yu Chou, Ming-Chang Chiang, Rebecca A Dutton, Kiralee M Hayashi, Eileen Luders, Oscar L Lopez, Howard J Aizenstein, Arthur W Toga*et al.* *Generalized tensor-based morphometry of HIV/AIDS using multivariate statistics on deformation tensors.*

IEEE transactions on medical imaging, vol. 27, no. 1, pages 129–141, 2008. (Cited on page 84.)

[Lewin 1991] Leonard Lewin. Structural properties of polylogarithms. Number 37. American Mathematical Soc., 1991. (Cited on page 37.)

[Likas 2003] Aristidis Likas, Nikos Vlassis and Jakob J Verbeek. *The global k-means clustering algorithm.* Pattern recognition, vol. 36, no. 2, pages 451–461, 2003. (Cited on page 65.)

[Liu 1996] Guoying Liu, Peter Van Gelderen, Jeff Duyn and Chrit TW Moonen. *Single-shot diffusion MRI of human brain on a conventional clinical instrument.* Magnetic resonance in medicine, vol. 35, no. 5, pages 671–677, 1996. (Cited on page 21.)

[Lloyd 1982] Stuart Lloyd. *Least squares quantization in PCM.* IEEE transactions on information theory, vol. 28, no. 2, pages 129–137, 1982. (Cited on page 64.)

[Lublin 1996] Fred D Lublin, Stephen C Reingold*et al.* *Defining the clinical course of multiple sclerosis results of an international survey.* Neurology, vol. 46, no. 4, pages 907–911, 1996. (Cited on page 13.)

[Lucchinetti 2000] Claudia Lucchinetti, Wolfgang Bruck, Joseph Parisi, Bernd Scheithauer, Moses Rodriguez, Hans Lassman*et al.* *Heterogeneity of multiple sclerosis lesions: implications for the pathogenesis of demyelination.* Annals of neurology, vol. 47, no. 6, pages 707–717, 2000. (Cited on page 24.)

[Lythgoe 1997] Mark F Lythgoe, Albert L Busza, Fernando Calamante, Christopher H Sotak, Martin D King, Anna C Bingham, Stephen R Williams and David G Gadian. *Effects of diffusion anisotropy on lesion delineation in a rat model of cerebral ischemia.* Magnetic resonance in medicine, vol. 38, no. 4, pages 662–668, 1997. (Cited on page 23.)

[Mahajan 2009] Meena Mahajan, Prajakta Nimbhorkar and Kasturi Varadarajan. *The planar k-means problem is NP-hard.* In International Workshop on Algorithms and Computation, pages 274–285. Springer, 2009. (Cited on page 65.)

[Maier 2010] Stephan E Maier, Yanping Sun and Robert V Mulkern. *Diffusion imaging of brain tumors.* NMR in biomedicine, vol. 23, no. 7, pages 849–864, 2010. (Cited on page 16.)

[Mallat 1989] Stephane G Mallat. *A theory for multiresolution signal decomposition: the wavelet representation.* IEEE transactions on pattern analysis and machine intelligence, vol. 11, no. 7, pages 674–693, 1989. (Cited on page 30.)

[Mardia 2009] Kanti V Mardia and Peter E Jupp. Directional statistics, volume 494. John Wiley & Sons, 2009. (Cited on page 37.)

[Markiewicz 2006] Inga Markiewicz and Barbara Lukomska. *The role of astrocytes in the physiology and pathology of the central nervous system.* Acta Neurobiol Exp (Wars), vol. 66, no. 4, pages 343–358, 2006. (Cited on page 12.)

[Marner 2003] Lisbeth Marner, Jens R Nyengaard, Yong Tang and Bente Pakkenberg. *Marked loss of myelinated nerve fibers in the human brain with age.* Journal of comparative neurology, vol. 462, no. 2, pages 144–152, 2003. (Cited on page 11.)

[McGraw 2004] Tim McGraw, Baba C Vemuri, Yunmei Chen, Murali Rao and Thomas Mareci. *DT-MRI denoising and neuronal fiber tracking.* Medical image analysis, vol. 8, no. 2, pages 95–111, 2004. (Cited on page 22.)

[McGraw 2006] T. McGraw and B.C. Vemuri. *Von Mises-Fisher mixture model of the diffusion ODF.* In IEEE ISBI, pages 65–8, 2006. (Cited on page 72.)

[Menzel 2011] Marion I Menzel, Ek T Tan, Kedar Khare, Jonathan I Sperl, Kevin F King, Xiaodong Tao, Christopher J Hardy and Luca Marinelli. *Accelerated diffusion spectrum imaging in the human brain using compressed sensing.* Magnetic Resonance in Medicine, vol. 66, no. 5, pages 1226–1233, 2011. (Cited on page 33.)

[Mervaala 2000] Esa Mervaala, J Föhr, M Könönen, M Valkonen-Korhonen, P Vainio, K Partanen, J Partanen, J Tiihonen, H Viinamäki, A-K Karjalainen*et al. Quantitative MRI of the hippocampus and amygdala in severe depression.* Psychological medicine, vol. 30, no. 01, pages 117–125, 2000. (Cited on page 13.)

[Meyer 1992] Craig H Meyer, Bob S Hu, Dwight G Nishimura and Albert Macovski. *Fast spiral coronary artery imaging.* Magnetic Resonance in Medicine, vol. 28, no. 2, pages 202–213, 1992. (Cited on page 21.)

[Mlynárik 2001] Vladimír Mlynárik, Stephan Gruber and Ewald Moser. *Proton T1 and T2 relaxation times of human brain metabolites at 3 Tesla.* NMR in biomedicine, vol. 14, no. 5, pages 325–331, 2001. (Cited on page 17.)

[Morgan 2004] P.S. Morgan, R.W. Bowtell, D.J. McIntyre and B.S. Worthington. *Correction of spatial distortion in EPI due to inhomogeneous static magnetic fields using the reversed gradient method.* Journal of Magnetic Resonance Imaging, vol. 19, no. 4, pages 499–507, 2004. (Cited on pages 41 and 42.)

[Mori 1999] Susumu Mori, Barbara J Crain, Vadappuram P Chacko and Peter Van Zijl. *Three-dimensional tracking of axonal projections in the brain by magnetic resonance imaging.* Annals of neurology, vol. 45, no. 2, pages 265–269, 1999. (Cited on page 95.)

[Moseley 1990] ME Moseley, Y Cohen, J Mintorovitch, L Chileuitt, H Shimizu, J Kucharczyk, MF Wendland and PR Weinstein. *Early detection of regional*

cerebral ischemia in cats: comparison of diffusion-and T2-weighted MRI and spectroscopy. Magnetic resonance in medicine, vol. 14, no. 2, pages 330–346, 1990. (Cited on page 15.)

[Müller 2006] Claus Müller. Spherical harmonics, volume 17. Springer, 2006. (Cited on page 31.)

[Neuman 1974] CH Neuman. *Spin echo of spins diffusing in a bounded medium.* The Journal of Chemical Physics, vol. 60, no. 11, pages 4508–4511, 1974. (Cited on page 38.)

[Ng 2002] Andrew Y Ng, Michael I Jordan, Yair Weiss*et al.* *On spectral clustering: Analysis and an algorithm.* Advances in neural information processing systems, vol. 2, pages 849–856, 2002. (Cited on pages 62, 63 and 65.)

[Ning 2015] Lipeng Ning, Carl-Fredrik Westin and Yogesh Rathi. *Estimating diffusion propagator and its moments using directional radial basis functions.* IEEE transactions on medical imaging, vol. 34, no. 10, pages 2058–2078, 2015. (Cited on page 20.)

[Nordberg 2010] Agneta Nordberg, Juha O Rinne, Ahmadul Kadir and Bengt Långström. *The use of PET in Alzheimer disease.* Nature Reviews Neurology, vol. 6, no. 2, pages 78–87, 2010. (Cited on page 13.)

[Orton 2006] Sarah-Michelle Orton, Blanca M Herrera, Irene M Yee, William Valdar, Sreeram V Ramagopalan, A Dessa Sadovnick, George C Ebers, Canadian Collaborative Study Group*et al.* *Sex ratio of multiple sclerosis in Canada: a longitudinal study.* The Lancet Neurology, vol. 5, no. 11, pages 932–936, 2006. (Cited on page 13.)

[Ourselin 2000] Sébastien Ourselin, Alexis Roche, Sylvain Prima and Nicholas Ayache. *Block matching: A general framework to improve robustness of rigid registration of medical images.* In Medical Image Computing and Computer-Assisted Intervention–MICCAI 2000, pages 557–566. Springer, 2000. (Cited on pages 41, 43, 86 and 88.)

[Padhani 2009] Anwar R Padhani, Guoying Liu, Dow Mu-Koh, Thomas L Chenevert, Harriet C Thoeny, Taro Takahara, Andrew Dzik-Jurasz, Brian D Ross, Marc Van Cauteren, David Collins*et al.* *Diffusion-weighted magnetic resonance imaging as a cancer biomarker: consensus and recommendations.* Neoplasia, vol. 11, no. 2, pages 102–125, 2009. (Cited on page 16.)

[Pakkenberg 1988] B Pakkenberg and HJG Gundersen. *Total number of neurons and glial cells in human brain nuclei estimated by the disector and the fractionator.* Journal of microscopy, vol. 150, no. 1, pages 1–20, 1988. (Cited on page 11.)

[Pal 2005] Nikhil R Pal, Kuhu Pal, James M Keller and James C Bezdek. *A possibilistic fuzzy c-means clustering algorithm.* IEEE Transactions on Fuzzy Systems, vol. 13, no. 4, pages 517–530, 2005. (Cited on page 65.)

[Panagiotaki 2012] Eleftheria Panagiotaki, Torben Schneider, Bernard Siow, Matt G Hall, Mark F Lythgoe and Daniel C Alexander. *Compartment models of the diffusion MR signal in brain white matter: a taxonomy and comparison.* Neuroimage, vol. 59, no. 3, pages 2241–2254, 2012. (Cited on page 34.)

[Park 2005] Hae-Jeong Park. *Quantification of white matter using diffusion-tensor imaging.* Int Rev Neurobiol, vol. 66, pages 167–212, 2005. (Cited on page 24.)

[Park 2009] Hae-Sang Park and Chi-Hyuck Jun. *A simple and fast algorithm for K-medoids clustering.* Expert systems with applications, vol. 36, no. 2, pages 3336–3341, 2009. (Cited on page 65.)

[Parmar 2004] Hemant Parmar, Yih-Yian Sitoh and Tseng Tsai Yeo. *Combined magnetic resonance tractography and functional magnetic resonance imaging in evaluation of brain tumors involving the motor system.* Journal of computer assisted tomography, vol. 28, no. 4, pages 551–556, 2004. (Cited on page 92.)

[Pasternak 2009] Ofer Pasternak, Nir Sochen, Yaniv Gur, Nathan Intrator and Yaniv Assaf. *Free water elimination and mapping from diffusion MRI.* Magnetic Resonance in Medicine, vol. 62, no. 3, pages 717–730, 2009. (Cited on page 34.)

[Pasternak 2010] Ofer Pasternak, Nir Sochen and Peter J Basser. *The effect of metric selection on the analysis of diffusion tensor MRI data.* NeuroImage, vol. 49, no. 3, pages 2190–2204, 2010. (Cited on page 25.)

[Paulsen 2001] Jane S Paulsen, RE Ready, JM Hamilton, MS Mega and JL Cummings. *Neuropsychiatric aspects of Huntington's disease.* Journal of Neurology, Neurosurgery & Psychiatry, vol. 71, no. 3, pages 310–314, 2001. (Cited on page 13.)

[Pennec 2006] Xavier Pennec, Pierre Fillard and Nicholas Ayache. *A Riemannian framework for tensor computing.* International Journal of Computer Vision, vol. 66, no. 1, pages 41–66, 2006. (Cited on page 27.)

[Pierpaoli 1996] Carlo Pierpaoli and Peter J Basser. *Toward a quantitative assessment of diffusion anisotropy.* Magnetic resonance in Medicine, vol. 36, no. 6, pages 893–906, 1996. (Cited on page 38.)

[Pluchino 2003] Stefano Pluchino, Angelo Quattrini, Elena Brambilla, Angela Gritti, Giuliana Salani, Giorgia Dina, Rossella Galli, Ubaldo Del Carro, Stefano Amadio, Alessandra Bergami*et al.* *Injection of adult neurospheres*

induces recovery in a chronic model of multiple sclerosis. Nature, vol. 422, no. 6933, pages 688–694, 2003. (Cited on page 13.)

[Polman 2005] Chris H Polman, Stephen C Reingold, Gilles Edan, Massimo Filippi, Hans-Peter Hartung, Ludwig Kappos, Fred D Lublin, Luanne M Metz, Henry F McFarland, Paul W O'Connor*et al. Diagnostic criteria for multiple sclerosis: 2005 revisions to the "McDonald Criteria".* Annals of neurology, vol. 58, no. 6, pages 840–846, 2005. (Cited on pages 2, 6 and 13.)

[Porter 2009] David A Porter and Robin M Heidemann. *High resolution diffusion-weighted imaging using readout-segmented echo-planar imaging, parallel imaging and a two-dimensional navigator-based reacquisition.* Magnetic resonance in medicine, vol. 62, no. 2, pages 468–475, 2009. (Cited on pages 60 and 106.)

[Powell 2009] Michael JD Powell. *The BOBYQA algorithm for bound constrained optimization without derivatives.* Technical report, Centre for Mathematical Sciences, University of Cambridge, UK, 2009. (Cited on page 46.)

[Purcell 1946] Edward M Purcell, HC Torrey and Robert V Pound. *Resonance absorption by nuclear magnetic moments in a solid.* Physical review, vol. 69, no. 1-2, page 37, 1946. (Cited on page 14.)

[Raffelt 2011] David Raffelt, J-Donald Tournier, Jurgen Fripp, Stuart Crozier, Alan Connelly and Olivier Salvado. *Symmetric diffeomorphic registration of fibre orientation distributions.* NeuroImage, vol. 56, no. 3, pages 1171–1180, 2011. (Cited on page 32.)

[Reber 1998] P.J. Reber, E.C. Wong, R.B. Buxton and L.R. Frank. *Correction of off resonance-related distortion in echo-planar imaging using EPI-based field maps.* Magnetic Resonance in Medicine, vol. 39, no. 2, pages 328–330, 1998. (Cited on page 40.)

[Reese 2003] TG Reese, O Heid, RM Weisskoff and VJ Wedeen. *Reduction of eddy-current-induced distortion in diffusion MRI using a twice-refocused spin echo.* Magnetic Resonance in Medicine, vol. 49, no. 1, pages 177–182, 2003. (Cited on page 21.)

[Robson 1997] M.D. Robson, J.C. Gore and R.T. Constable. *Measurement of the point spread function in MRI using constant time imaging.* Magnetic Resonance in Medicine, vol. 38, no. 5, pages 733–740, 1997. (Cited on page 40.)

[Rohde 2004] GK Rohde, AS Barnett, PJ Basser, S Marenco and C Pierpaoli. *Comprehensive approach for correction of motion and distortion in diffusion-weighted MRI.* Magnetic resonance in medicine, vol. 51, no. 1, pages 103–114, 2004. (Cited on page 22.)

[Romano 2009] A Romano, G D'andrea, G Minniti, L Mastronardi, L Ferrante, LM Fantozzi and A Bozzao. *Pre-surgical planning and MR-tractography utility in brain tumour resection.* European radiology, vol. 19, no. 12, page 2798, 2009. (Cited on page 92.)

[Ruiz-Alzola 2002a] J. Ruiz-Alzola, C.-F. Westin*et al.* *Nonrigid registration of 3D tensor medical data.* Medical Image Analysis, vol. 6, no. 2, pages 143–161, June 2002. (Cited on page 79.)

[Ruiz-Alzola 2002b] Juan Ruiz-Alzola, C-F Westin, Simon K Warfield, C Alberola, S Maier and Ron Kikinis. *Nonrigid registration of 3D tensor medical data.* Medical image analysis, vol. 6, no. 2, pages 143–161, 2002. (Cited on pages 86, 87 and 106.)

[Sakamoto 1986] Yosiyuki Sakamoto, Makio Ishiguro and Genshiro Kitagawa. *Akaike information criterion statistics.* Dordrecht, The Netherlands: D. Reidel, 1986. (Cited on page 81.)

[Sandrasegaran 2005] Kumaresan Sandrasegaran, Arumugam Rajesh, Daniel A Rushing, Jonas Rydberg, Fatih M Akisik and John D Henley. *Gastrointestinal stromal tumors: CT and MRI findings.* European radiology, vol. 15, no. 7, pages 1407–1414, 2005. (Cited on pages 2 and 6.)

[Sanguinetti 2005] Guido Sanguinetti, Jonathan Laidler and Neil D Lawrence. *Automatic determination of the number of clusters using spectral algorithms.* In Machine Learning for Signal Processing, 2005 IEEE Workshop on, pages 55–60. IEEE, 2005. (Cited on page 81.)

[Schaltenbrand 1998] Georges Schaltenbrand and Waldemar Wahren. Atlas for stereotaxy of the human brain: with an accompanying guide. Thieme, 1998. (Cited on page 84.)

[Scherrer 2010] Benoit Scherrer and Simon K Warfield. *Why multiple b-values are required for multi-tensor models. Evaluation with a constrained log-Euclidean model.* In Biomedical Imaging: From Nano to Macro, 2010 IEEE International Symposium on, pages 1389–1392. IEEE, 2010. (Cited on page 37.)

[Scherrer 2012] Benoit Scherrer and Simon K Warfield. *Parametric representation of multiple white matter fascicles from cube and sphere diffusion MRI.* PLoS one, vol. 7, no. 11, page e48232, 2012. (Cited on page 107.)

[Schoenberg 1973] Isaac Jacob Schoenberg. Cardinal spline interpolation, volume 12 of *Regional conference series in applied mathematics.* Philadelphia, Society for Industrial and Applied Mathematics, 1973. (Cited on page 50.)

[Schröder 1978] JM Schröder, J Bohl and K Brodda. *Changes of the ratio between myelin thickness and axon diameter in the human developing sural nerve.*

Acta neuropathologica, vol. 43, no. 1-2, pages 169–178, 1978. (Cited on page 11.)

[Serrai 2005] Hacene Serrai and Lotfi Senhadji. *Acquisition time reduction in magnetic resonance spectroscopic imaging using discrete wavelet encoding*. Journal of Magnetic Resonance, vol. 177, no. 1, pages 22–30, 2005. (Cited on page 20.)

[Siri 1961] William E Siri*et al.* *Body composition from fluid spaces and density: analysis of methods*. Techniques for measuring body composition, vol. 61, pages 223–44, 1961. (Cited on pages 1 and 5.)

[Smith 2006] Stephen M Smith, Mark Jenkinson, Heidi Johansen-Berg, Daniel Rueckert, Thomas E Nichols, Clare E Mackay, Kate E Watkins, Olga Ciccarelli, M Zaheer Cader, Paul M Matthews*et al.* *Tract-based spatial statistics: voxelwise analysis of multi-subject diffusion data*. Neuroimage, vol. 31, no. 4, pages 1487–1505, 2006. (Cited on page 92.)

[Soares 2013] Jose Soares, Paulo Marques, Victor Alves and Nuno Sousa. *A hitchhiker's guide to diffusion tensor imaging*. Frontiers in neuroscience, vol. 7, page 31, 2013. (Cited on page 24.)

[Sofroniew 2010] Michael V Sofroniew and Harry V Vinters. *Astrocytes: biology and pathology*. Acta neuropathologica, vol. 119, no. 1, pages 7–35, 2010. (Cited on page 12.)

[Song 2002] Sheng-Kwei Song, Shu-Wei Sun, Michael J Ramsbottom, Chen Chang, John Russell and Anne H Cross. *Dysmyelination revealed through MRI as increased radial (but unchanged axial) diffusion of water*. Neuroimage, vol. 17, no. 3, pages 1429–1436, 2002. (Cited on page 24.)

[Sotiropoulos 2012] Stamatios N Sotiropoulos, Timothy EJ Behrens and Saad Jbabdi. *Ball and rackets: inferring fiber fanning from diffusion-weighted MRI*. NeuroImage, vol. 60, no. 2, pages 1412–1425, 2012. (Cited on page 37.)

[Spiegel 1991] Murray R Spiegel. Advanced mathematics. McGraw-Hill, Incorporated, 1991. (Cited on page 33.)

[Spielmat 1996] Daniel A Spielmat and Shang-Hua Teng. *Spectral partitioning works: Planar graphs and finite element meshes*. In Foundations of Computer Science, 1996. Proceedings., 37th Annual Symposium on, pages 96–105. IEEE, 1996. (Cited on page 65.)

[Sporns 2005] Olaf Sporns, Giulio Tononi and Rolf Kötter. *The human connectome: a structural description of the human brain*. PLoS Comput Biol, vol. 1, no. 4, page e42, 2005. (Cited on page 13.)

[Stachel 2005] John J Stachel. *Einstein's miraculous year: five papers that changed the face of physics*. 2005. (Cited on page 16.)

[Stamm 2012a] A. Stamm, P. Pérez and C. Barillot. *A new multi-fiber model for low angular resolution diffusion MRI.* In Biomedical Imaging (ISBI), 2012 9th IEEE International Symposium on, pages 936–939, May 2012. (Cited on page 40.)

[Stamm 2012b] Aymeric Stamm, Patrick Pérez and Christian Barillot. *A new multi-fiber model for low angular resolution diffusion MRI.* In ISBI, pages 936–939. IEEE, 2012. (Cited on pages 62 and 73.)

[Stamm 2012c] Aymeric Stamm, Patrick Pérez and Christian Barillot. *A new multi-fiber model for low angular resolution diffusion MRI.* In Biomedical Imaging (ISBI), 2012 9th IEEE International Symposium on, pages 936–939. IEEE, 2012. (Cited on page 68.)

[Stamm 2013] Aymeric Stamm. *Diffusion directions imaging: high resolution reconstruction of white matter fascicles from low angular resolution diffusion MRI.* PhD thesis, Université Rennes 1, 2013. (Cited on pages 34, 36 and 89.)

[Stamm 2016] Aymeric Stamm, Olivier Commowick, Simon K Warfield and Simone Vantini. *Comprehensive Maximum Likelihood Estimation of Diffusion Compartment Models Towards Reliable Mapping of Brain Microstructure.* In International Conference on Medical Image Computing and Computer-Assisted Intervention, pages 622–630. Springer, 2016. (Cited on pages 36, 75 and 88.)

[Stanisz 1997] Greg J Stanisz, Graham A Wright, R Mark Henkelman and Aaron Szafer. *An analytical model of restricted diffusion in bovine optic nerve.* Magnetic Resonance in Medicine, vol. 37, no. 1, pages 103–111, 1997. (Cited on page 34.)

[Starck 2002] Jean-Luc Starck, Emmanuel J Candès and David L Donoho. *The curvelet transform for image denoising.* IEEE Transactions on image processing, vol. 11, no. 6, pages 670–684, 2002. (Cited on page 30.)

[Stehling 1991] Michael K Stehling, Robert Turner and Peter Mansfield. *Echo-planar imaging: magnetic resonance imaging in a fraction of a second.* Science, vol. 254, no. 5028, page 43, 1991. (Cited on page 21.)

[Stejskal 1965] Edward O Stejskal and John E Tanner. *Spin diffusion measurements: spin echoes in the presence of a time-dependent field gradient.* The journal of chemical physics, vol. 42, no. 1, pages 288–292, 1965. (Cited on page 15.)

[Stikov 2011] N Stikov, LM Perry, A Mezer, JM Pauly, BA Wandell and RF Dougherty. *Modeling and Measuring the Myelin g-ratio.* In Proc Intl Soc Mag Reson Med, volume 19, page 225, 2011. (Cited on page 106.)

[Suarez 2012] Ralph O. Suarez, Olivier Commowick*et al.* *Automated delineation of white matter fiber tracts with a multiple region-of-interest approach.* Neuroimage, vol. 59, no. 4, pages 3690–3700, 2012. (Cited on pages 78 and 87.)

[Sumner 1991] Austin J Sumner and Gareth J Parry. *Demyelinating disease of the peripheral nervous system.* Current Opinion in Neurology, vol. 4, no. 2, pages 214–220, 1991. (Cited on page 13.)

[Svendsen 2002] Clive N Svendsen. *Neurobiology: The amazing astrocyte.* Nature, vol. 417, no. 6884, pages 29–32, 2002. (Cited on page 12.)

[Tabelow 2008] Karsten Tabelow, Jörg Polzehl, Vladimir Spokoiny and Henning U Voss. *Diffusion tensor imaging: structural adaptive smoothing.* NeuroImage, vol. 39, no. 4, pages 1763–1773, 2008. (Cited on page 22.)

[Talairach 1988] Jean Talairach and Pierre Tournoux. *Co-planar stereotaxic atlas of the human brain. 3-Dimensional proportional system: an approach to cerebral imaging.* 1988. (Cited on page 84.)

[Taquet 2012] Maxime Taquet, Benoit Scherrer*et al. Registration and analysis of white matter group differences with a multi-fiber model.* In MICCAI 2012, pages 313–320. 2012. (Cited on page 62.)

[Taquet 2014] Maxime Taquet, Benoit Scherrer, Olivier Commowick, Jurrriaan M. Peters, Mustafa Sahin, Benoit Macq and Simon K. Warfield. *A Mathematical Framework for the Registration and Analysis of Multi-Fascicle Models for Population Studies of the Brain Microstructure.* IEEE Transactions on Medical Imaging, vol. 2, no. 33, pages 504–17, 2014. (Cited on page 40.)

[Toh 2011] CH Toh, K-C Wei, S-H Ng, Y-L Wan, C-P Lin and Mauricio Castillo. *Differentiation of brain abscesses from necrotic glioblastomas and cystic metastatic brain tumors with diffusion tensor imaging.* American Journal of Neuroradiology, vol. 32, no. 9, pages 1646–1651, 2011. (Cited on page 23.)

[Treadway 2011] Michael T Treadway and David H Zald. *Reconsidering anhedonia in depression: lessons from translational neuroscience.* Neuroscience & Biobehavioral Reviews, vol. 35, no. 3, pages 537–555, 2011. (Cited on page 13.)

[Tuch 2002] David Solomon Tuch. *Diffusion MRI of complex tissue structure.* PhD thesis, Citeseer, 2002. (Cited on page 32.)

[Tuch 2003] David S Tuch, Timothy G Reese, Mette R Wiegell and Van J Wedeen. *Diffusion MRI of complex neural architecture.* Neuron, vol. 40, no. 5, pages 885–895, 2003. (Cited on pages 21 and 32.)

[Van Essen 2012] David C Van Essen, Kamil Ugurbil, E Auerbach, D Barch, TEJ Behrens, R Bucholz, Acer Chang, Liyong Chen, Maurizio Corbetta, Sandra W Curtiss*et al. The Human Connectome Project: a data acquisition perspective.* Neuroimage, vol. 62, no. 4, pages 2222–2231, 2012. (Cited on pages 74, 75 and 76.)

[Van Laere 1992] J Van Laere. *Vesalius and the nervous system*, 1992. (Cited on page 14.)

[Vercauteren 2008] Tom Vercauteren, Xavier Pennec, Aymeric Perchant and Nicholas Ayache. *Symmetric Log-Domain Diffeomorphic Registration: A Demons-Based Approach.* In Medical Image Computing and Computer-Assisted Intervention - MICCAI 2008, volume 5241 of *Lecture Notes in Computer Science*, pages 754–761, 2008. (Cited on page 48.)

[Vesalius 1543] Andreas Vesalius. De humani corporis fabrica libri septem. 1543. (Cited on page 14.)

[Von Luxburg 2007] Ulrike Von Luxburg. *A tutorial on spectral clustering.* Statistics and computing, vol. 17, no. 4, pages 395–416, 2007. (Cited on page 65.)

[Voss 2006] Henning U Voss, Richard Watts, Aziz M Uluğ and Doug Ballon. *Fiber tracking in the cervical spine and inferior brain regions with reversed gradient diffusion tensor imaging.* Magnetic resonance imaging, vol. 24, no. 3, pages 231–239, 2006. (Cited on pages 40, 42 and 49.)

[Vovk 2007] Uro Vovk, Franjo Pernus and Botjan Likar. *A review of methods for correction of intensity inhomogeneity in MRI.* IEEE transactions on medical imaging, vol. 26, no. 3, pages 405–421, 2007. (Cited on page 41.)

[Wang 2004] Zhizhou Wang, Baba C Vemuri, Yunmei Chen and Thomas H Mareci. *A constrained variational principle for direct estimation and smoothing of the diffusion tensor field from complex DWI.* IEEE transactions on Medical Imaging, vol. 23, no. 8, pages 930–939, 2004. (Cited on page 23.)

[Wang 2005] Fu-Nien Wang, Teng-Yi Huang, Fa-Hsuan Lin, Tzu-Chao Chuang, Nan-Kuei Chen, Hsiao-Wen Chung, Cheng-Yu Chen and Kenneth K Kwong. *PROPELLER EPI: an MRI technique suitable for diffusion tensor imaging at high field strength with reduced geometric distortions.* Magnetic resonance in medicine, vol. 54, no. 5, pages 1232–1240, 2005. (Cited on page 57.)

[Wang 2014] Yuanxiang Wang, Hesamoddin Salehian, Guang Cheng and Baba C Vemuri. *Tracking on the product manifold of shape and orientation for tractography from diffusion MRI.* In Proceedings of the IEEE Conference on Computer Vision and Pattern Recognition, pages 3051–3056, 2014. (Cited on page 30.)

[Wedeen 2005] Van J Wedeen, Patric Hagmann, Wen-Yih Isaac Tseng, Timothy G Reese and Robert M Weisskoff. *Mapping complex tissue architecture with diffusion spectrum magnetic resonance imaging.* Magnetic resonance in medicine, vol. 54, no. 6, pages 1377–1386, 2005. (Cited on page 32.)

[Wedeen 2008] Van J Wedeen, RP Wang, Jeremy D Schmahmann, Thomas Benner, WYI Tseng, Guangping Dai, DN Pandya, Patric Hagmann, Helen D'Arceuil

and Alex J de Crespigny. *Diffusion spectrum magnetic resonance imaging (DSI) tractography of crossing fibers.* Neuroimage, vol. 41, no. 4, pages 1267–1277, 2008. (Cited on page 92.)

[Weiskopf 2005] N. Weiskopf, U. Klose, N. Birbaumer and K. Mathiak. *Single-shot compensation of image distortions and BOLD contrast optimization using multi-echo EPI for reltime fMRI.* Neuroimage, vol. 24, no. 4, pages 1068–1079, 2005. (Cited on page 41.)

[Werring 2000] DJ Werring, D Brassat, AG Droogan, CA Clark, MR Symms, GJ Barker, DG MacManus, AJ Thompson and DH Miller. *The pathogenesis of lesions and normal-appearing white matter changes in multiple sclerosis.* Brain, vol. 123, no. 8, pages 1667–1676, 2000. (Cited on page 83.)

[Westin 2002] C-F Westin, Stephan E Maier, Hatsuho Mamata, Arya Nabavi, Ferenc A Jolesz and Ron Kikinis. *Processing and visualization for diffusion tensor MRI.* Medical image analysis, vol. 6, no. 2, pages 93–108, 2002. (Cited on pages 47 and 88.)

[Whitcher 2007] Brandon Whitcher, Jonathan J Wisco, Nouchine Hadjikhani and David S Tuch. *Statistical group comparison of diffusion tensors via multivariate hypothesis testing.* Magnetic Resonance in Medicine, vol. 57, no. 6, pages 1065–1074, 2007. (Cited on page 84.)

[White 2008] Tonya White, Miranda Nelson and Kelvin O Lim. *Diffusion tensor imaging in psychiatric disorders.* Topics in Magnetic Resonance Imaging, vol. 19, no. 2, pages 97–109, 2008. (Cited on page 24.)

[Wieshmann 1997] UC Wieshmann, MR Symms and SD Shorvon. *Diffusion changes in status epilepticus.* The Lancet, vol. 350, no. 9076, pages 493–494, 1997. (Cited on page 24.)

[Wiest-Daesslé 2007] Nicolas Wiest-Daesslé, Sylvain Prima, Pierrick Coupé, Sean Morrissey and Christian Barillot. *Non-local means variants for denoising of diffusion-weighted and diffusion tensor MRI.* Medical Image Computing and Computer-Assisted Intervention–MICCAI 2007, pages 344–351, 2007. (Cited on page 88.)

[Wiest-Daesslé 2009] Nicolas Wiest-Daesslé. *Imagerie du tenseur de diffusion pour l'étude de pathologies cérébrales.* PhD thesis, 2009. Thèse de doctorat dirigée par Barillot, Christian et Prima, Sylvain Informatique Rennes 1 2009. (Cited on page 101.)

[Wilt 2009] Brian A Wilt, Laurie D Burns, Eric Tatt Wei Ho, Kunal K Ghosh, Eran A Mukamel and Mark J Schnitzer. *Advances in light microscopy for neuroscience.* Annual review of neuroscience, vol. 32, pages 435–506, 2009. (Cited on page 14.)

[Wolf 1967] Joseph Albert Wolf. Spaces of constant curvature, volume 96. McGraw-Hill New York, 1967. (Cited on page 26.)

[Woods 1999] Roger P Woods, Mirella Dapretto, Nancy L Sicotte, Arthur W Toga and John C Mazziotta. *Creation and use of a Talairach-compatible atlas for accurate, automated, nonlinear intersubject registration, and analysis of functional imaging data.* Human brain mapping, vol. 8, no. 2-3, pages 73–79, 1999. (Cited on page 84.)

[Wu 2008] M. Wu, L.-C. Chang, L. Walker, H. Lemaitre, A.S. Barnett, S. Marenco and C. Pierpaoli. *Comparison of EPI Distortion Correction Methods in Diffusion Tensor MRI Using a Novel Framework.* In MICCAI, Part II, volume 5242 of *LNCS*, pages 321–329, 2008. (Cited on page 40.)

[Yamada 2007] K Yamada, K Sakai, FGC Hoogenraad, R Holthuizen, K Akazawa, H Ito, H Oouchi, S Matsushima, T Kubota, H Sasajima*et al.* *Multitensor tractography enables better depiction of motor pathways: initial clinical experience using diffusion-weighted MR imaging with standard b-value.* American Journal of Neuroradiology, vol. 28, no. 9, pages 1668–1673, 2007. (Cited on page 92.)

[Yamada 2009] Kei Yamada, Koji Sakai, Kentaro Akazawa, YUEN Sachiko and Tsunehiko Nishimura. *MR tractography: a review of its clinical applications.* Magnetic resonance in medical sciences, vol. 8, no. 4, pages 165–174, 2009. (Cited on page 92.)

[Yu 2005] Chun Shui Yu, Kun Cheng Li, Yun Xuan, Xun Ming Ji and Wen Qin. *Diffusion tensor tractography in patients with cerebral tumors: a helpful technique for neurosurgical planning and postoperative assessment.* European journal of radiology, vol. 56, no. 2, pages 197–204, 2005. (Cited on page 92.)

[Zaitsev 2004] M Zaitsev, J Hennig and O Speck. *Point spread function mapping with parallel imaging techniques and high acceleration factors: Fast, robust, and flexible method for echo-planar imaging distortion correction.* Magnetic Resonance in Medicine, vol. 52, no. 5, pages 1156–1166, 2004. (Cited on page 40.)

[Zalc 2006] Bernard Zalc. *The acquisition of myelin: a success story.* In Novartis Foundation symposium, volume 276, page 15. Chichester; New York; John Wiley; 1999, 2006. (Cited on page 12.)

[Zelnik-Manor 2004] Lihi Zelnik-Manor and Pietro Perona. *Self-tuning spectral clustering.* In NIPS, volume 17, page 16, 2004. (Cited on page 81.)

[Zhang 2011] Hui Zhang, Penny L Hubbard, Geoff JM Parker and Daniel C Alexander. *Axon diameter mapping in the presence of orientation dispersion with diffusion MRI.* Neuroimage, vol. 56, no. 3, pages 1301–1315, 2011. (Cited on page 37.)

[Zhang 2012a] Hui Zhang, Torben Schneider, Claudia A Wheeler-Kingshott and Daniel C Alexander. *NODDI: practical in vivo neurite orientation dispersion and density imaging of the human brain.* Neuroimage, vol. 61, no. 4, pages 1000–1016, 2012. (Cited on pages 12 and 37.)

[Zhang 2012b] Hui Zhang, Torben Schneider, Claudia A. Wheeler-Kingshott and Daniel C. Alexander. *NODDI: Practical in vivo neurite orientation dispersion and density imaging of the human brain.* NeuroImage, vol. 61, no. 4, pages 1000 – 1016, 2012. (Cited on page 40.)